University of Bath

PHD

Adaptive control of an active seat for occupant vibration reduction

Gan, Zengkang

Award date:
2015

Awarding institution:
University of Bath

Link to publication

Alternative formats
If you require this document in an alternative format, please contact:
openaccess@bath.ac.uk

Copyright of this thesis rests with the author. Access is subject to the above licence, if given. If no licence is specified above, original content in this thesis is licensed under the terms of the Creative Commons Attribution-NonCommercial 4.0 International (CC BY-NC-ND 4.0) Licence (https://creativecommons.org/licenses/by-nc-nd/4.0/). Any third-party copyright material present remains the property of its respective owner(s) and is licensed under its existing terms.

Take down policy
If you consider content within Bath's Research Portal to be in breach of UK law, please contact: openaccess@bath.ac.uk with the details. Your claim will be investigated and, where appropriate, the item will be removed from public view as soon as possible.

Download date: 04. May. 2023

Adaptive control of an active seat for occupant vibration reduction

Zengkang Gan

A thesis submitted for the degree of Doctor of Philosophy

Department of Mechanical Engineering
University of Bath

February 2015

COPYRIGHT

Attention is drawn to the fact that copyright of this thesis rests with the author. A copy of this thesis has been supplied on condition that anyone who consults it is understood to recognise that its copyright rests with the author and that they must not copy it or use material from it except as permitted by law or with the consent of the author.

This thesis may be made available for consultation within the University Library and maybe photocopied or lent to other libraries for the purpose of consultation with effect from_____.

Signed on behalf of the Faculty of Engineering & Design.

Abstract

Vehicle occupants are typically exposed to unpleasant whole-body vibration (WBV) for extended period of time. It is well known that the transmission of unwanted vibration to the human body can lead to fatigue and discomfort. Moreover, the unwanted vibration normally distributed in the low-frequency range has been found as the main risk factor for lower back pain and lumbago, which seriously affect the health and working performance of occupants. Thus vibration cancellation on seats has attracted considerable interest in recent years. So far, for most vehicle seats, vibration isolation is achieved passively by using seat cushions and conventional energy absorbers, which have very limited performance in the low-frequency range.

The work presented in this thesis forms a successful development and experimental study of an active seat and control algorithm for occupants' WBV reduction under low frequency excitations. Firstly, a modelling study of the seat human subjects (SHS) and an extensive experimental measurement of the vibration transmissibility of a test dummy and vehicle seat are carried out. The biodynamic responses of SHS exposed to uncoupled vertical and fore-and-aft WBV is modelled. A comparison with the existing models is made and the results show that an improved fit with the aggregated experimental data is achieved. Secondly, an active seat is developed based upon the observations and understanding of the SHS and seat system. The characteristics of the active seat dynamics are identified through experimental tests found suitable for the development of an active seat to attenuate the vibration experienced by vehicle occupants.

The vibration cancellation performance of the active seat is initially examined by feedforward plus proportional-integral (PI) control tests. Through these tests, the effectiveness of the actuators control authority is verified, but the limitations are also revealed. Because the active seat system is subject to non-linear and time-varying behaviour, a self-tuning fully adaptive algorithm is a prime requirement. The Filtered-x Least-Mean-Square (FXLMS) algorithm with the Fast-block LMS (FBLMS) system identification technique is found suitable for this application and is investigated through experimental tests. Substantial vibration reductions are achieved for a variety of input vibration profiles. An excellent capability of the active seat and control system for efficiently reducing the vibration level of seated occupants under low-frequency WBV is demonstrated.

Acknowledgements

I would like to sincerely thank my supervisors Dr. Andrew Hillis and Dr. Jos Darling for their supervision and guidance throughout the work. I would also like to thank the Centre for Power Transmission and Motion Control (CPTMC) for providing brilliant research facilities and environment. Thanks to Alan Jefferis, Graham Rattley and other technical staff for assisting in experiments. Thanks also to my friends in Bath for their accompanying.

Special thanks to my parents, sister and other family members for their endless love and support throughout my life. Special thanks also to Xingtong Yan for her patience and understanding.

Finally, I acknowledge the funding from the Department of Mechanical Engineering at the University of Bath, and the funding from the China Scholarship Council.

Publications

As a result of the work conducted in this thesis, the following publications have been produced:

Zengkang Gan, Andrew J. Hillis, Jocelyn Darling. Development of a biodynamic model of a seated human body exposed to low frequency whole-body vibration. *Proceedings of the eleventh International Conference on Vibration Problems,* Lisbon, Portugal, 2013.

Zengkang Gan, Andrew J. Hillis, Jocelyn Darling. Biodynamic modelling of seated human subjects exposed to uncoupled vertical and fore-and-aft whole-body vibration. *Journal of Vibration Engineering and Technologies,* Vol. 3, 3, 2015.

Zengkang Gan, Andrew J. Hillis, Jocelyn Darling. Adaptive control of an active seat for occupant vibration reduction. *Journal of Sound and Vibration,* 2015, 349, 39–55.

Contents

ABSTRACT ..... **I**

ACKNOWLEDGEMENTS ..... **III**

PUBLICATIONS ..... **V**

NOTATION ..... **XI**

CHAPTER 1

INTRODUCTION **1**

1.1 Whole-body vibration 1

1.2 Vehicle seat vibration isolation 3

1.2.1 Passive seat vibration isolation 3

1.2.2 Shock isolation using energy absorbers 4

1.2.3 Semi-active and active seat suspensions 5

1.3 Objectives of the research 6

1.4 Scope of the thesis 7

CHAPTER 2

LITERATURE REVIEW **9**

2.1 Modelling of seated human subjects 9

2.1.1 Human body FE models 10

2.1.2 Human body spine models 10

2.1.3 Human body lumped mass models 11

2.2 Semi-active and active seat suspensions 12

2.2.1 Semi-active seat suspensions 13

2.2.3 Active seat suspensions 14

2.2.4 Performance Comparison 15

2.3 Semi-active and active vibration control techniques 16

2.3.1 Semi-active vibration control techniques 16

2.3.2 Active vibration control techniques 18

2.4 Conclusions 20

CHAPTER 3

SEATED HUMAN BODY MODELLING AND SIMULATION 22

3.1 Measurement data of seated human subjects 22

3.2 Model description 26

3.3 Equations of motion (EOMs) 27

3.4 EOMs solution in the frequency domain 29

3.5 Model parameter identification 30

3.6 Simulation and comparison results 32

3.7 Discussions 38

3.8 Conclusions 39

CHAPTER 4

MEASUREMENTS OF VEHICLE SEAT AND TEST DUMMY VIBRATION TRANSMISSIBILITY 40

4.1 Experimental setup 40

4.1.1 Vehicle seat 40

4.1.2 Test dummy 40

4.1.3 Multi-axis vibration simulation table 42

4.1.4 Seat interface transducer pad 42

4.1.5 Accelerometers and data acquisition system 42

4.2 Vibration measurement method 44

4.2.1 Excitation signal types 44

4.2.2 PSD and ordinary coherence analysis 46

4.3 Vehicle seat vibration transmissibility results 47

4.3.1 Empty seat transmissibility 47

4.3.2 Seat transmissibility with a sandbag 49

4.3.3 Seat transmissibility with a dummy 51

4.4 Dummy vibration transmissibility results 53

4.4.1 Solid seat tests 54

4.4.2 Vehicle seat tests 60

4.5 Experimental measurements discussions 64

4.6 Conclusions 66

CHAPTER 5

ACTIVE SEAT STRUCTURE AND DYNAMICS 67

5.1 Active seat mechanical structure 67

5.1.1 Overall structure....67
5.1.2 Two-bar lever mechanism....69
5.1.3 Linear slider mechanism....70
5.1.4 Passive shock absorber....70
5.1.5 Active actuation element....71
5.2 Active seat dynamics....72
5.2.1 Shock absorber dynamics....72
5.2.2 Vibration transmissibility of the empty seat....76
5.2.3 Frequency responses of the empty seat....76
5.2.4 Frequency responses of the active seat with a dummy....78
5.3 Active seat dynamics discussions....79
5.4 Conclusions....80

CHAPTER 6

EXPERIMENTAL STUDIES: FEEDFORWARD PLUS PI CONTROL TESTS 81

6.1 Feedforward plus PI feedback control....81
6.2 Experimental setup....83
6.3 Experimental results....85
6.3.1 Single frequency cancellation....85
6.3.2 Multiple harmonics cancellation....88
6.3.3 Performance under low-frequency large amplitude disturbance....90
6.4 Problems and discussion....91
6.5 Conclusions....92

CHAPTER 7

ADAPTIVE CONTROLLER DESIGN AND SIMULATION 93

7.1 The LMS adaptive algorithm....93
7.2 Effect of secondary path dynamics....99
7.3 The FXLMS algorithm....100
7.4 On-line secondary path identification techniques....102
7.4.1 Overall modelling technique....102
7.4.2 Auxiliary random noise technique....103
7.5 FBLMS on-line secondary path identification....105
7.6 Simulation of on-line secondary path identification....108
7.7 Active narrow-band vibration cancellation....112

7.7.1 Single-frequency cancellation using the FXLMS algorithm....113
7.7.2 Multiple harmonics cancellation using the FXLMS algorithm....116
7.8 Simulation of active narrow-band vibration cancellation....117
7.8.1 Simulation of single-frequency cancellation....118
7.8.2 Simulation of multiple harmonics cancellation....120
7.9 Conclusions....124

CHAPTER 8

EXPERIMENTAL STUDIES: ADAPTIVE CONTROL TESTS....126

8.1 Experimental setup and the secondary path....126
8.2 Single frequency cancellation....127
8.2.1 Results for the secondary path 1....128
8.2.2 Results for the secondary path 2....131
8.3 Multiple harmonics cancellation....135
8.4 Transient switching frequency cancellation....140
8.2.1 Results for the secondary path 1....140
8.2.2 Results for the secondary path 2....146
8.5 Performance when subject to low-frequency large amplitude disturbances....150
8.6 Discussions....154
8.7 Conclusions....155

CHAPTER 9

CONCLUSIONS AND FUTURE WORK....156

1.1 Conclusions....156
1.2 Recommendations for future work....158

REFERENCES....160

Notation

Chapter 3

Variable	Description
c_1	Human body model lower torso damping
c_2	Human body model viscera damping
c_3	Human body model arms damping
c_4	Human body model upper torso damping
c_5	Human body model head and neck damping
c_{41}	Human body model spine damping
c_b	Human body model back damping
c_r	Human body model head and neck rotation damping
$\boldsymbol{C}$	Human body model damping matrix
$\boldsymbol{F_n}(j\omega)$	Complex Fourier transform vector of $\{\boldsymbol{f_n}\}$
$\boldsymbol{f_n}$	Human body model excitation force vector
g	Acceleration due to gravity
j	Imaginary unit
k_1	Human body model lower torso spring rate
k_2	Human body model viscera spring rate
k_3	Human body model arms spring rate
k_4	Human body model upper torso spring rate
k_5	Human body model head and neck spring rate
k_{41}	Human body model spine spring rate
k_b	Human body model back spring rate
k_r	Human body model head and neck rotation spring rate
$\boldsymbol{K}$	Human body model stiffness matrix
l_n	Average human neck distance
p_f	Fore-and-aft model unknown parameters vector
p_v	Vertical model unknown parameters vector
$\boldsymbol{M}$	Human body model mass matrix
m_1	Human body model lower torso mass

m_2	Human body model viscera mass
m_3	Human body model arms mass
m_4	Human body model upper torso mass
m_5	Human body model head and neck mass
N	Number of the measured target data points
$\boldsymbol{y_c}$	Human body response calculated value
$\boldsymbol{y_m}$	Human body response measured target value
$\ddot{\boldsymbol{z}}$	Human body model acceleration vector
$\dot{\boldsymbol{z}}$	Human body model velocity vector
$\boldsymbol{z}$	Human body model displacement vector
$\boldsymbol{Z}(j\omega)$	Complex Fourier transform vector of $\{\boldsymbol{z}\}$
ω	Angular frequency
θ	Human body model head and neck rotational degree
$\dot{\theta}$	Human body model head and neck rotational speed
$\ddot{\theta}$	Human body model head and neck rotational acceleration

Chapter 4

E	Expected value
f	Frequency
$G_{xx}(f)$	One-sided spectral density functions of x
$G_{yy}(f)$	One-sided spectral density functions of y
$H(f)$	System frequency response function
$\gamma_{xy}^2(f)$	Ordinary coherency between signal x and y
$S_{xx}(f)$	Power spectral density of x
$S_{yy}(f)$	Power spectral density of y
$S_{xy}(f)$	Cross-spectral density function between signal x and y
T	Time interval
$x(t)$	Input signal
$y(t)$	Output signal
π	The ratio of a circle's circumference to its diameter

Chapter 6

$d(n)$	Desired response or disturbance
$e(n)$	Measured error signal
G_{ff}	Feedforward controller
K_{ff}	Gain of the feedforward controller
n	Index
$P(z)$	Primary path dynamics (frequency-domain)
$S(z)$	Secondary path dynamics (frequency-domain)
T_z	Zero of the lead-lag compensator
T_p	Pole of the lead-lag compensator
$u(n)$	Active control signal
$v(n)$	Measured seat base vibration signal

Chapter 7

A_0, A_1	Reference signals amplitudes
A_s	Secondary path amplitude at ω_0
A_w	Adaptive filter amplitude at ω_0
$d(n)$	Desired response or disturbance
$D(z)$	Z-transforms of the signal $d(n)$
$e(n)$	Measured error signal
$\hat{e}(n)$	Estimated error signal
E	Expected value
$E(z)$	Z-transforms of the signal $e(n)$
$\mathbf{E}_f(k)$	Frequency-domain error signal
$H(z)$	Close-loop transfer function between the primary input and the error output
k	Block index
L	Adaptive filter length
m	Channel index number
M	Harmonics number
n	Index
$\mathbf{p}$	Cross-correlation vector

$\hat{\mathbf{p}}$	Instantaneous estimate of the cross-correlation vector
P_x	The power of $x(n)$
$P(z)$	Primary path dynamics (frequency-domain)
$\hat{P}(z)$	Estimated primary path dynamics (frequency-domain)
$\boldsymbol{P}_i(k)$	Estimated power of the samples of the filter input (frequency-domain)
$\mathbf{R}$	Input autocorrelation matrix
$\hat{\mathbf{R}}$	Instantaneous estimate of the input autocorrelation matrix
$S(z)$	Secondary path dynamics (frequency-domain)
$\hat{S}(z)$	Estimated secondary path dynamics (frequency-domain)
Δt	Fixed sampling interval
$\mathbf{U}_f(k)$	FFT of the two successive blocks of noise signal $u(n)$
$v(n)$	White noise
$\mathbf{v}(n)$	Buffered white noise vector
$\hat{v}'(n)$	Output of the modelling filter
$\mathbf{w}(n)$	Filter coefficients vector
$\mathbf{w}^o$	Optimal coefficient vector
$W(z)$	LMS filter (frequency-domain)
$\hat{\mathrm{w}}(k)$	Time-domain weight vector
$\hat{\mathrm{w}}_e(k)$	Zero vector
$\hat{W}_f(k)$	Frequency -domain weight vector
$x_0(n),\ x_1(n)$	Reference signals
$x_0'(n),\ x_1'(n)$	Reference signals filtered by the secondary path estimate
$\mathbf{x}(n)$	Input signal vector
$x'(n)$	$x(n)$ filtered by $\hat{s}(n)$
$X(z)$	Z-transforms of the signal $x(n)$
$y(n)$	Filter output
$Y(z)$	Z-transforms of the signal $y(n)$
z^{-1}	Unit delay elements
$\xi(n)$	MSE performance function
ξ_{min}	The minimum MSE
$\nabla\xi(n)$	The gradient of the error surface

μ	Rate of descent to the optimal point
$\lambda_{\max}$	Largest eigenvalue of the input autocorrelation matrix
β	Leakage factor
ξ	Damping ration
ω_e	Estimated vibration frequency
ω_n	Natural frequency
$\emptyset_s$	Secondary path phase at ω_0
$\emptyset_w$	Adaptive filter phase at ω_0

Chapter 1

Introduction

This chapter presents a background to the research work. The harmful effects of whole-body vibration on seated human body are described. An overview of the vehicle seat vibration isolation systems is provided and the overall objectives of the research are introduced. The scope of the thesis is also included in the end of this chapter.

1.1 Whole-body vibration

Vehicle occupants are typically exposed to unpleasant whole-body vibration for extended periods of time. It is well known that the transmission of unwanted vibration to the human body can lead to fatigue and discomfort. Moreover, the unwanted vibration normally distributed in the low-frequency range (0.5-25 Hz) has been found as the main risk factor for lower back pain and lumbago [1-6], which seriously affect the mental and physical health of occupants and influence their working performance.

Numerous studies, primarily focused on vertical vibration, have been conducted to evaluate the response characteristics of human body dynamics, and the primary goal is to determine the magnitude of the human body resonances and the frequency locations associated with the highest body motions. The dominant resonance of the human body to vertical vibration appears to be 3-6 Hz [7-9], which explains why low frequency vibrations significantly affect the comfort of seated persons.

The effects of whole-body vibration on the human body can be divided into two main categories: biodynamic effects and physiological and psychological effects. Biodynamic effects can be evaluated by frequency response transfer functions. One commonly used type of frequency response transfer function involves measuring the transmitted force of the human body against a supporting structure, typically a seat mounted on load cells.

This has the advantage that it is a non-invasive method. The ratio between the transmitted force at the seat and the input velocity at the seat is called the driving-point impedance, which is described by the magnitude of the ratio and the phase angle between the two measurements. Plots of impedance against frequency are then used to identify regions of high transmission and resonance in the human body. Peaks in the magnitude of the plots and rapid changes in the phase of the plots are indicative of a body resonance. Human body resonance can also be evaluated by vibration transmissibility. Vibration transmissibility is defined as the ratio of the output vibration level transmitted through the subject to the input vibration level in the frequency range of interest. This can be obtained in different forms by examining different response quantities, such as displacement, velocity and acceleration.

Apart from the biodynamic response, some physiological and psychological effects such as fatigue, discomfort, lower back pain, neck and spine strain injuries, spinal abnormalities, blurred vision and perception are observed and reported in many studies. For example, vibration transmitted from the floor can introduce relative motion of the eye with respect to an observed object or display, which can cause difficulty in reading instruments and performing visual tasks for the aircrew in aerospace environments. Small amplitude vibration can cause mental fatigue, especially when experienced over long periods. Human muscle begins to fatigue after around 30 minute's exposure to severe vibrations. Muscle fatigue will not only lead to discomfort, but can also lead to a reduction of the protective ability of the muscles. Human muscular-skeletal systems work as a natural protective mechanism, large muscle groups on the human body are capable of absorbing vibration energy caused by external sources. However, this protective ability may be limited by the minimum reaction time of the nerve muscle reflex arc which is about 75 milliseconds for leg muscle and is equivalent to frequencies up to 13 Hz [10].

Many researches have shown that there is a link between lower back pain (LBP) and whole-body vibration. LBP is a serious disabling health problem facing industrialized societies and the costs of it are immense. A review of studies on seated whole-body vibration and LBP has been made by Pope et al. [11]. Some in vivo measurements were carried out in the study, and they concluded that the muscles will be fatigued and the discs will be compressed after whole-body vibration, and thus become less capable of

absorbing and distributing load. This also means that the spine is in a poorer condition to sustain large loads.

1.2 Vehicle seat vibration isolation

The harmful effects on human performance and health caused by unwanted vibration from vehicle seats are of increasing concern. Since it is much more difficult and more energy-consuming to successfully reduce the vibration level globally than locally on vehicles, vibration cancellation on seats – the part which directly contacts with the human, has attracted considerable interest in recent years.

1.2.1 Passive seat vibration isolation

So far, for most vehicle seats, vibration isolation is achieved passively by using seat cushions and conventional springs and dampers. Some materials commonly used in seat cushions can effectively reduce higher frequency vibration peaks, but tend to amplify the occupants' body vibration in the low frequency range. In the experiment conducted by Pope et al. [12], several kinds of seat cushions, including Polyethylene foam, Polyethylene foam (stiffer), and Viscoelastic material, which represented a wide range of cushions available for seating, were tested. The response curves were compared and analysed, the results showed that the softest material moved the transmissibility peak to below 4 Hz and increased its amplitude; the stiffer material tended to move the transmissibility peak to higher frequency and produce rotational response; the viscoelastic material had little effect below 8 Hz. Some new seat cushion materials have been developed and used in passive suspension systems in order to attenuate seated human body vibrations at high frequency, but these materials lose their efficiency at low frequency, and always produce relatively large motions.

Conventional springs and dampers are commonly used for vehicle seat suspensions. The springs act as an energy-storing element while the dampers act as an energy dissipating element. Since these two elements cannot add energy to the system this kind of suspension systems are called passive. The coefficients of the spring and damper are usually tuned to one set of values and only for an average occupant ride comfort. Although there is an increase in the use of dampers with switchable or continuously

adjustable characteristics of damping, these passive systems cannot provide optimal vibration isolation performance for individuals. It is known that passive seat suspensions are subject to some inherent limitations: They are difficult to optimize, have a poor performance in the low frequency range, and often 'de-tune' due to deterioration of the structural parameters and/or variations in the excitation frequency.

1.2.2 Shock isolation using energy absorbers

Currently, most aircraft seats are designed primarily to meet crashworthiness criteria by employing energy absorbers (EAs). The high acceleration vertical shock loads that are transmitted from the base frame of the aircraft and imparted into the human body during harsh or crash landings can be attenuated to within a tolerable range by the energy absorption systems.

Most commonly used energy absorbers are fixed-load energy absorbers (FLEAs). The load-stroke profiles of these FLEAs are tuned to a constant factory-established load throughout their entire operating range. FLEAs are tuned only for one occupant weight/type (typically a 50th percentile male) and one crash level (typically to the highest crash design level). FLEAs are typically designed to provide approximate 15 g seat deceleration limit for the occupant to whom they are tuned. The factory established stroking load tends to be too high for lighter occupants while too low for heavier occupants. The inappropriate load can result in an increased injury risk [13].

Fixed-profile energy absorbers (FPEAs) were developed after the FLEAs. These devices aim to more efficiently attenuate shock load by taking advantage of the dynamic response of the human body. FPEAs use a 'notched' load-stroke profile with an initial load spike to achieve a quick compress of the human body "springs". Then, the load is lowered rapidly to minimize the overshoot as the body is loaded up, thereby limiting the maximum load on the occupant's spine. The energy absorber load would then be again increased to a sustainable plateau for the rest of the stroke [14]. This type of load-stroke profile allows the body to be decelerated at a higher average acceleration than FLEAs by minimizing the overshoot. However, these FPEAs are still tuned for one occupant weight and one crash level, and therefore, they suffer similar limitations as the FLEAs.

Variable load energy absorbers (VLEAs), which allow the occupant to manually adjust the constant stroking load by setting a dial for their weight, have been developed for an improved performance. These VLEAs exploit the fact that the strength of an occupant's spine is nearly proportional to occupant weight. However, these devices highly rely on plastic deformation of material and their weight adjustment range is limited [14].

The above EAs are all passive in that they cannot adapt their load profile during the real-time operations. Moreover, these EAs do not begin to stroke until the load reaches the tuned threshold and therefore act as a coupling between the floor and the seat. For these reasons, these EAs provide only shock protection and rarely offer vibration isolation on the seat.

1.2.3 Semi-active and active seat suspensions

Semi-active and active seat suspensions are developed to overcome the limitations of passive systems and aim to provide more efficient vibration isolation for occupants. Active suspensions are typically composed of a spring element and some type of force actuator which is capable of supplying energy to the system. A variety of actuators have been developed and used in active vibration control systems, which include hydraulic, pneumatic, electrohydraulic, electromagnetic, and stacked piezoelectric actuators. The actuator is the heart of active system, the vibration cancellation performance of the whole active system is mainly dependent upon the actuator force.

A compromise between passive and active types is semi-active suspension systems. Semi-active systems can only passively modulate damping or spring forces according to a parameter tuning policy with only a small amount of control effort. So far, many semi-active dampers have been developed for this type of suspensions. The damping characteristics are usually controlled by modulation of fluid-flow orifices, of dry friction forces or of electric or magnetic field applied to electrorheological or magnetorheological fluid dampers. Semi-active suspension system can offer a compromise between the simplicity of passive systems, and the cost of higher-performance fully active suspension system.

For both the active and semi-active suspension systems, a control law implemented on a real-time computer processor is required to govern the actuator and determine the

control force. A more detailed literature review of the active and semi-active seat suspensions and the associated control algorithms is presented in Chapter 2.

1.3 Objectives of the research

The main objective of the research was to investigate and demonstrate the feasibility and benefits of an active seat system for occupants' whole-body vibration reduction under low frequency excitations. The first aim was to gain a better insight into the mechanisms and biodynamic responses of the seated human subjects (SHS) under low frequency whole-body vibrations and to develop a mathematical model which is able to represent the biodynamic behaviour of SHS in a more comprehensive way. The second aim was to develop a vibration test dummy which can be used as a seated human body substitute and to set up an experimental test program to characterise the dummy response on a vehicle seat. The next aim was to develop an active seat which is able to attenuate the vibration level on the occupants' body under low frequency excitation range (1-25 Hz). The final aim was to develop an adaptive control algorithm and apply it to the active seat to evaluate the vibration cancellation performance through experimental tests.

For the active seat and vibration control system, the following key requirements need to be met:

1. The system must be able to attenuate the vibration level on the occupants' body in a low frequency range of 1-25 Hz.

2. The system must have high adaptability and robustness, and be able to address the variation in vibratory situation due to the changes in operating conditions (e.g. occupant weight variation and ageing of the suspension system);

3. The control algorithm in the system must be fully self-tuning without *a priori* knowledge about the plant;

1.4 Scope of the thesis

Chapter 1 provides an introduction of the effects of whole-body vibration on seated human body. Overviews of the vehicle seat vibration isolation systems and the overall objectives of the research are presented.

Chapter 2 presents a literature review of the modelling of seated human subjects under low frequency whole-body vibration and a review of the active and semi-active seat suspensions. The advantages and limitations of the two types of suspensions are compared. Additionally, a summary of the various types of controller that have been applied to active and semi-active vibration control systems is given. The Filter-x Least-Mean-Square (FXLMS) algorithm was selected for detailed investigation in Chapter 7.

Chapter 3 presents the development of a lumped-parameter biodynamic model of a seated human subject exposed to low frequency whole-body vibration. Model parameters are identified using curve fitting methods and the STHT, DPMI and APM biodynamic magnitude and phase response functions are simulated. A comparison with the existing models is carried out and the results show that an improved fit with the aggregated experimental data is achieved. The developed model can be used to help in developing anthropodynamic mannequins for vibration assessment.

Chapter 4 presents the experimental measurement results of the vibration transmissibility of a test dummy and vehicle seat. The dynamic response of the test dummy is characterised and the principal whole body modes are found to be broadly consistent with a seated human response. These findings enable the dummy to be used as a seated human body substitute in the active seat vibration cancellation tests in order to ensure an improved consistency in behaviour and avoid safety and ethical issues.

Chapter 5 provides the details of the active seat structure and dynamics. The constituent and mechanical structure of the active seat is described and illustrated by three-dimensional line drawings and photos. The characteristics of the active seat dynamics are identified through experimental tests. The rig is found suitable for the development of an active seat to attenuate the vibration experienced by vehicle occupants.

In chapter 6 the vibration cancellation performance of the active seat using feedforward plus PI control method is examined. Through these tests, the effectiveness of the actuators' control authority is verified and an understanding of the real-time implementation is gained. Meanwhile, the limitations of the feedforward plus PI controller are revealed, which indicates that an advanced adaptive control strategy is required to exploit the whole potential vibration cancellation capability of the active seat.

Chapter 7 provides a necessary theoretical background of the Least-Mean-Square (LMS) adaptive algorithm. The secondary path effect in the implementation of the LMS algorithm is discussed and the filtered-x LMS (FXLMS) algorithm is introduced for solving this problem. Different approaches for secondary path identification are compared and evaluated through simulation exercises. The FXLMS algorithm with the FBLMS system identification technique is evaluated through a simulated system for narrow-band vibration cancellation. The effectiveness of this combination is proved and thus it is applied in the experimental studies described in Chapter 8.

The results of experimental studies of the active seat using adaptive control methods are presented in chapter 8. Substantial vibration reductions are achieved for a single frequency and multiple harmonic signals. The robustness and stability of the control system is validated by cancelling vibration signals with switching frequency. Additionally, the performance of the system when subject to low-frequency large amplitude disturbances is validated. The experimental results demonstrate the capability of the active seat for seated occupant's vibration reduction.

Finally, chapter 9 gives the conclusions and discussions of the work conducted. Recommendations for future work are also included.

Chapter 2

Literature Review

This chapter aims to provide a thorough review of the prior works related to the research objectives of this thesis. In the first part of this chapter, a review of the modelling of seated human subjects under low frequency whole-body vibration is presented. Secondly, a review of active and semi-active seat suspension is provided. Additionally, a summary of the various types of controller that have been applied to active and semi-active vibration control systems is given.

2.1 Modelling of seated human subjects

In order to understand the biodynamic response and adverse effects of whole-body vibration on the human body, a number of seated human body models have been proposed in the literature. The human body is an extremely complex system containing both linear and nonlinear elements (e.g. the viscoelastic nature of soft tissue, large deformation involved during the loading process), and the human population is physically and biologically diverse. This means the mechanical properties will vary hugely from person to person, and makes it difficult to develop an ideal model, however, "All models are wrong but some are useful", George E.P. Box [15]. An appropriate human body model can be used to estimate the forces and motions being transmitted within the body under specific vibration environments, thus it can allow the prediction of the body vibration exposure levels as well as the design and simulation of control method to attenuate the vibration.

The seated human body has already been modelled by many researchers in the literature and most of the models can be categorized into three groups: finite element (FE) models, spine models and lumped mass models. The first group considers the whole human body including the details of the skeleton and soft tissues. The second group

focus on the modelling of the spine and treats other body parts as influencing factors. The third group treats the body as several lumped masses connected by springs and dampers and identifies the model parameters based upon the whole body biodynamic responses.

2.1.1 Human body FE models

A number of human body FE models have been developed during the last two decades, and these models are mainly used for crashworthiness studies. The FE technique uses a discretized definition of the geometry and the constitutive laws relating stresses and strains as inputs. Human body FE models usually include details of the human skeleton and soft tissues, and can predict stresses, strains, and the deformed shapes of bodies.

The Hybrid III 50% [16] model is one of the most commonly used human body FE models for the evaluation of automotive crashworthiness and safety. Some other human body FE models have also been developed and improved by many researchers [17, 18]. The FE model allows a more detailed and accurate representation of the human body, but at a significantly higher computational cost. In addition, since most of these FE models have been developed to evaluate extreme conditions, such as the loading and impacts during automotive crashes, they are not suitable to predict or simulate the human body responses under low frequency and low magnitude vibrations.

2.1.2 Human body spine models

There are two kinds of human body spine models: the continuum and discrete types. A continuum model is one in which the spine is considered as a rod having an infinite number of DOF. This seems too different from the real spine structure. Discrete models consider the spine as a structure formed by various anatomic elements, such as vertebrae, discs, ligaments, muscles, which are individually modelled. These kinds of model are more detailed and much closer to the real spine structure [19]. The early continuum models were developed by Hess and Lombard [20]; Liu and Murray [21] and Terry and Roberts [22]. They considered the spine column as an elastic beam or viscoelastic rod. The first discrete model was presented by Latham [23] which was based on the human body response to aircraft ejection. Other discrete models have been presented by Toth [24], Orne and Liu [25], and Panjabi [26].

One of the latest discrete human spine models presented by Yoshimura and et al. [27] was based on the detailed measurement of vibration transmissibilities from the seat surface to the spinal column and the head. The model contains 10 DOFs, and the vertebrae are represented by rigid bodies which are connected by revolute joints. It is suggested that this model can be used to evaluate the vibration effects to the spinal column. However, there are two concerns in the modelling process. Firstly, the sensors are mounted on the skin surface which will influence the accuracy of measurement. Secondly, the inertia effect of the viscera is taken into account by simply distributing the inertia quantity to each vertebra.

Human body spine models are mainly used to investigate the spine dynamic behaviours, especially the lumbar spine and lower vertebrae biodynamic under shock loading. Since this type of model focuses on the human spine, the global biodynamic response of the whole body cannot be studied thoroughly.

2.1.3 Human body lumped mass models

In this kind of model, the human body is approximated by a lumped mass parameter system, ranging from a linear single degree of freedom system to nonlinear multi degree of freedom systems. Suggs et al. [28] developed a two-DOF damped spring-mass model based on measurements which closely approximated the major dynamic characteristics of a seated man to vertical modes of vibration below 10 Hz. The model was used to build a standardised vehicle seat testing procedure. Payne and Band [29] presented a four DOFs model. In the model, the head, upper torso, abdominal viscera and the pelvis were represented as four rigid masses, which were interconnected by springs and dampers.

Wei and Griffin [30] suggested a two-DOF human and seat model to predict car seat vibration transmissibility. It was found that the predicted seat transmissibilities were close to those measured in a group of eight subjects over the entire frequency range. Boileau and Rakheja [7] proposed a four-DOF human body model, shown in Figure 2.1, considered the typical vehicle driving positions, such as erect without backrest support posture, feet supported and low frequency excitation below 4 m/s^2. The model parameters were estimated by attempting to match the magnitude and phase characteristics of both the vertical driving-point mechanical impedance and seat-to-head

transmissibility. Some more recent models in group two include a multi-DOF lumped parameter seated human body model developed by Rosen and Arcan [31]. This model included two subsystems: the first subsystem represented the apparent mass phenomenon as the global human biodynamic system, and the second represented the local dynamics of the human pelvis/seat cushion contact. The challenge of this multi-DOF model is the identification and optimization of many parameters.

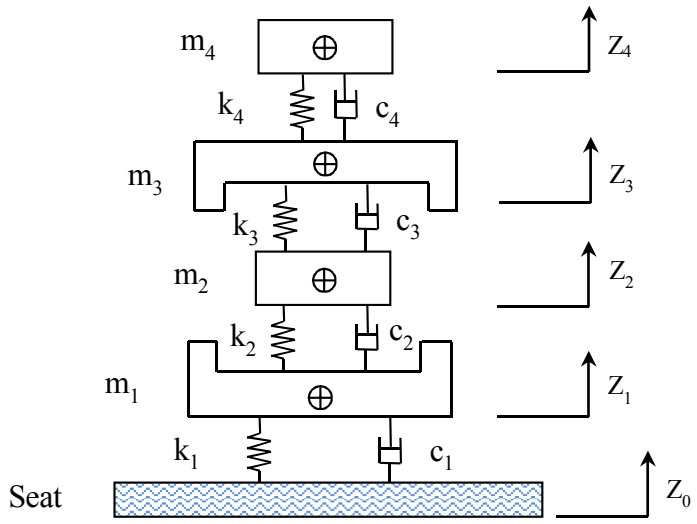

Figure 2.1: Vehicle driver linear biodynamic model by Boileau and Rakheja [7].

Human body lumped mass models have advantages like less complexity, less demand on computational power, and relatively simpler validation requirements. Such models are capable of producing biofidelic responses and can be used to simulate both kinematics and kinetics of the whole body under specific vibration environments, thus they can allow the prediction of the body vibration exposure levels as well as the design and simulation of control methods for vibration attenuation. Therefore, this type of human body model was selected to model a seated human subject exposed to low frequency whole-body vibration in chapter 3.

2.2 Semi-active and active seat suspensions

As mentioned in Chapter 1, passive seat suspensions are subject to many limitations. As a result semi-active and active seat suspensions have been developed aiming to provide

more effective vibration isolation for vehicle occupants. The typical configurations of semi-active and active vibration suspension systems are shown in Figure 2.2.

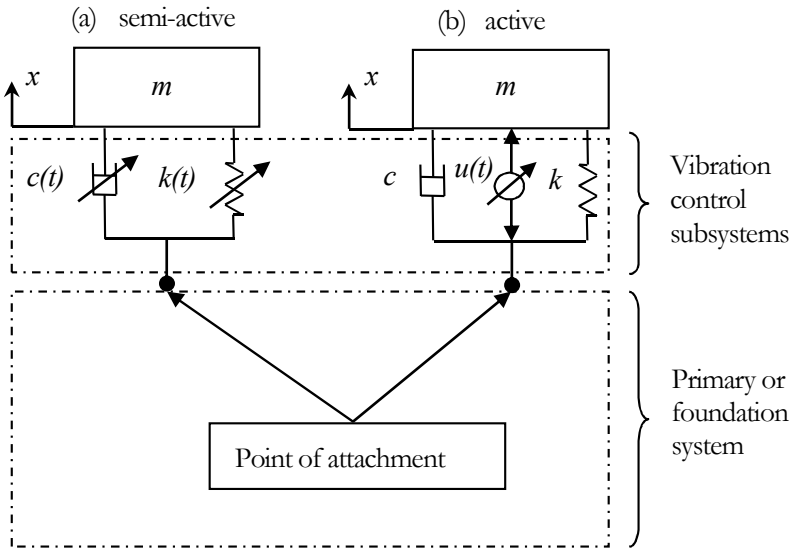

Figure 2.2: Typical configuration of semi-active and active vibration suspension systems.

2.2.1 Semi-active seat suspensions

The fundamental concepts of semi-active (SA) suspensions and vibration control systems were first introduced by Karnopp [32] in 1974. SA suspension systems can only passively modulate damping or spring forces according to a parameter tuning policy with only a small amount of control effort. SA systems, as their name implies, fill the gap between purely passive and fully active vibration control systems. They offer reliability comparable to that of passive systems, yet maintain the versatility and adaptability of fully active systems. During recent years there has been considerable interest towards practical implementation of these systems for their low energy requirement and cost, also, recent advances in smart materials and adjustable dampers, such as electrorheological (ER) and magnetorheological (MR) dampers have significantly contributed to the applicability of these systems.

In recent years, various SA seat suspension systems have been proposed. Wu and Griffin [33] developed a SA seat suspension using an ER fluid damper to reduce the seat impacts caused by shocks or high magnitude vibration. Choi et al. [34] proposed a SA

seat suspension using a MR fluid damper for commercial vehicles. McManus et al. [35] evaluated the vibration and shock attenuation performance of a SA MR fluid damper in reducing the incidence and severity of end-stop impacts of a low natural frequency suspension seat. Hiemenz et al. [36] explored the use of a MR damper in a SA seat suspension system for helicopter crew seats to enhance occupant comfort.

Although SA suspension systems provide some desirable benefits, the force range of SA systems are limited, and they are known to be 'soft' to high frequency excitations while being 'stiff' to low frequency excitations [37]. Thus, the vibration isolation performance in the low frequency range can be compromised.

2.2.3 Active seat suspensions

An active system is one in which the passive components are replaced or augmented by actuators that supply additional forces. Active seat suspensions which can provide much wider force range and achieve better isolation performance in the low frequency region have attracted more and more attention in recent years. For instance, Kawana and Shimogo [38] proposed an active seat suspension for a heavy duty truck using an electric servo-motor and ball-screw mechanism which showed that some resistance will remain even if the control is off. Stein [39] developed an electro-pneumatic active seat suspension for a driver's seat for heavy earth moving equipment or off-road vehicles. Maciejewski et al. [40] presented an active seat suspension system containing a controlled pneumatic spring and a hydraulic shock-absorber. The active control of air-flow to the pneumatic spring was applied by means of a directional servo-valve. Some drawbacks of pneumatic systems were found: They require a large amount of energy to maintain the necessary air pressure in the source, and the complexity of the systems make them less reliable and difficult to control. In a recent study by Chen et al. [37], an adaptive helicopter seat mount using stacked piezoelectric actuators was developed. The seat mount has been retrofitted on a full-scale Bell-412 helicopter co-pilot seat and the performance was evaluated through closed-loop tests. The results showed that significant vibration suppression was achieved. However, the study also found that the stacked piezoelectric actuators can not provide enough stroke to effectively suppress the low frequency vibration.

The actuator is the heart of an active system. Low noise, low power consumption, low cost, physically compact and reliable and enough authority are desirable characteristics for actuators in active systems [41]. Due to the costs, energy demand and complexity, the use of active seat systems is very limited in the current market. One successful use of active seat suspensions is the Bose Ride System for heavy duty trucks [42] as shown in Figure 2.3. Linear electromagnetic actuators are used in this system. According to Bose, the seat suspension is able to counteract broadband vibration from the road and it is proven to reduce driver fatigue and pain.

Figure 2.3: Bose Ride System [42].

2.2.4 Performance Comparison

Based upon the above review, a performance comparison between semi-active and active systems can be made, as seen in Table 2.1.

Table 2.1: Performance comparison between semi-active and active systems.

Features	Cost	Power supply	Control complexity	Adaptability	Isolation performance
Semi-active	++	+	+	+	++
Active	+++	++	++	++	+++

Note: + - low level, +++ - high level.

Semi-active systems have a lower control effort compared with that of active systems. They offer the reliability, yet maintaining some versatility and adaptability. However, semi-active systems can only passively modulate damping or spring forces according to a parameter tuning policy, and they are found to be 'soft' to high frequency excitations while 'stiff' to low frequency excitations, therefore, the vibration isolation performance in low frequency range is still compromised.

Active vibration control systems are the most complex due to the requirement for special actuators, sensors and computing systems, and require an external power supply. But active systems have many desirable advantages, which include providing significantly improved isolation performance in the low frequency range, high adaptability on a large bandwidth, and can be modified as desired by control algorithms to cancel vibration at certain frequencies.

2.3 Semi-active and active vibration control techniques

2.3.1 Semi-active vibration control techniques

There are many control techniques which have been developed and demonstrated to be viable for semi-active (SA) suspension systems. The following sections outline some classical and widely used control techniques for SA systems.

Skyhook control

Skyhook control, originally devised by Karnopp et al. [32], is one of the most effective control strategies for SA vibration control systems. In this kind of control system, a fictitious damper is used to connect the sprung mass to a fixed point in the sky (an inertial reference), as shown in Figure 2.4. The damper exerts a force tending to reduce the absolute velocity of the sprung mass, rather than reduce the relative velocity for conventional dampers. The damper is turned on when the absolute velocity of the sprung mass is the same sign as the relative velocity and switched off when they are opposite, ensuring that the damper force is always dissipative. The conventional skyhook control law requires the damper coefficient to be continuously variable. To simplify the operation an "on-off" skyhook control scheme has been proposed [43].

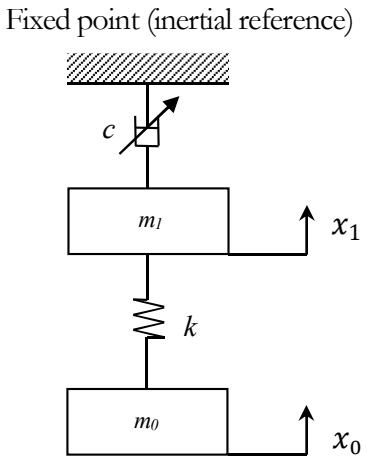

Figure 2.4: Skyhook SA vibration control systems [32].

Balance control

Balance control was first introduced by Rakheja and Sankar in 1985 [44]. It is so-called because it attempts to cancel the spring force in part by the damping force and keep the mass in balance. Balance control also includes "on-off" and continuous versions. In this control method, the damping force tends to increase the acceleration of the mass during the first and third quarters of a cycle when the spring and the damper forces have the same sign, or equivalently when the relative velocity and relative displacement have the same sign. It also tends to decelerate the mass in the second and fourth quarters when the spring and the damper forces have opposite signs. A continuous balance control algorithm has been proposed in [45], which can be considered as a further development of the "on-off" control algorithm. For "on-off" balance control the spring force can be partly cancelled or over-cancelled, while the spring force can be partly or totally cancelled in continuous balance control.

Other SA control methods

As a result of the substantial on-going theoretical advances in this area, many other control methods for SA systems have been proposed, which include: adaptive and nonlinear controls [46], fuzzy reasoning control, sliding mode control [47], ground-hook control [48], anti-jerk continuous skyhook control [49], acceleration-driven-damper control [50].

2.3.2 Active vibration control techniques

The force generated by the actuator is governed by a control law, and some sensors are used to measure error and reference signals which are required by the control law. So far, a variety of control approaches have been developed for active vibration control systems. The following is a short-list of several different types of active control strategies.

Least-Mean-Square (LMS) algorithm

Due largely to its simplicity and robustness, the Least-Mean-Square (LMS) algorithm is the most popular control strategy for active vibration control systems. The LMS algorithm which was originally developed by Widrow and Hoff [51] is an adaptive gradient search approach based on the steepest descent method and does not require squaring, averaging or differentiating. It is a stochastic gradient descent method in that the filter is only adapted based on the error at the current time. The Filter-x LMS (FXLMS) algorithm is one of the most widely used variations of the LMS algorithm. The adaptive nature of FXLMS makes it inherently applicable to non-linear and time-varying systems. It has been found to offer stable and robust performance for a wide class of active noise and vibration cancellation applications.

Examples of applications of FXLMS algorithm include the following. In [52], the FXLMS algorithm was applied to a six-strut Stewart vibration isolation platform which serves as a prototype for a space flight system. The test results show an excellent dynamic performance of the FXLMS controller and over 40 dB vibration reduction is achieved for narrow-band disturbance. The FXLMS algorithm is applied to a flexible cantilever beam for active vibration control in [53]. The control results indicated that a considerable vibration reduction could be achieved in a few seconds. The performance of the FXLMS algorithm for cancelling airfoil vibration and flutter was investigated in [54]. The control method showed good performance in suppressing wing vibration and flutter. In [55], the application of the FXLMS algorithm to active engine mounts is studied in detail. A feed-forward FXLMS algorithm with on-line secondary path identification was applied to an experimental rig to cancel narrow-band engine vibrations. The results show that a significant level of vibration reduction is achieved. The performance was also validated by real-time tests on a saloon car equipped with a turbo-diesel engine. The application of the Filter-x LMS (FXLMS) algorithm to an

adaptive helicopter seat mount is described in [37]. Here the FXLMS algorithm was used to minimize the seat vibration incurred by the N/rev harmonic loads of the main rotor speed. The seat vibration which was directly correlated to the N/rev harmonic loads was selected as the reference signal in this investigation. The test results show a significant global reduction of the body vibration levels is achieved. Although no details of the estimation of the so-called secondary path dynamics (the path from the actuator signal to the measured error signal) are provided.

Because it is assumed that *a priori* knowledge about the plant and disturbance is not available in this investigation, a self-tuning algorithm is a prime requirement. A self-tuning fully adaptive algorithm, such as FXLMS, could control a non-linear time-varying system with unknown initial parameters and would meet the requirements stipulated in the research objectives. Hence, the FXLMS filter with on-line system identification was selected for detailed investigation in Chapter 7.

In addition to the FXLMS control algorithm, there are several control strategies, listed in the following, that could be applied but which have not been considered for detailed investigation either because they offer no computational advantage over the FXLMS algorithm, or due to the requirement for a design procedure based upon knowledge of the system parameters.

Self-tuning regulator

The self-tuning regulator (STR), proposed by Astrom and Wittenmark [56], is a typical adaptive control method and has been used for many applications [57, 58] since the mid-1970s. STRs are inherently nonlinear due to the estimation part and the changing parameters in the controller, which makes the analysis of STRs very complicated and the convergence and stability is difficult to guarantee.

Model reference adaptive control

Model Reference Adaptive Control (MRAC) is a closed loop controller with parameters that can be updated to change the response of the system. The output of the system is compared to a desired response from a reference model. The goal is for the parameters to converge to ideal values that cause the plant response to match the response of the

reference model. Some applications of MRAC to active systems include [59-61]. *A priori* knowledge of the pole-excess and order of the plant are needed to apply the MRAC procedure and empirical evidence indicates that the MRAC algorithm is only stable for small adaption gains, high gains will lead to instability.

Model reaching adaptive control

Model Reaching Adaptive Control's main idea is to design a dynamic manifold for the target, rather than control the plant to follow the model reference [62]. Its derivation is based upon Lyapunov analysis and Barbalat's lemma. This algorithm eliminates the necessity of base or ground vibration measurement, however, it requires to measure the absolute velocity of the isolated mass, and the relative displacement between the isolated mass and base, which make the application of this method very limited in practice.

Linear Quadratic Gaussian (LQG)/H2/H∞ methods

LQG/ H2/ H∞ are optimal control methods. A cost function needs to be formulated before optimization. In [63] a LQG controller was described and applied to active vibration absorbers to reduce disk drive vibration at multiple rotating speeds. An adaptive form of LQG named adaptive-Q controller is applied to vibration isolation in [64]. An H2 control algorithm was applied to control the lateral vibration of a jacket-type offshore platform subjected to wave loading in [65]. In [66] a H∞ based controller was designed and applied to multi-mode structural vibration control in the composite fin-tip of an aircraft. All the above optimal control methods either need *a priori* information about the plant and disturbance or require intensive computation.

2.4 Conclusions

This chapter provides a review of the modelling of seated human subjects under low frequency whole-body vibration and a review of active and semi-active seat suspensions. The advantages and limitations of the two types of suspension are compared. In addition, a summary of the various types of controller that have been applied to active and semi-active vibration control systems is given. The Filter-x Least-Mean-Square

algorithm was selected for detailed investigation in Chapter 7 as it is a self-tuning fully adaptive algorithm which requires no *a priori* knowledge of the system parameters.

Chapter 3

Seated Human Body Modelling and Simulation

In this chapter, the biodynamic responses of seated human subjects (SHS) exposed to uncoupled vertical and fore-and-aft whole-body vibration (WBV) are modelled. The mathematical model can be used to obtain a better insight into the mechanisms and biodynamic behaviour of the SHS system. The main limitation of some previous SHS models is that they were derived to satisfy a single biodynamic response function. Such an approach may provide a reasonable fit with the function data being considered but uncertain matches with the others. The model presented in this study is based on all three types of biodynamic response functions: seat-to-head transmissibility (STHT), driving-point mechanical impedance (DPMI) and apparent mass (APM). The objective of this model is to match all three functions and to represent the biodynamic behaviour of SHS in a more comprehensive way.

3.1 Measurement data of seated human subjects

In order to gain a better understanding of seated human subject biodynamic response and adverse effects under low frequency whole-body vibration, a variety of statistical and analytical studies have been carried out by various researchers. Statistical studies usually involve measuring the kinetic and biodynamic responses of human subjects. There are three types of generalized biodynamic responses functions - seat-to-head transmissibility (STHT), driving-point mechanical impedance (DPMI) and apparent mass (APM), which are widely used to characterize biodynamic response of the seated human subject under most commonly encountered vibration environments. The STHT function is defined as the complex ratio of the output vibration level on the head to the input vibration level on the seat in the frequency range of interest [9]. This can be obtained in different forms by examining different response quantities, such as displacement, velocity and acceleration. The DPMI function is defined as the complex

ratio between the transmitted dynamic force to which the subject is exposed and the input driving-point velocity [7]. The APM function is defined similarly to the DPMI function. It specifies the complex ratio of driving force to the driving-point acceleration. Whilst the DPMI and APM are in principle directly related, they are treated in this thesis as separate quantities since it is unknown exactly how the data had been processed in the original sources. While the STHT function can provide indications on the dynamic behaviour of human body parts which are distant from the driving-point, the DPMI and APM functions can show the biodynamic characteristics of the human body load at the input point. All three functions can be evaluated by calculating the magnitude and phase responses in the frequency range of interest.

It is noted that the biodynamic response data of seated human subjects was obtained from a variety of field and experimental measurements which were carried out under widely varying test conditions [7, 9]. The variation of test conditions for individual measurements may involve both intrinsic and extrinsic variables, such as subject mass and population, seat posture, feet and hand position, vibration excitation type and level, seat backrest angle and measurement location on the subject. In order to avoid significant discrepancies among the measurements data associated with the above variable conditions, the following requirements were specified for the synthesis of the biodynamic characteristics of seated human subjects [7, 67]:

(1) Studies presenting measurement results based on at least six subjects;

(2) The measured subjects are considered to be sitting erect or with upright posture without backrest support for vertical vibration and with backrest support for fore-and-aft vibration, irrespective of the hands' position;

(3) Feet are supported and vibrated on the same excitation base;

(4) Subject mass is limited to the range of 45-100 kg;

(5) Excitation levels are below $5 m/s^2$, and magnitude and phase data are reported in the 0-20 Hz frequency range;

(6) Either sinusoidal or random vibration excitation is used in the measurements.

Based upon the above requirements, the following published measurement data were selected for the synthesis of seated human body biodynamic properties: Paddan and Griffin [9], Boileau and Rakheja [7] and Hinz et al. [68] for the seat-to-head transmissibility (STHT) data; Boileau and Rakheja [7], Fairley and Griffin [69], Hinz and Seidel [70] and Holmlund and Lundström [71] for the driving-point mechanical impedance (DPMI) data; Mansfield and Griffin [72], Toward and Griffin [73], Fairley and Griffin [74] and Qiu and Griffin [75] for the apparent mass (APM) data. The aggregated data, shown in Table 3.1 and 3.2, is derived by averaging the above data sets (magnitude and phase data sets are averaged separately) within the frequency range of interest. Picking off values from curves are used for some frequencies at which the measured values are not provided in the original sources.

Table 3.1: Aggregated data of STHT, DPMI and APM mean values in the vertical direction.

Frequency (Hz)	**STHT (abs)**		**DPMI (N*s/m)**		**APM (kg)**	
	Magnitude	Phase (deg)	Magnitude	Phase (deg)	Magnitude	Phase (deg)
0.5	1.01	-0.2	95	89.5	59	-2.2
0.75	1.00	-0.7	175	89.0	60	-2.3
1.0	1.01	-0.8	310	88.5	60	-3.5
2.0	1.10	-6.0	754	87.5	61	-4.5
3.0	1.16	-10.0	1255	82	71	-10
4.0	1.28	-17.5	2252	66	81	-15
4.5	1.37	-29	2704	45	80	-23
5.0	1.45	-40	2605	31	76	-31
5.5	1.43	-50	2254	23	67	-43
6.0	1.30	-61	2105	23	53	-55
6.5	1.18	-62	1865	20	48	-60
7.0	1.09	-60	1892	22	44	-64
8.0	0.99	-62	1998	21	39	-68
9.0	0.94	-70	2002	20	36	-70
10.0	0.95	-76	2015	16	32	-72
12.0	0.86	-85	1905	17	31	-80
14.0	0.76	-97	1770	18	25	-83
16.0	0.67	-105	1625	19	18	-82
18.0	0.60	-113	1585	20	14	-81
20.0	0.56	-121	1605	20	11	-81

Table 3.2: Aggregated data of STHT, DPMI and APM mean values in the fore-and-aft direction.

Frequency (Hz)	STHT (abs)		DPMI (N*s/m)		APM (kg)	
	Magnitude	Phase (deg)	Magnitude	Phase (deg)	Magnitude	Phase (deg)
0.5	1.26	-1	55	83.0	53.0	-8.0
0.75	1.44	-16	148	80.8	57.0	-10.6
1.0	1.62	-40	257	76.6	59.5	-12.8
1.25	1.59	-64	392	71.55	63.1	-16.0
1.5	1.41	-85	515	65.4	67.2	-20.2
1.75	1.23	-103	655	59.5	69.6	-24.0
2.0	1.10	-119	850	48.4	70.2	-28.5
2.5	0.86	-135	1010	33.6	62.5	-39.4
2.75	0.71	-144	1068	25.0	58.6	-46.0
3.0	0.56	-159	1095	17.1	54.0	-53.5
3.5	0.41	-168	1083	1.8	45.1	-62.5
4.0	0.29	-175	1061	-7.5	37.7	-75.0
4.5	0.26	-189	1028	-15.5	35.3	-80.5
5.0	0.23	-198	974	-21.5	30.6	-81.0
6.0	0.18	-211	912	-25.8	20.5	-86.2
7.0	0.13	-231	853	-29.0	17.4	-91.0
8.0	0.10	-247	746	-29.8	12.9	-90.2
9.0	0.08	-253	647	-29.3	10.3	-87.0
10.0	0.08	-255	555	-28.0	7.8	-85.0
11.0	0.08	-254	521	-27.2	7.2	-84.0
12.0	0.08	-252	487	-25.7	6.0	-84.0

The lower and upper limits of each data are not included in the above tables. However, they are shown in the simulation results. It is noted that sufficient measurement data of STHT, DPMI and APM responses in the fore-and-aft direction is only available up to 12 Hz.

3.2 Model description

The developed model is a lumped-parameter linear spring and damper system. The model includes segments representing appropriate anatomical parts of the body and is capable of accommodating translational and rotational (head and neck joint) movements of these segments, which enable it to represent the measured STHT, DPMI and APM function data under low frequency whole-body vibration.

This model is composed of two sub-models: the vertical model and the fore-and-aft model (uncoupled), as shown in Figure 3.1. The vertical model consists of five segments: head and neck (m_5), upper torso (m_4), arms (m_3), viscera (m_2), and lower torso (m_1). The spring (k_{41}) and damper (c_{41}) connecting the upper and lower torsos represent the body spine. In the fore-and-aft model, the main body mass (m_1+ m_2+ m_3+ m_4) is treated as a single lumped mass. The head and neck (m_5) and the main body are connected by a rotational degree of freedom. These rigid masses are coupled by linear elastic and damping elements. The masses of the lower legs and the feet are not incorporated in the model representation, assuming their negligible contributions to the whole-body biodynamic response. This assumption is in agreement with the evidence that the contribution of the supported legs to the whole-body vibration is relatively insignificant when both the seat and the footrest are vibrated under the same excitation.

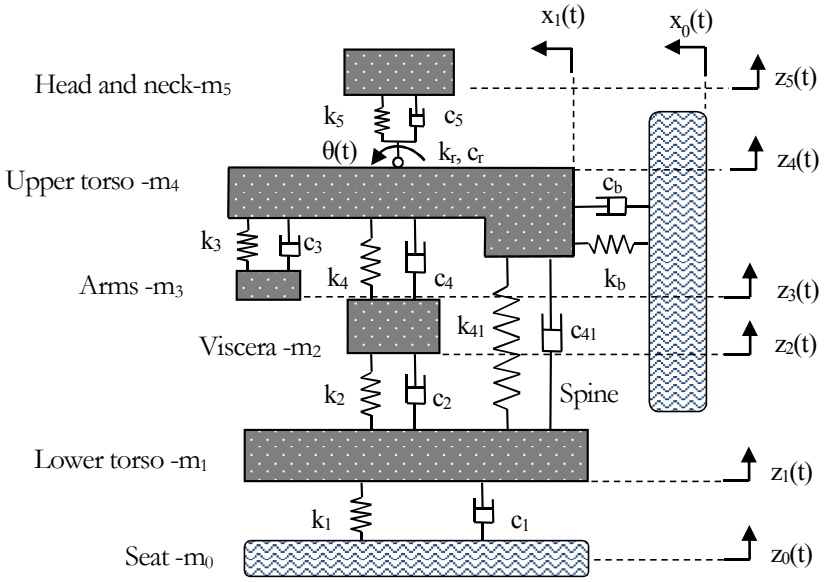

Figure 3.1: Schematic of model for seated human subjects in both vertical and fore-and-aft directions.

3.3 Equations of motion (EOMs)

EOMs of the model were derived from the free-body diagram of each part. The vertical model has five degrees of freedom in total: the vertical displacement of each segment $\{z_1(t),\ z_2(t),\ z_3(t),\ z_4(t),\ z_5(t)\}$. The vertical model EOMs can be expressed by the following coupled differential equations:

$$m_1\ddot{z}_1 + c_1(\dot{z}_1 - \dot{z}_0) + k_1(z_1 - z_0) - c_2(\dot{z}_2 - \dot{z}_1) - k_2(z_2 - z_1) - c_{41}(\dot{z}_4 - \dot{z}_1) - k_{41}(z_4 - z_1) = 0 \quad (3.1)$$

$$m_2\ddot{z}_2 + c_2(\dot{z}_2 - \dot{z}_1) + k_2(z_2 - z_1) - c_4(\dot{z}_4 - \dot{z}_2) - k_4(z_4 - z_2) = 0 \quad (3.2)$$

$$m_3\ddot{z}_3 - c_3(\dot{z}_4 - \dot{z}_3) - k_3(z_4 - z_3) = 0 \quad (3.3)$$

$$m_4\ddot{z}_4 + c_3(\dot{z}_4 - \dot{z}_3) + k_3(z_4 - z_3) + c_4(\dot{z}_4 - \dot{z}_2) + k_4(z_4 - z_2) + \mathrm{c}_{41}(\dot{\mathrm{z}}_4 - \dot{\mathrm{z}}_1) + \mathrm{k}_{41}(\mathrm{z}_4 - \mathrm{z}_1) - \mathrm{c}_5(\dot{\mathrm{z}}_5 - \dot{\mathrm{z}}_4) - \mathrm{k}_5(\mathrm{z}_5 - \mathrm{z}_4) = 0 \quad (3.4)$$

$$m_5\ddot{z}_5 + c_5(\dot{z}_5 - \dot{z}_4) + k_5(z_5 - z_4) = 0 \quad (3.5)$$

The above differential equations can be expressed in matrix form:

$$[\boldsymbol{M}]\{\ddot{\boldsymbol{z}}\} + [\boldsymbol{C}]\{\dot{\boldsymbol{z}}\} + [\boldsymbol{K}]\{\boldsymbol{z}\} = \{\boldsymbol{f_n}\} \quad (3.6)$$

where $[\boldsymbol{M}]$, $[\boldsymbol{C}]$ and $[\boldsymbol{K}]$ are mass, damping and stiffness matrices with a size of 5×5, respectively; $\{\ddot{\boldsymbol{z}}\}$, $\{\dot{\boldsymbol{z}}\}$ and $\{\boldsymbol{z}\}$ are acceleration, velocity and displacement vectors, respectively, with a size of 5×1; $\{\boldsymbol{f_n}\}$ is an 5×1 excitation force vector. All the above matrices and vectors can be expressed as follows:

$$[\boldsymbol{M}] = \begin{bmatrix} m_1 & 0 & 0 & 0 & 0 \\ 0 & m_2 & 0 & 0 & 0 \\ 0 & 0 & m_3 & 0 & 0 \\ 0 & 0 & 0 & m_4 & 0 \\ 0 & 0 & 0 & 0 & m_5 \end{bmatrix};$$

$$[\boldsymbol{C}] = \begin{bmatrix} c_1 + c_2 + c_{41} & -c_2 & 0 & -c_{41} & 0 \\ -c_2 & c_2 + c_4 & 0 & -c_4 & 0 \\ 0 & 0 & c_3 & -c_3 & 0 \\ -c_{41} & -c_4 & -c_3 & c_3 + c_4 + c_{41} + c_5 & -c_5 \\ 0 & 0 & 0 & -c_5 & c_5 \end{bmatrix};$$

$$[\boldsymbol{K}] = \begin{bmatrix} k_1 + k_2 + k_{41} & -k_2 & 0 & -k_{41} & 0 \\ -k_2 & k_2 + k_4 & 0 & -k_4 & 0 \\ 0 & 0 & k_3 & -k_3 & 0 \\ -k_{41} & -k_4 & -k_3 & k_3 + k_4 + k_{41} + k_5 & -k_5 \\ 0 & 0 & 0 & -k_5 & k_5 \end{bmatrix};$$

$$\{\ddot{\boldsymbol{z}}\} = \begin{Bmatrix} \ddot{z}_1 \\ \ddot{z}_2 \\ \ddot{z}_3 \\ \ddot{z}_4 \\ \ddot{z}_5 \end{Bmatrix};\ \{\dot{\boldsymbol{z}}\} = \begin{Bmatrix} \dot{z}_1 \\ \dot{z}_2 \\ \dot{z}_3 \\ \dot{z}_4 \\ \dot{z}_5 \end{Bmatrix};\ \{\boldsymbol{z}\} = \begin{Bmatrix} z_1 \\ z_2 \\ z_3 \\ z_4 \\ z_5 \end{Bmatrix};\ \{\boldsymbol{f_n}\} = \begin{Bmatrix} c_1\dot{z}_0 + k_1 z_0 \\ 0 \\ 0 \\ 0 \\ 0 \end{Bmatrix}.$$

The fore-and-aft model has two degrees of freedom in total: the fore-and-aft displacement of the main body part $x_1(t)$ and the head and neck rotational degree $\theta(t)$. The EOMs of the fore-and-aft model can be expressed by the following differential equations:

$$\mathrm{M}\ddot{x_1} + m_5 l_n \ddot{\theta}\cos\theta - m_5 l_n \dot{\theta}^2 \sin\theta + k_b(x_1 + x_0) + c_b(\dot{x_1} + \dot{x_0}) = 0 \quad (3.7)$$

$$m_5 {l_n}^2 \ddot{\theta} + m_5 l_n \ddot{x_1}\cos\theta - m_5 l_n g \sin\theta + k_t\theta + c_t\dot{\theta} = 0 \quad (3.8)$$

where M is the mass of the whole body ($\mathrm{M}= m_1+ m_2+ m_3+ m_4+ m_5$), l_n is the average distance between the shoulder and the gravity centre of the head, g is the acceleration due to gravity. k_t and c_t are the rotational spring and damper coefficients of the neck, k_b and c_b are the spring and damper coefficients between the main body and the backrest, respectively.

3.4 EOMs solution in the frequency domain

By taking Fourier transforms of the above EOMs the models can be analysed in the frequency domain. The Fourier transform of the vertical model EOMs (Equation (3.6)) results in:

$$\{\boldsymbol{Z}(j\omega)\} = \left[-\omega^2[\boldsymbol{M}] + j\omega[\boldsymbol{C}] + [\boldsymbol{K}]\right]^{-1}\{\boldsymbol{F_n}(j\omega)\} \tag{3.9}$$

where $\{\boldsymbol{Z}(j\omega)\}$ and $\{\boldsymbol{F_n}(j\omega)\}$ are the complex Fourier transform vectors of $\{\boldsymbol{z}\}$ and $\{\boldsymbol{f_n}\}$, respectively, j is the imaginary unit and ω is the angular frequency. The vector $\{\boldsymbol{Z}(j\omega)\}$ contains the complex displacement responses of the 5 mass segments as a function of angular frequency, and they can be represented by $\{\boldsymbol{Z_1}(j\omega),\ \boldsymbol{Z_2}(j\omega),\ \boldsymbol{Z_3}(j\omega),\ \boldsymbol{Z_4}(j\omega),\ \boldsymbol{Z_5}(j\omega)\}$. $\{\boldsymbol{F_n}(j\omega)\}$ contains the complex excitation forces as a function of angular frequency as well, which is $\{(k_1 + j\omega c_1)\boldsymbol{Z_0}(j\omega), 0, 0, 0, 0\}$, where $\boldsymbol{Z_0}(j\omega)$ is the complex displacement of excitation. The EOMs of the fore-and-aft model contain some nonlinear terms $-m_5 l_n \ddot{\theta}\cos\theta$, $-m_5 l_n \dot{\theta}^2 \sin\theta$, $m_5 l_n \ddot{x}_1 \cos\theta$, $-m_5 l_n g \sin\theta$. Small oscillations were assumed (i.e. around $\theta = 0$), and the following linearization were used: $\cos\theta = 1$, $\sin\theta = \theta$, $\dot{\theta}^2 \sin\theta = 0$. The Fourier transform of the linearized equations can be expressed as follows:

$$-\omega^2 \mathrm{M}\mathbf{X_1}(j\omega) - \omega^2 m_5 l_n \boldsymbol{\theta}(j\omega) + (k_b + j\omega c_b)(\mathbf{X_1}(j\omega) - \mathbf{X_0}(j\omega)) = 0 \tag{3.10}$$

$$-\omega^2 m_5 {l_n}^2 \boldsymbol{\theta}(j\omega) - \omega^2 m_5 l_n \mathbf{X_1}(j\omega) + m_5 l_n g \boldsymbol{\theta}(j\omega)$$

$$+(k_t + j\omega c_t)\boldsymbol{\theta}(j\omega) = 0 \tag{3.11}$$

Based on the preceding definitions, the STHT, DPMI and APM biodynamic functions for the vertical model can be derived as follows:

$$\mathrm{STHT\_v} = \frac{\boldsymbol{Z_5}(j\omega)}{\boldsymbol{Z_0}(j\omega)} \tag{3.12}$$

$$\mathrm{DPMI\_v} = \left|\frac{(k_1 + j\omega c_1)[\boldsymbol{Z_0}(j\omega) - \boldsymbol{Z_1}(j\omega)]}{j\omega \boldsymbol{Z_0}(j\omega)}\right| \tag{3.13}$$

$$\text{APM\_v} = \left|\frac{\text{DPMI\_v}}{j\omega}\right| = \left|\frac{(k_1 + j\omega c_1)[\boldsymbol{Z_0}(j\omega) - \boldsymbol{Z_1}(j\omega)]}{-\omega^2 \boldsymbol{Z_0}(j\omega)}\right| \tag{3.14}$$

Considering the Equation (3.10) and (3.11) of the fore-and-aft model in a similar manner, the STHT, DPMI and APM biodynamic functions for the fore-and-aft model can be derived as follows:

$$\text{STHT\_f} = \frac{l_n \boldsymbol{\theta}(j\omega) + \mathbf{X_1}(j\omega)}{\mathbf{X_0}(j\omega)} \tag{3.15}$$

$$\text{DPMI}_\text{f} = \left|\frac{(k_b + j\omega c_b)(\mathbf{X_1}(j\omega) - \mathbf{X_0}(j\omega))}{j\omega \mathbf{X_0}(j\omega)}\right| \tag{3.16}$$

$$\text{APM\_f} = \left|\frac{\text{DPMI\_f}}{j\omega}\right| = \left|\frac{(k_b + j\omega c_b)(\mathbf{X_1}(j\omega) - \mathbf{X_0}(j\omega))}{-\omega^2 \mathbf{X_0}(j\omega)}\right| \tag{3.17}$$

3.5 Model parameter identification

Model parameters were identified using curve fitting methods formulated in Matlab (version 2011b). The Least Absolute Residual (LAR) method and the 'Trust-Region' algorithm are used. The fitting process involves the solution of a multivariable optimization function comprising the root mean square errors between the computed values using the model and those target values measured experimentally (Tables 3.1 and 3.2). In the vertical model there are 17 unknown parameters in total, which can be represented in a vector as: $p_v = [c_1,\ c_2,\ c_3,\ c_4,\ c_{41},\ c_5,\ k_1,\ k_2,\ k_3,\ k_4,\ k_{41},\ k_5,\ m_1,\ m_2,\ m_3,\ m_4,\ m_5]^{\mathrm{T}}$. Since the mass $(m_1,\ m_2,\ m_3,\ m_4,\ m_5)$ are shared parameters, in the fore-and-aft model the unknown parameters vector can be expressed as: $p_f = [c_b,\ c_t,\ k_b, k_t,\ l_n]^{\mathrm{T}}$. The vectors p_v and p_f were identified by fitting the biodynamic functions in Equations (3.12-3.17) independently. The final values of the parameters were obtained by averaging the three sets of identified values.

In order to make the fitting procedure more effective, a set of initial, upper and lower limit values were estimated by referring to previously published studies. 73.6% (percentage of body mass supported by the seat for erect seating posture) of the whole

body weight (75 kg) is used for the total model mass (i.e. 73.6% of 75kg =55.2kg). The damping and stiffness coefficients of the human body segments are not known precisely, therefore, the ranges are relatively large. The estimated initial, upper and lower limit values are listed in Table 3.3. The identified model parameters are listed in Table 3.4.

Table 3.3: Estimated initial, upper and lower limits values for model parameter identification.

Model parameters	**Initial values**	**Lower limits**	**Upper limits**
Head and neck mass m_5 (kg)	5.5	5	7
Upper torso mass m_4 (kg)	22	20	25
Arms mass m_3 (kg)	6	5	8
Viscera mass m_2 (kg)	10.2	8	12
Lower torso mass m_1 (kg)	11.7	10	15
Average distance l_n (m)	0.16	0.13	0.19
Damping coefficient c_1 (Ns/m)	2000	500	5000
Damping coefficient c_2 (Ns/m)	1000	400	5000
Damping coefficient c_3 (Ns/m)	300	100	2000
Damping coefficient c_4 (Ns/m)	4000	400	5000
Damping coefficient c_{41} (Ns/m)	4000	500	5000
Damping coefficient c_5 (Ns/m)	400	300	2000
Damping coefficient c_b (Ns/m)	200	10	3000
Damping coefficient c_t (Ns/m)	200	10	2000
Stiffness coefficient k_1 (N/m)	120000	5000	200000
Stiffness coefficient k_2 (N/m)	6000	5000	100000
Stiffness coefficient k_3 (N/m)	10000	5000	200000
Stiffness coefficient k_4 (N/m)	7000	5000	100000
Stiffness coefficient k_{41} (N/m)	160000	5000	250000
Stiffness coefficient k_5 (N/m)	300000	5000	500000
Stiffness coefficient k_b (N/m)	10000	500	200000
Stiffness coefficient k_t (N/m)	1000	500	200000

Table 3.4: Identified parameter values for the vertical and fore-and-aft human body models.

Model parameters	Identified values	Model parameters	Identified values
Head and neck mass m_5 (kg)	5.6	Damping coefficient c_5 (Ns/m)	977
Upper torso mass m_4 (kg)	20.3	Damping coefficient c_b (Ns/m)	6210
Arms mass m_3 (kg)	8.0	Damping coefficient c_t (Ns/m)	19
Viscera mass m_2 (kg)	9.2	Stiffness coefficient k_1 (N/m)	120000
Lower torso mass m_1 (kg)	10.0	Stiffness coefficient k_2 (N/m)	5300
Average distance l_n (m)	0.19	Stiffness coefficient k_3 (N/m)	13200
Damping coefficient c_1 (Ns/m)	2380	Stiffness coefficient k_4 (N/m)	9150
Damping coefficient c_2 (Ns/m)	676	Stiffness coefficient k_{41} (N/m)	128000
Damping coefficient c_3 (Ns/m)	146	Stiffness coefficient k_5 (N/m)	292000
Damping coefficient c_4 (Ns/m)	1800	Stiffness coefficient k_b (N/m)	9930
Damping coefficient c_{41} (Ns/m)	4020	Stiffness coefficient k_t (N/m)	772

3.6 Simulation and comparison results

After all the model parameters have been identified, the magnitude and phase responses of the STHT, DPMI and APM biodynamic functions were simulated in Matlab. The simulation results are presented in Figure 3.2 to 3.7. To evaluate the goodness-of-fit (GOF) of the presented models, the ratio of the root-mean-square error to the mean value was calculated using the following equation [67]:

(3.18)

$$GOF = 1 - \frac{\sqrt{\sum(\boldsymbol{y_m} - \boldsymbol{y_c})^2/(N-2)}}{\sum \boldsymbol{y_m}/N}$$

where $\boldsymbol{y_m}$ and $\boldsymbol{y_c}$ are the measured target data and calculated value, respectively. N is the number of the measured target data points. The GOF statistic can take on any value less than or equal to 1, with a value closer to 1 indicating a better fit. The GOF values of the seated human subject models in the comparison are summarized in Table 3.5. It is noted that in the figures and Table 3.5, any GOF value less than 0 is marked by ~.

In the simulation results, four previous seated human subject models were selected for comparison: a four-DOF linear vertical model developed by Wan and Schimmels [76], which has been found to provide the highest average goodness-of-fit in [67], and a four-DOF vehicle driver model proposed by Boileau and Rakheja [7] were chosen for the vertical model comparison; a two-DOF fore-and-aft model developed by Stein et al. [77] and a four-DOF fore-and-aft apparent mass model presented by Qiu and Griffin [78] were selected for the fore-and-aft model comparison. The schematics and parameters of the comparison models are listed in Table 3.6.

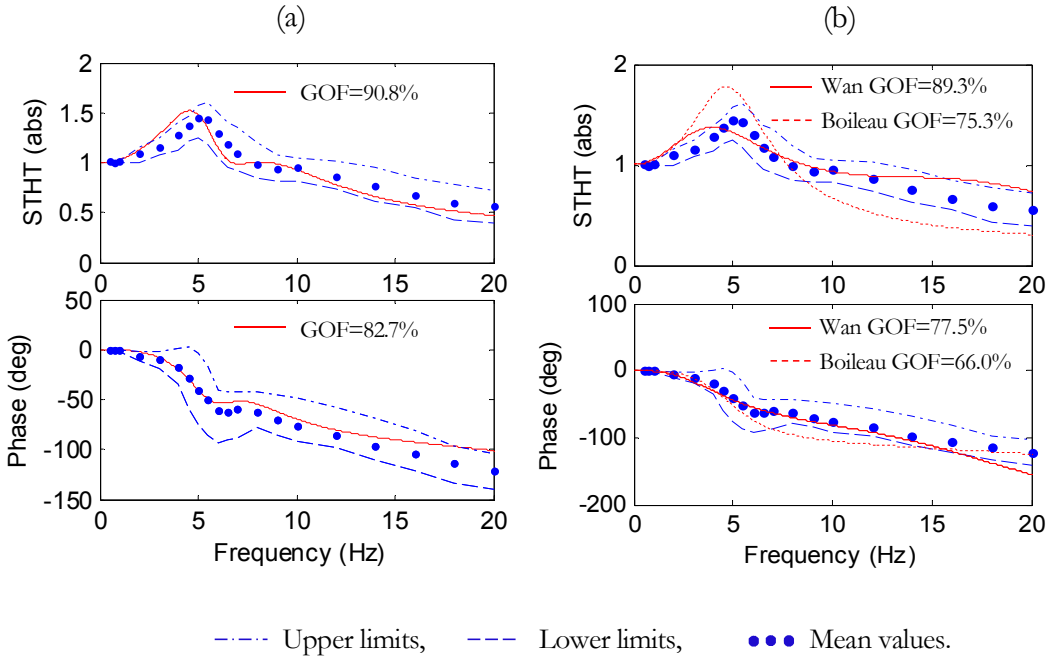

Figure 3.2: Vertical model STHT magnitude and phase responses. (a) Presented model; (b) Wan's and Boileau's models.

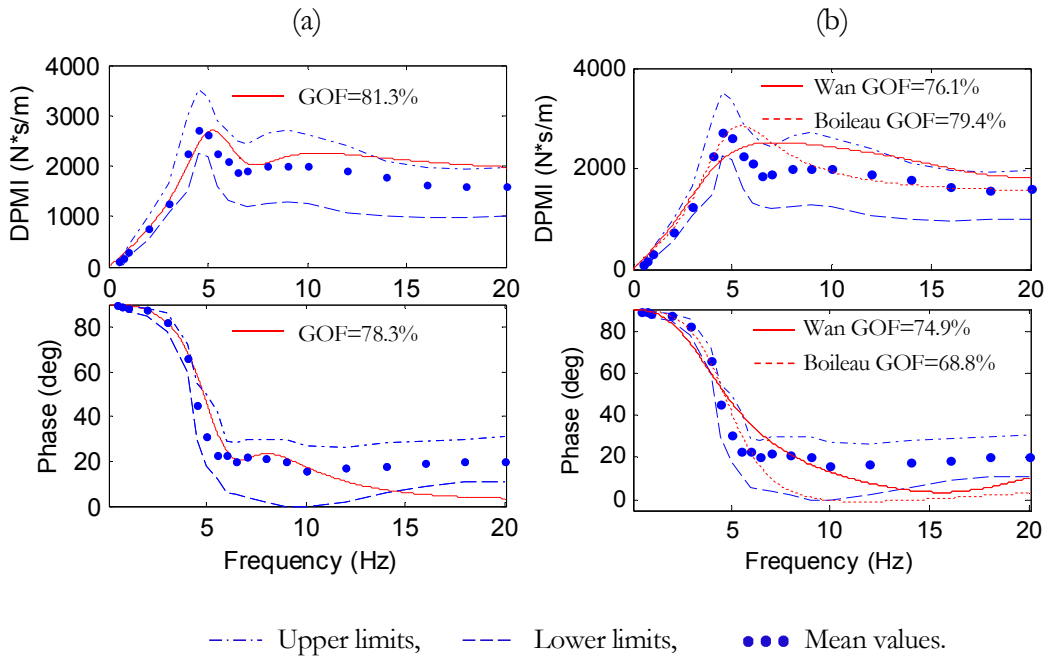

Figure 3.3: Vertical model DPMI magnitude and phase responses. (a) Presented model; (b) Wan's and Boileau's models.

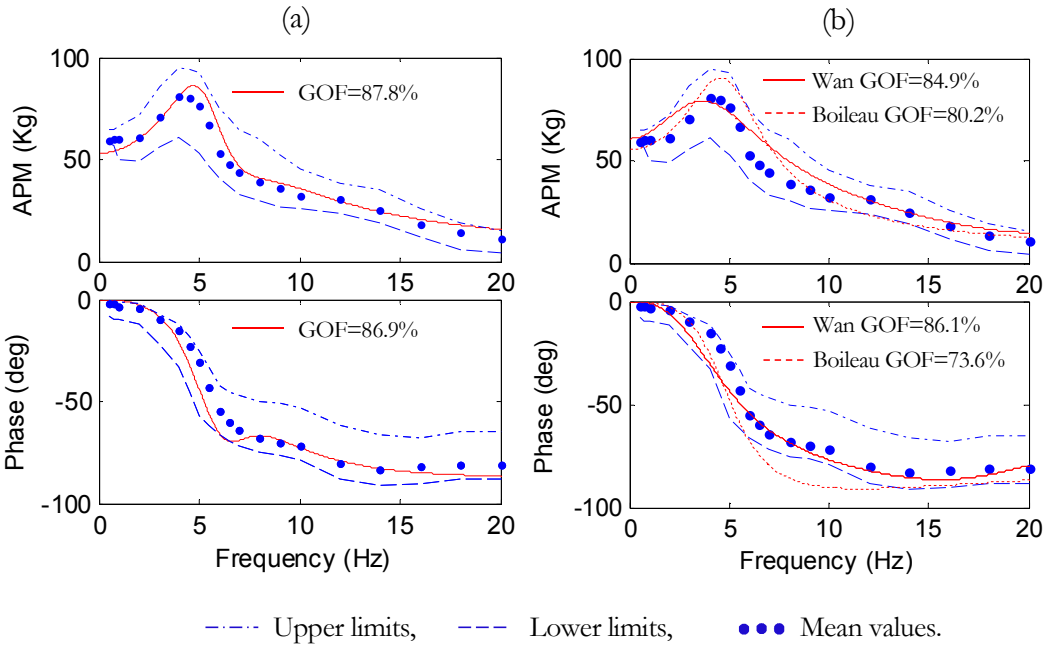

Figure 3.4: Vertical model APM magnitude and phase responses. (a) Presented model; (b) Wan's and Boileau's models.

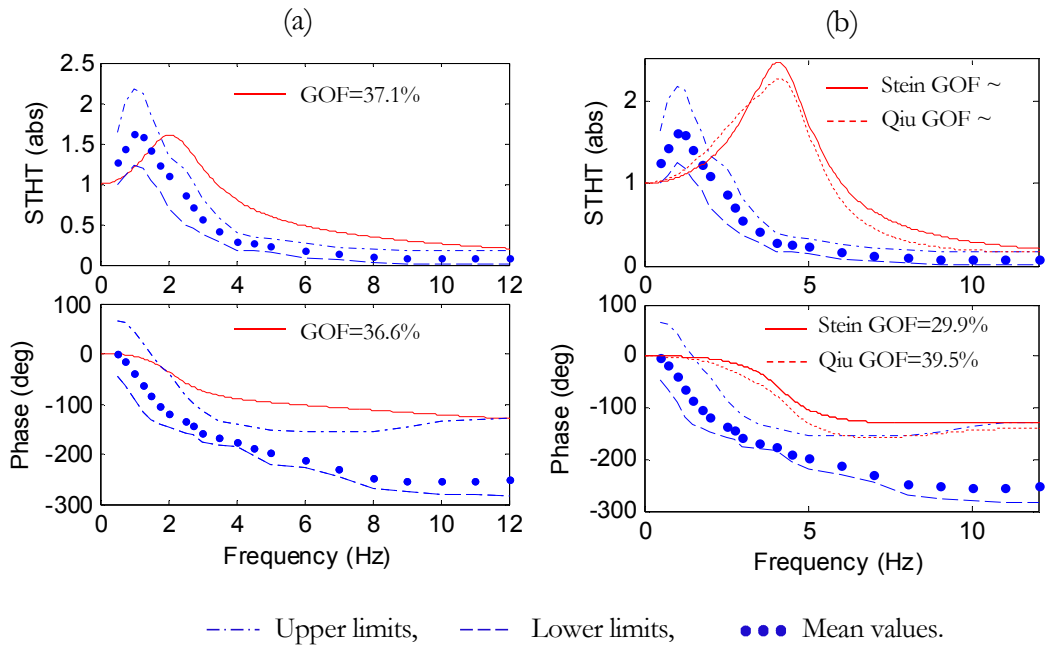

Figure 3.5: Fore-and-aft model STHT magnitude and phase responses. (a) Presented model; (b) Stein's and Qiu's models.

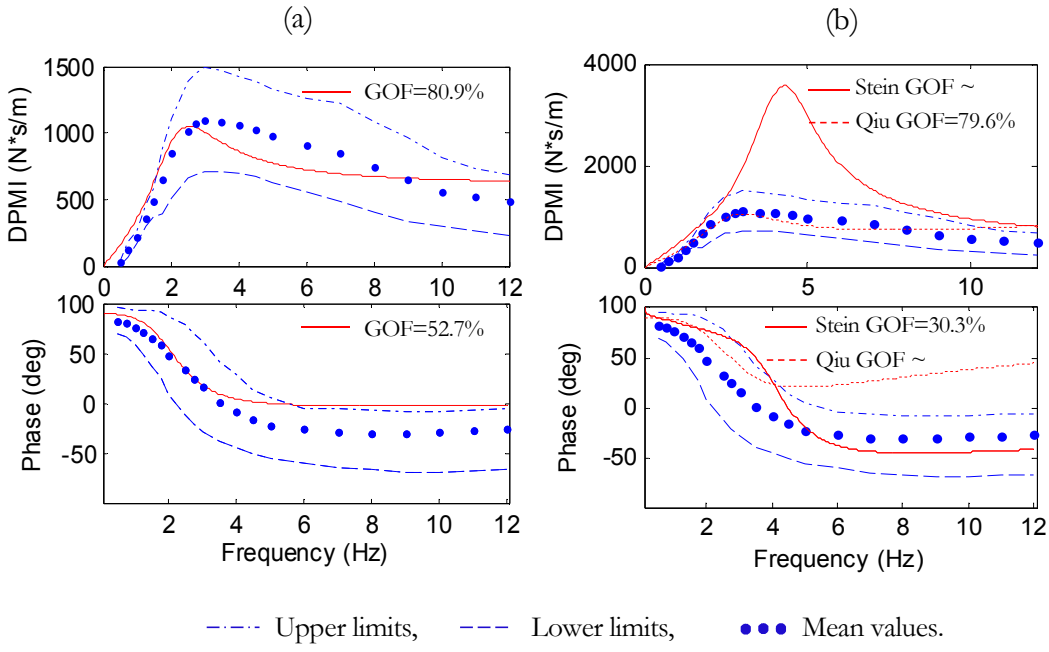

Figure 3.6: Fore-and-aft model DPMI magnitude and phase responses. (a) Presented model; (b) Stein's and Qiu's models.

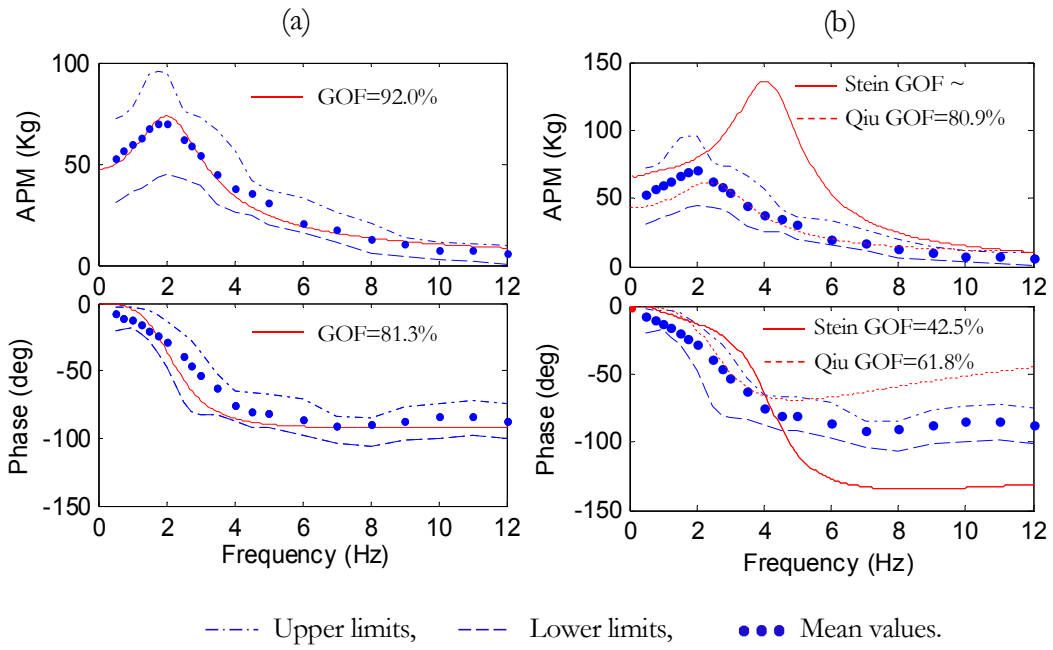

Figure 3.7: Fore-and-aft model APM magnitude and phase responses. (a) Presented model; (b) Stein's and Qiu's models.

Table 3.5: Summary of comparison results of the seated human subject models.

Direction	Model Name	STHT GOF (%)		DPMI GOF (%)		APM GOF (%)	
		Magnitude	Phase	Magnitude	Phase	Magnitude	Phase
Vertical	Presented	90.8	82.7	81.3	78.3	87.8	86.9
	Wan's model	89.3	77.5	76.1	74.9	84.9	86.1
	Boileau's	75.3	66.0	79.4	68.8	80.2	73.6
Fore-and-aft	Presented	37.1	36.6	80.9	52.7	92.0	81.3
	Stein's model	~	29.9	~	30.3	~	42.5
	Qiu's model	~	39.5	79.6	~	80.9	61.8

Table 3.6: Schematics and parameters of comparison models of seated human subject.

Model Name	Model parameters						Schematic of model
	Mass (kg)		Stiffness (N/m)		Damping (Ns/m)		
Wan and Schimmels [76]	m_1	36.0	k_1	49340	c_1	2475.0	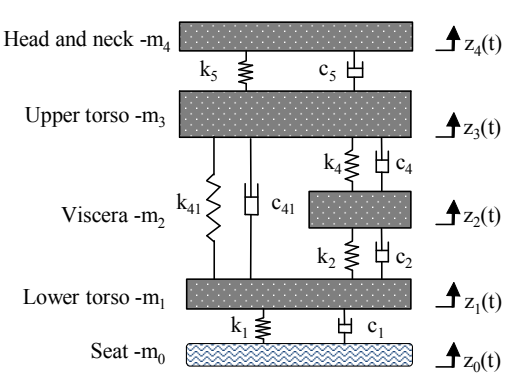
	m_2	5.5	k_2	20000	c_2	330.0	
	m_3	15.0	k_4	192000	c_{41}	909.1	
	m_4	4.17	k_4	10000	c_4	200.0	
			k_5	134400	c_5	250.0	
Boileau and Rakheja [7]	m_1	12.78	k_1	90000	c_1	2064	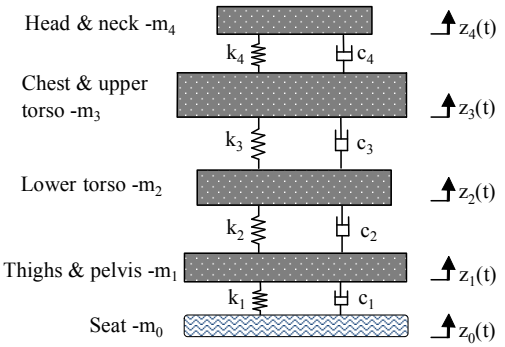
	m_2	8.62	k_2	162800	c_2	4585	
	m_3	28.49	k_3	183000	c_3	4750	
	m_4	5.31	k_4	310000	c_4	400	
Stein et al. [77]	m_1	54	k_1	39322	c_1	465.9	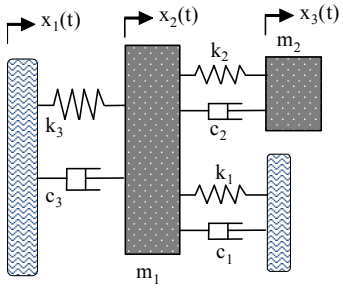
	m_2	10.4	k_2	9	c_2	8.0	
			k_3	1054	c_3	113.1	
Qiu and Griffin [78]	m_b	8	k_1	39886	c_1	359	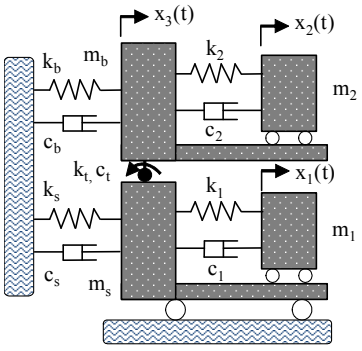
	m_s	10	k_2	10924	c_2	542	
	m_1	20	k_b	24610	c_b	0.0	
	m_2	35	k_t	10	c_t	112	
			k_s	26646	c_s	0.0	

3.7 Discussions

Since there is some variation between the aggregated targets data used in these models, the calculated GOF of the comparison models may not be the original presented values. The measurement condition of the target data used in Stein's model varies somewhat from those of the aggregated target data in the fore-and-aft direction. However, the target data used in Wan, Boileau and Qiu's models are very close to the aggregated target data in this study.

From the simulation results, the vertical seated human models show a higher average goodness-of-fit than the fore-and-aft models in both the magnitude and phase responses of the STHT, DPMI and APM functions. The presented vertical model provides 90.8% GOF and 82.7% GOF for the STHT magnitude and phase responses, 81.3% GOF and 78.3% GOF for the DPMI magnitude and phase responses , 87.8% GOF and 86.9% GOF for the APM magnitude and phase responses, respectively. This indicates that a better overall GOF is achieved for predicting the above biodynamic functions for the seated human subject under vertical vibration. The results also show that very close peaks occur at about 5 Hz in the magnitude responses of all three functions, which indicates the reliability of predicting identical primary resonant frequencies are validated by each other. In addition, the presented vertical model predicts a second resonant frequency around 8 Hz which is observed in the target data. Wan's model has been found to provide a generally good fit for the STHT and APM functions. However, the fit for the DPMI function is relatively poor, with 76.1% GOF for magnitude response and 74.9% GOF for phase response. The peak values occur at about 4 Hz for the STHT and APM functions while the peak value is around 7.5 Hz for the DPMI function.

The fore-and-aft model simulation results exhibit a relatively large deviation. The presented model provides the highest match for the APM function, with 92.0% GOF for magnitude response and 81.3% GOF for phase response. The GOF values for the DPMI function are relatively lower, with 80.9% for magnitude response and 52.7% for phase response. The prediction for the STHT function is the poorest for all the three models. The GOF values for both magnitude and phase responses are below 40%. Because of the variation between the measurement data, Stein's model shows poor matches for all the three functions. Qiu's model provides a reasonably good fit for the

APM function, but poor fits for the other two functions. One of the reasons is that the model was developed based only on the APM measurement data.

It is noted that the quantity of reported experimental data for the seated human subject responses in the fore-and-aft direction is considerably less than the data in the vertical direction. More measurement data is needed to guide and validate the human body modelling in the fore-and-aft direction. It is also noted that the phase responses of the three biodynamic functions are usually measured in experimental studies; however, they are rarely evaluated and analysed in human body modelling studies. The phase responses of the biodynamic functions are evaluated in this study since the phase responses can be equally as important as the magnitude responses, if not more so, when it comes to human body vibration cancellation.

3.8 Conclusions

A lumped-parameter biodynamic model of a seated human subject exposed to low frequency whole-body vibration in both the vertical and fore-and-aft directions has been developed. Model parameters were identified using curve fitting methods and the STHT, DPMI and APM biodynamic magnitude and phase response functions were simulated in Matlab. The goodness-of-fit of the presented model has been evaluated graphically and statistically. A comparison with the existing models was carried out and the results show that an improved fit with the aggregated experimental data is achieved. Through the model, the biodynamic behaviour of seated human subjects can be observed in a more comprehensive way. The developed model can also be used to help in developing anthropodynamic mannequins for vibration assessment.

Chapter 4

Measurements of Vehicle Seat and Test Dummy Vibration Transmissibility

In this chapter, experimental measurements of the vibration transmissibility of a test dummy and vehicle seat are presented. The test dummy was designed and built to represent the dynamic response of a seated human subject and was used in active seat vibration cancellation tests. The aim of these measurements was to characterise the dynamic response of the test dummy and to further investigate the overall vibration isolation efficiency of vehicle seats.

4.1 Experimental setup

4.1.1 Vehicle seat

A standard polyurethane foam (PUF) cushion car seat was used in the experimental measurements. The total mass of the seat is 10.2 kg. The seat consisted of a backrest and a seat pan, the backrest reclined at 9.8^{o} to the vertical and the seat pan inclined at 15.9^{o} to the horizontal. The seat pan frame was attached on a rail mechanism through which the horizontal position could be adjusted. The seat was rigidly mounted on the platform of the multi-axis vibration simulation table (MAST) using screws, as shown in Figure 4.1 (a).

4.1.2 Test dummy

A vibration test dummy was designed and built based on the developed model in Chapter 3 to represent the dynamic response of a seated human subject. The dummy has three segments: the head, upper torso and lower torso (including pelvis and thighs). Each segment

is filled with sand bag cushioned by foam, and the segments are connected by rubber joints to provide stiffness and damping. The total mass of the dummy is 55.2 kg.

Once fully tested and calibrated, the dummy can be used as a seated human body substitute in the active seat vibration cancellation test in order to ensure an improved consistency in behaviour and avoid safety and ethical issues. The dynamic response of the test dummy was characterised by measuring the vibration transmissibility under two experimental setups: car seat setup and solid seat setup, as shown in Figure 4.1 (c) and (d). The dummy was secured using a standard seat belt in the car seat setup and a four-point harness in the solid seat setup. Both the seat belt and harness were bolted to the simulation table.

(a) Empty seat

(b) Seat with sandbag

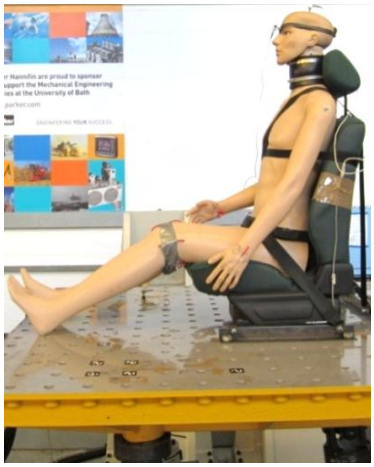

(c) Dummy measurement: car seat

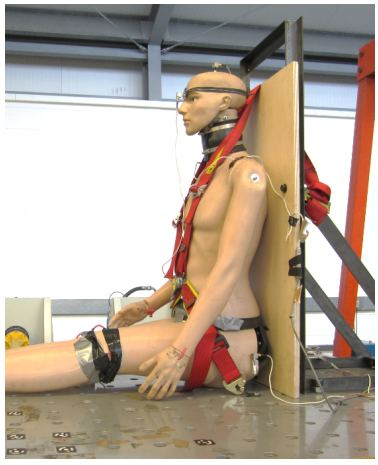

(d) Dummy measurement: solid seat

Figure 4.1: Experimental seat rig.

4.1.3 Multi-axis vibration simulation table

The multi-axis vibration simulation table (MAST) has 6 degrees-of-freedom, and can be controlled in Cartesian co-ordinates (X, Y, Z, Roll, Pitch, and Yaw). Control signals such as sine waves and random inputs can be specified, and any combination of linear or rotary motions can be commanded simultaneously. The actuator stroke is ±75 mm, with test frequencies up to 50 Hz, and acceleration up to 60 m/s^2.

4.1.4 Seat interface transducer pad

A seat interface transducer pad was used to mount the accelerometers on the seat conforming to ISO 10326-1:1992 Mechanical vibration - Laboratory method for evaluating vehicle seat vibration, as shown in Figure 4.1 (a). The flexible pad was a semi-rigid rubber sheet and was designed to conform to the contours of the seat under the weight of subjects. The pad had no adverse effect on the contact condition with the seat surface, and did not compress or bend under the action of normal vibration during measurements.

4.1.5 Accelerometers and data acquisition system

A total of six single-axis piezoresistive accelerometers (Entran, EGCS-D1CM-25) were used to measure the acceleration of the simulation table, test dummy and vehicle seat. The measurement locations and orientations are listed in Table 4.1. Due to the limited number of accelerometers, accelerometers No. 3 and 4 were interchanged between some measurement locations in order to gain both vertical and fore-and-aft axis signals. The accelerometer mounted on the head of the dummy in the vertical direction was reclined at 10.3° to the vertical and in the fore-aft direction was inclined at 19.8° to the horizontal. The signals from the accelerometers were sampled at 1000 Hz and were acquired by an xPC Target system using a NI PCI-6229 data acquisition board. Figure 4.2 provides an overview of the experimental measurement and data acquisition setup.

Table 4.1: Position of the accelerometers used in the measurements.

Accelerometer position	Orientation	
	Vertical	**Fore-and-aft**
Head	Yes (No.1)	Yes (No.2)
Shoulder	Yes (No.3 Interchanged)	
Pelvis	Yes (No.4 Interchanged)	
Seat pan	Yes (No.4 Interchanged)	-
Seat backrest	-	Yes (No.3 Interchanged)
Simulation table	Yes (No.5)	Yes (No.6)

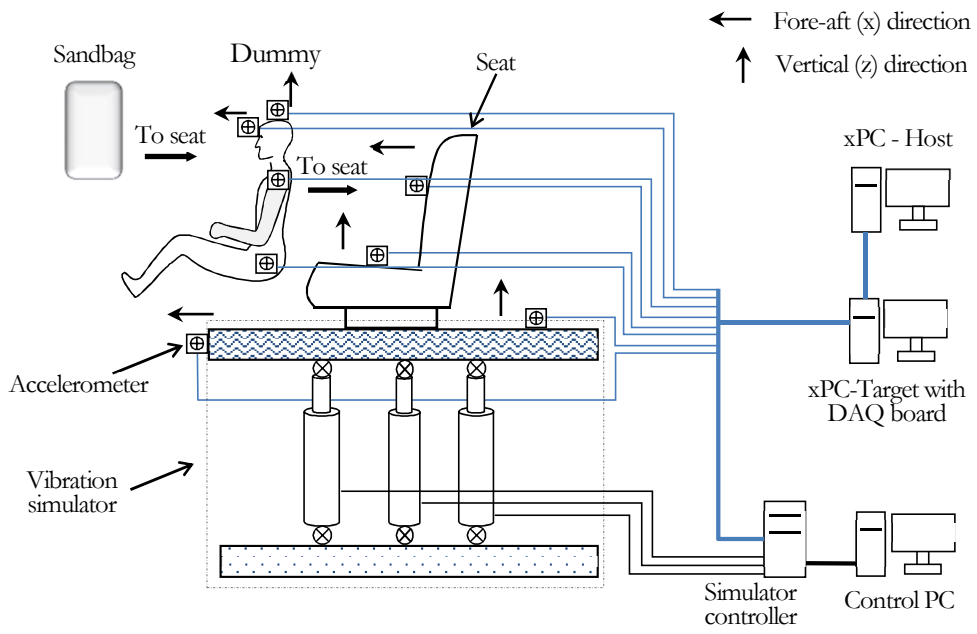

Figure 4.2: Experimental setup for vehicle seat and dummy vibration measurements.

4.2 Vibration measurement method

Four types of measurements were undertaken. These were an empty seat transmissibility measurement, a seat transmissibility measurement with a sandbag and a dummy transmissibility measurement on both a solid seat and a vehicle seat. The setups are shown in Figure 4.1. The recorded acceleration data of the corresponding location and orientation was used to calculate the vibration transmissibility, power spectral density (PSD) and ordinary coherence between the measurement points.

4.2.1 Excitation signal types

A number of excitation signal sequences were generated based on both vehicle vibration data, and the dynamic behaviour of the test dummy and seat. The amplitudes of the excitation signal ranged from 0.5mm to 10mm, and the frequencies up to 20 Hz. The frequency intervals were 0.25 Hz in the primary resonance range (typically 4-8 Hz), and 1 Hz outside of this range. The excitation signal sequences were grouped into three main types:

Excitation A – Sinusoidal excitation signal with constant displacement amplitude with a frequency range from 1 Hz to 20 Hz. Under this kind of excitation signal, the simulation table shakes in three different modes: x-axis shakes only, z-axis shakes only, and x & z-axis shake simultaneously. The measurement duration at each frequency was 40 seconds.

Excitation B – Sinusoidal excitation signal with constant frequency with a variable amplitude range from 1 mm to 10 mm (the amplitude at frequencies above 4 Hz was limited to 5mm due to the excessive acceleration level). The measurement duration of each different amplitude signal was 40 seconds.

Excitation C – Random excitation signal with frequency range 0-20 Hz for both the x-axis and z-axis, with peak amplitudes of 2.2 mm for the x-axis and 5.5 mm for the z-axis. The measurement duration for both axes was 120 seconds.

The excitation signal types and details are listed in Table 4.2.

Table 4.2: Excitation signal types and vibration simulator shaking modes.

Signal type	Amplitude(mm)	Frequency (Hz)	Axis	Peak acceleration (g)	Table shake mode
Excitation A	5.5	1-15	z	5	1. x-axis only 2. z-axis only 3. x, z axis simultaneously
	3.0	1-20	x, z	2	
	1.0	1-20	x, z		
	0.5	1-20	z		
Excitation B	1-10	2	x, z	0.16	1. x-axis only 2. z-axis only
	1-10	4	x, z	0.32	
	1-5	6	x, z	0.72	
	1-5	8	x, z	1.29	
	1-5	10	x, z	2.01	
	1-5	12	x, z	2.89	
	1-5	14	x, z	3.94	
Excitation C	2.2 (Peak value)	0-20	x	3.54	1. x, z axis simultaneously
	5.5 (Peak value)	0-20	z	8.85	

The following equation can be used to calculate the maximum acceleration of the above excitation signals:

$$Maximum\ acceleration = \frac{Amplitude}{1000} * (2\pi * Frequency)^2 * \frac{1}{9.81}\ \ (g) \qquad (4.1)$$

where the Amplitude (mm) and Frequency (Hz) are known, g (gravity of earth) uses approximate value of 9.81 m/s^2.

4.2.2 PSD and ordinary coherence analysis

PSD analysis

The power spectral density (PSD) describes how the power of a signal is distributed over the content frequencies, and it can be used to reveal the resonant frequencies of the test objects under random excitation. The PSD of a random signal $x(t)$ can be expressed as the average of the Fourier transform magnitude squared over a large time interval:

$$PSD_x(f) = \lim_{T\to\infty} E\left\{\frac{1}{2T}\left|\int_{-T}^{T} x(t)e^{-j2\pi ft}dt\right|^2\right\} \tag{4.2}$$

where E denotes the expected value, T is the time interval and f is the frequency.

Ordinary coherence analysis

Coherence functions are used to assess the validity of the frequency response function from the measured data and to analyse the linear relationship between the input and output signals. For a single-input and single-output (SISO) system, the ordinary coherency between the input signal $x(t)$ and the output signal $y(t)$ is defined as [88]:

$$\gamma_{xy}^2(f) = \frac{\left|G_{xy}(f)\right|^2}{G_{xx}(f)G_{yy}(f)} = \frac{\left|S_{xy}(f)\right|^2}{S_{xx}(f)S_{yy}(f)} \tag{4.3}$$

where $G_{xx}(f)$ and $G_{yy}(f)$ are the one-sided spectral density functions of $x(t)$ and $y(t)$, respectively. $G_{xy}(f)$ is the one-sided cross-spectral density function between $x(t)$ and $y(t)$. $S_{xx}(f)$ and $S_{yy}(f)$ are the power spectral density functions of $x(t)$ and $y(t)$, respectively. $S_{xy}(f)$ is the cross-spectral density function between $x(t)$ and $y(t)$. Because $\left|S_{xy}(f)\right|^2 \leq S_{xx}(f)S_{yy}(f)$, it follows that $0 \leq \gamma_{xy}^2(f) \leq 1$ for $0 \leq f \leq \infty$.

If the SISO system is a linear system, then $S_{yy}(f) = |H(f)|^2 S_{xx}(f)$ and $S_{xy}(f) = H(f)S_{xx}(f)$, where $H(f)$ is the system frequency response function. So the coherence function is:

$$\gamma_{xy}^2(f) = \frac{|H(f)|^2 S_{xx}{}^2(f)}{S_{xx}(f)|H(f)|^2 S_{xx}(f)} = 1 \tag{4.4}$$

This implies that the input signal $x(t)$ and output signal and $y(t)$ are linearly related at all frequencies. If the system is nonlinear, or has multiple-input, or experiences noise in the measurements of either or both $x(t)$ and $y(t)$ then the coherence function is less than unity.

4.3 Vehicle seat vibration transmissibility results

The results of the vehicle seat vibration transmissibility tests are grouped into three types based on the measurement setups. These are an empty seat transmissibility, a seat transmissibility with a sandbag and a seat transmissibility with a dummy. In each case, the overall transmissibility from the MAST to the seat pan (vertical) and backrest (fore-and-aft) under excitation A, the vibration magnitude related non-linearity under excitation B, and the PSD and ordinary coherence under excitation C were calculated using the recorded acceleration data. For the cases of x & z-axis shaking simultaneously, the corresponding transmissibilities were calculated using the measured input and output signals in the same axis.

4.3.1 Empty seat transmissibility

Excitation A: Overall transmissibility

Figure 4.3 shows the overall transmissibility from the MAST to the seat pan and backrest under excitation A. The MAST to the seat pan transmissibility in the vertical direction exhibits no obvious peak in the 1-15 Hz frequency range for either shake modes, and it tends to rise as the frequency increases. The MAST to backrest

transmissibility in the fore-and-aft direction exhibits a distinctive resonant frequency near 9 Hz for both shake modes. The peak magnitude is over 7 for the Z-axis shake mode.

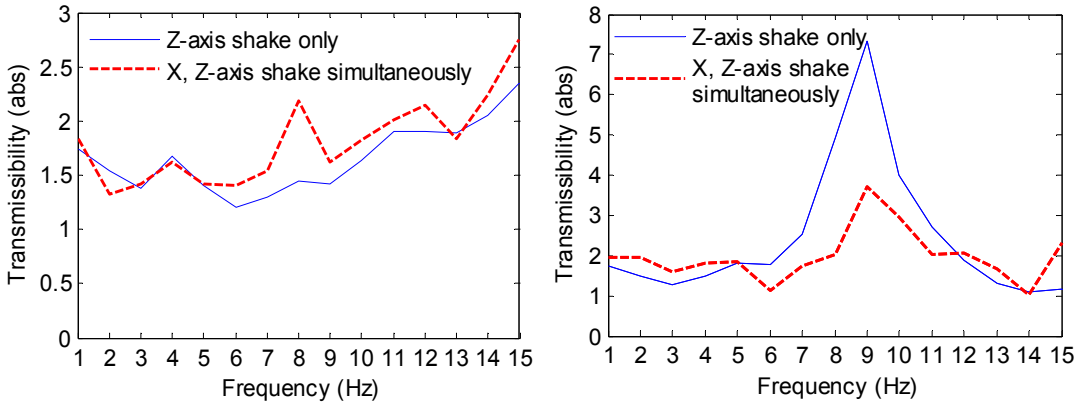

(a) MAST to seat pan (vertical). (b) MAST to backrest (fore-and-aft).

Figure 4.3: Overall transmissibility of the empty seat.

Excitation B: Vibration magnitude related non-linearity

Figure 4.4 shows the effect of the vibration magnitude related non-linearity of the empty seat. Both the MAST to seat pan and MAST to backrest transmissibilities appear to be fairly independent of amplitude at all the measured frequencies.

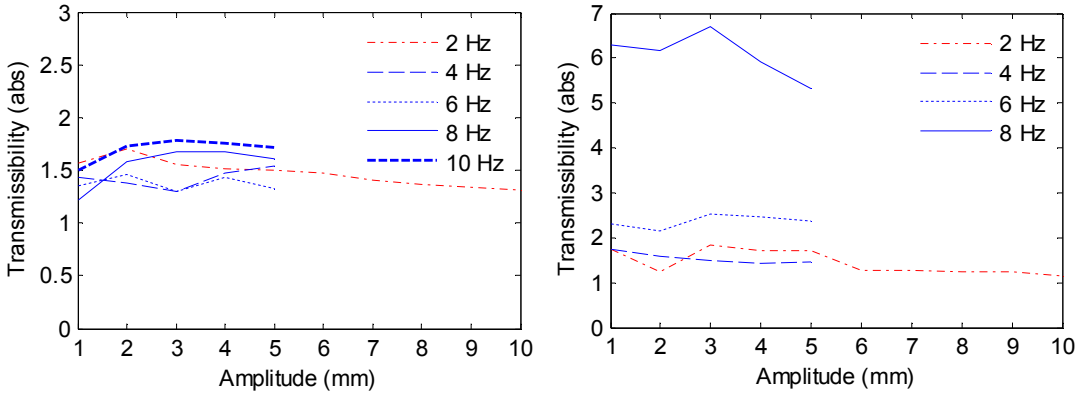

(a) MAST to seat pan (vertical). (b) MAST to backrest (fore-and-aft).

Figure 4.4: Vibration magnitude related non-linearity of the empty seat.

Excitation C: PSD and coherence analysis

Figure 4.5 shows the PSD and coherence plots of the empty seat. The PSD plots of the MAST and seat pan acceleration signal in the vertical direction show a similar energy distribution without obvious peaks. However, there is a peak near 9 Hz in the backrest signal PSD. An over strong coherence of 0.8-1.0 is exhibited between the MAST and seat pan signal, and the coherence between the MAST and backrest is fluctuating. Both the PSD and coherence analysis support the trends observed in Figure 4.3.

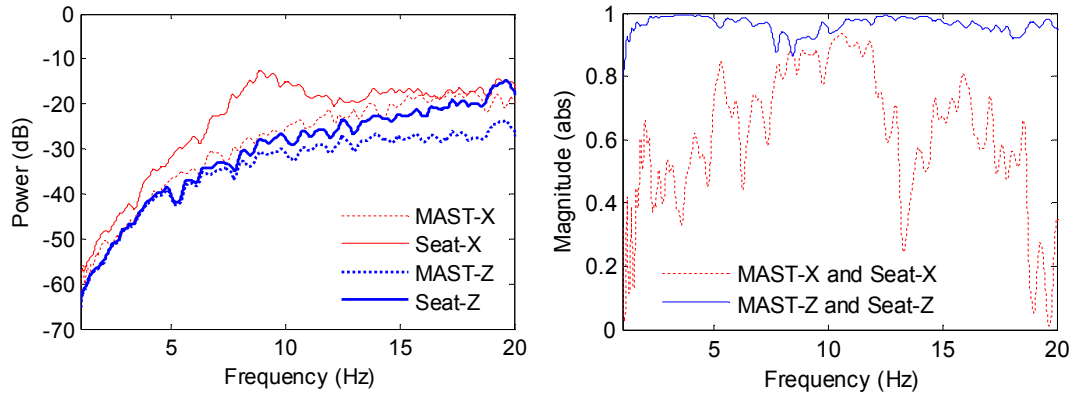

(a) PSD plots. (b) Coherence plots.

Figure 4.5: PSD and coherence plots of the empty seat.

4.3.2 Seat transmissibility with a sandbag

Excitation A: Overall transmissibility

The overall transmissibility of the seat with a sandbag under excitation A is shown in Figure 4.6. A dominant resonant frequency between 4 and 6 Hz can be clearly observed in the MAST to the seat pan transmissibility in the vertical direction, and the associated peak magnitudes are over 1.5. It can also be observed that the transmissibility magnitudes tend to drop below 0.5 beyond frequencies of 6 Hz. The MAST to the backrest transmissibility in the fore-and-aft direction exhibits a resonant frequency near 3 Hz for both shake modes.

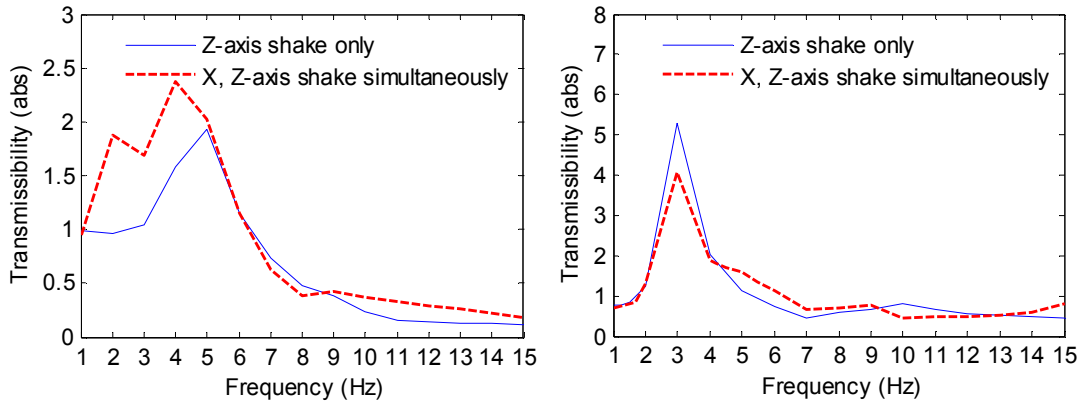

(a) MAST to seat pan (vertical). (b) MAST to backrest (fore-and-aft).

Figure 4.6: Overall transmissibility of the seat with a sandbag.

Excitation B: Vibration magnitude related non-linearity

Figure 4.7 shows the effect of the vibration magnitude related non-linearity of the seat with a sandbag. The MAST to seat pan transmissibility at frequencies 4, 6 and 8 Hz (close to the resonant frequency observed in Figure 4.6) changes significantly as amplitude increases. This may indicate a vibration magnitude related non-linearity in the seat and seated object system. A similar trend can also be found in the MAST to backrest transmissibility in the fore-and-aft direction.

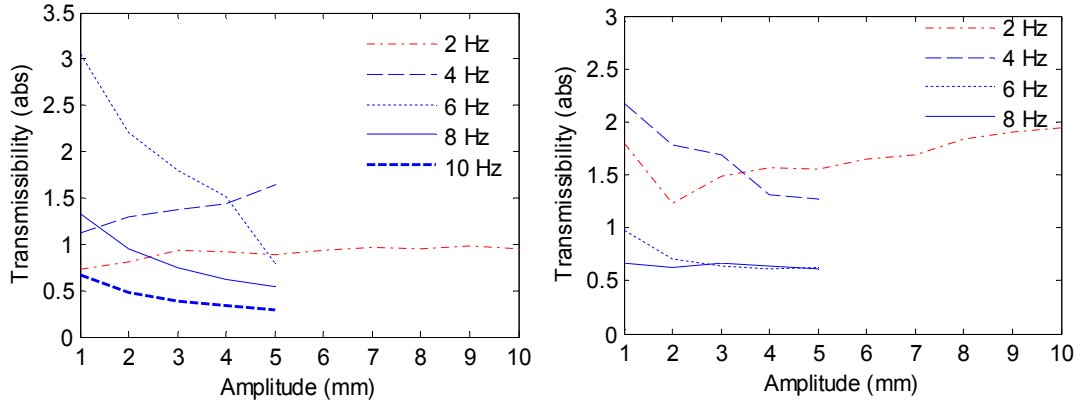

(a) MAST to seat pan (vertical). (b) MAST to backrest (fore-and-aft).

Figure 4.7: Vibration magnitude related non-linearity of the seat with a sandbag.

Excitation C: PSD and coherence analysis

Figure 4.8 shows the PSD and coherence plots of the seat with a sandbag. Two peaks at 6 Hz and 3 Hz can be identified in the seat pan signal (vertical) and the backrest signal (fore-and-aft), respectively. This is consistent with the observation in Figure 4.6. The coherence of the MAST and the seat pan signal in the vertical direction, as shown in Figure 4.8 (b), drops significantly above 10 Hz. The coherence between the MAST and backrest tends to rise as the frequency increases, indicating that the backrest is more linear at higher frequency.

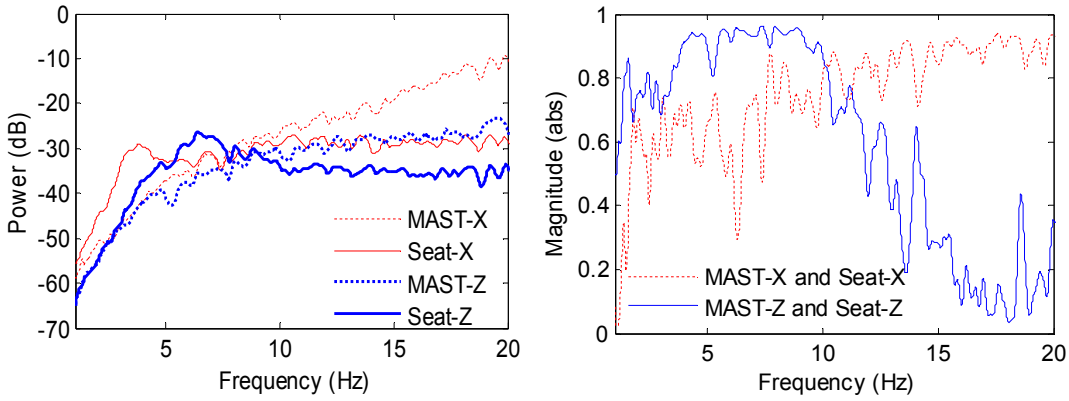

(a) PSD plots. (b) Coherence plots.

Figure 4.8: PSD and coherence plots of the seat with a sandbag.

4.3.3 Seat transmissibility with a dummy

Excitation A: Overall transmissibility

The overall transmissibility of the seat with a dummy under excitation A is shown in Figure 4.9. It is observed that there is a dominant resonance at a frequency of approximately 5 Hz in the MAST to the seat pan transmissibility in the vertical direction, with peak magnitude over 1.5. Two close peaks near 4 Hz can be identified in the MAST to the backrest transmissibility in the fore-and-aft direction. The transmissibilities of both shake modes show good consistency, except that a new peak near 3 Hz was introduced in the MAST to the seat pan transmissibility under the X, Z-axis shake mode.

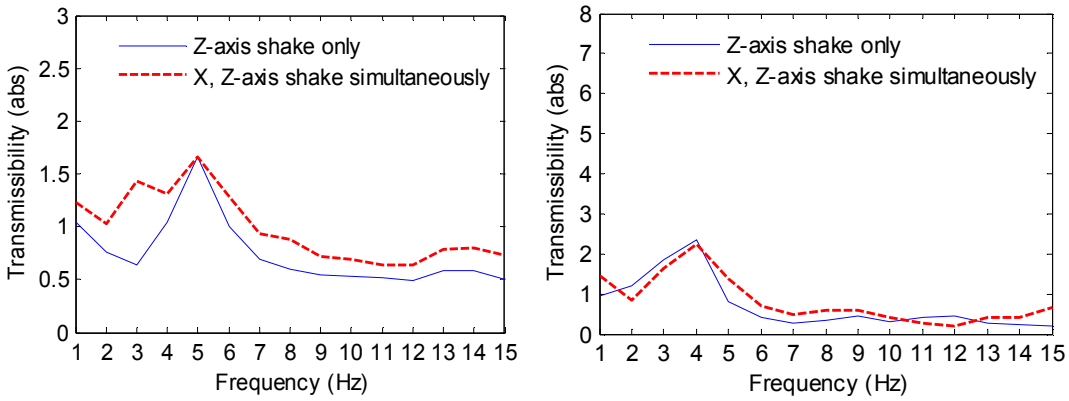

(a) MAST to seat pan (vertical). (b) MAST to backrest (fore-and-aft).

Figure 4.9: Overall transmissibility of the seat with a dummy.

Excitation B: Vibration magnitude related non-linearity

The effect of the vibration magnitude related non-linearity of the seat with a dummy is shown in Figure 4.10. The MAST to seat pan transmissibility at frequencies 4 and 6 Hz (close to the resonant frequency 5 Hz observed in Figure 4.9 (a)) shows a larger change than at other frequencies. Similarly, the MAST to backrest transmissibility at a frequency of 4 Hz (the resonant frequency observed in Figure 4.9 (b)) changes significantly while the transmissibility at other frequencies remains quite constant.

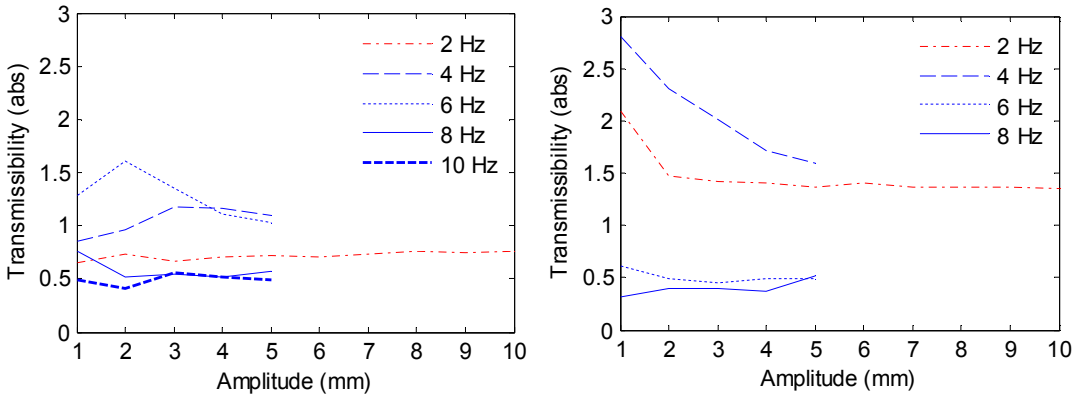

(a) MAST to seat pan (vertical). (b) MAST to backrest (fore-and-aft).

Figure 4.10: Vibration magnitude related non-linearity of the seat with a dummy.

Excitation C: PSD and coherence analysis

The PSD and coherence plots of the seat with a dummy are shown Figure 4.11. In the PSD plots, two peaks near 6 Hz and 4 Hz can be observed in the seat pan signal (vertical) and the backrest signal (fore-and-aft), respectively. The coherence of the MAST and the seat pan signal in the vertical direction tends to decrease at frequencies above 7 Hz. The coherence between the MAST and backrest signal remains significantly low in the 5-15 Hz frequency range but high at both ends.

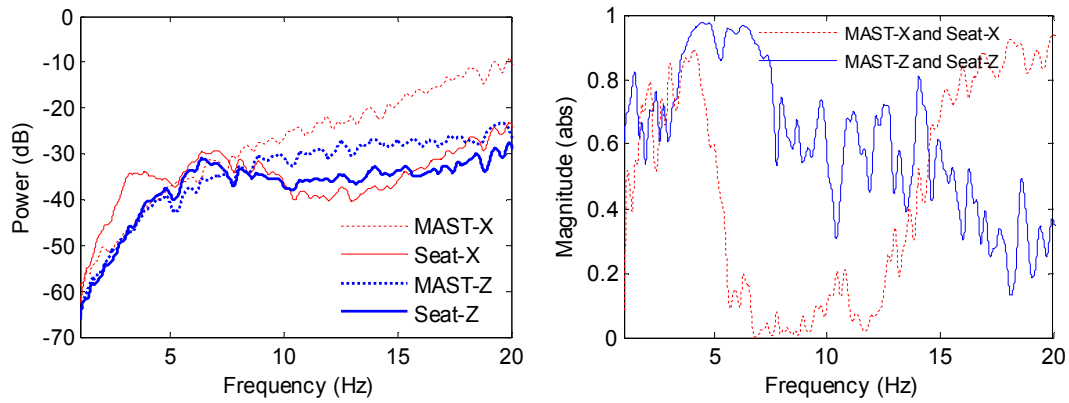

(a) PSD plots. (b) Coherence plots.

Figure 4.11: PSD and coherence plots of the seat with a dummy.

4.4 Dummy vibration transmissibility results

The dynamic response of the test dummy was characterised by measuring the vibration transmissibility under two conditions; the solid seat and the vehicle seat.

The solid seat tests investigate the response of the dummy itself without the vehicle seat interference, while the vehicle seat tests provide an insight into the coupling effects between the dummy and seat.

4.4.1 Solid seat tests

Excitation A: Overall transmissibility

Vertical

The overall transmissibility in the vertical direction from the MAST to the dummy head, shoulder and pelvis was calculated and is shown in Figure 4.12.

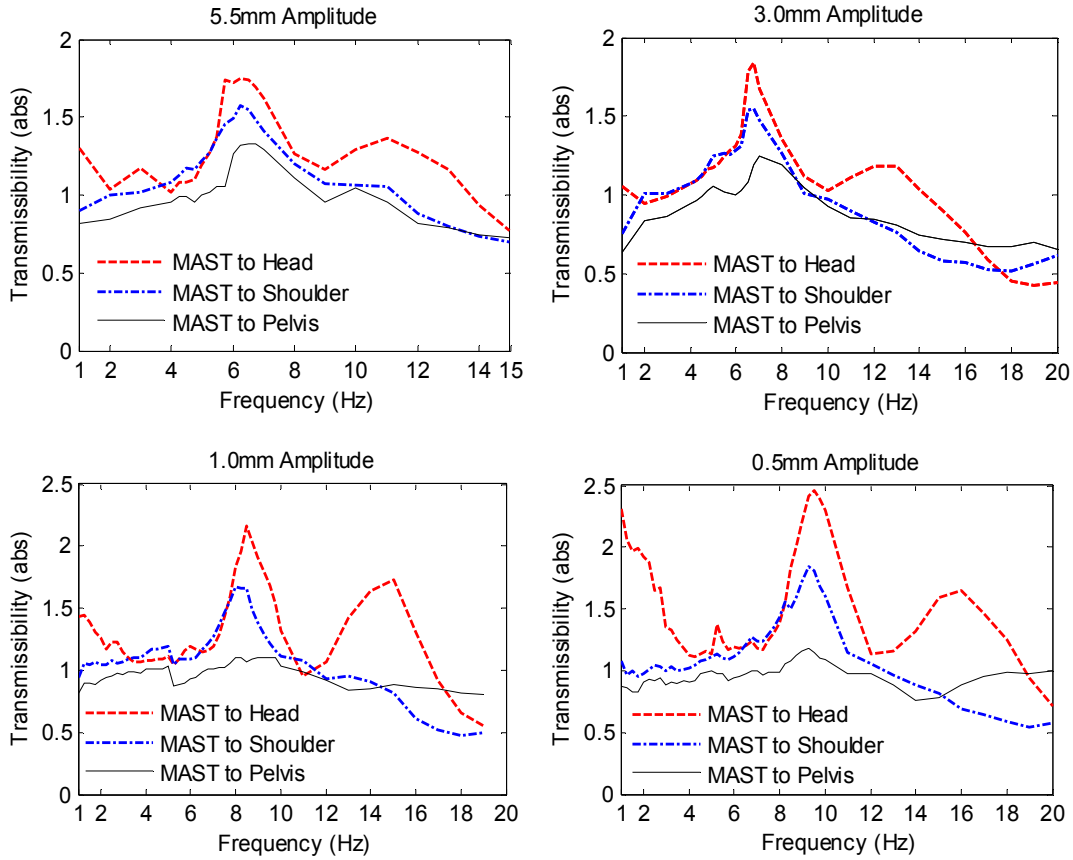

Figure 4.12: Overall transmissibility of the dummy in the vertical direction.

It can be observed that a dominant resonant frequency occurs in the range of 6-8 Hz, with the peak transmissibility increasing from 1.1 at the pelvis, to above 1.7 at the head for the 5.5 and 3.0 mm excitation amplitudes. This dominant whole body resonance is similar to some previous measurements on seated human subjects [7-9]. It can also be observed that the dominant resonance tends to shift to the range of 8-10 Hz at lower excitation amplitudes (1.0 and 0.5 mm).

Due to very low acceleration levels at the 1.0 and 0.5 mm amplitude, the acceleration was of similar magnitude to noise. Therefore low frequency measurements below 4Hz at low excitation amplitude may be affected by signal noise.

Fore-and-aft

Figure 4.13 shows the overall transmissibility of the dummy in the fore-and-aft direction. The MAST to head and shoulder transmissibility exhibit a dominant resonance in the range of 4-8 Hz at both 3.0 mm and 1.0 mm excitation amplitudes. The MAST to head peak transmissibility is over 3 at 3.0 mm and over 5 at 1.0 mm amplitude. A dominant fore-and-aft 'rocking' motion associated with a rotation about the pelvis was observed in the response of the dummy. Both the head and shoulder transmissibilities drop rapidly above the resonant frequency range. However, the MAST to pelvis transmissibility remains constant around one and shows no obvious peak.

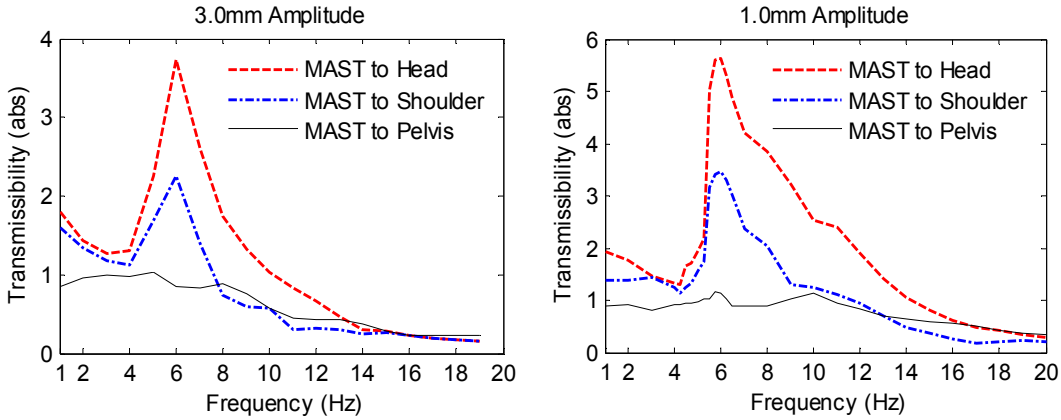

Figure 4.13: Overall transmissibility of the dummy in the fore-and-aft direction.

Excitation B: Vibration magnitude related non-linearity

Vertical

Figure 4.14 shows the vibration magnitude related non-linearity of the dummy on the solid seat in the vertical direction. The MAST to head and shoulder transmissibilities at a constant frequency over a range of excitation amplitudes were calculated. It can be observed that both the head and shoulder transmissibility change more significantly at frequencies of 6 Hz and 8 Hz. These frequencies are close to the resonance frequency

identified in Figure 4.12. This may indicate that the non-linearity associated with the vibration magnitude has a larger effect at frequencies near the resonance.

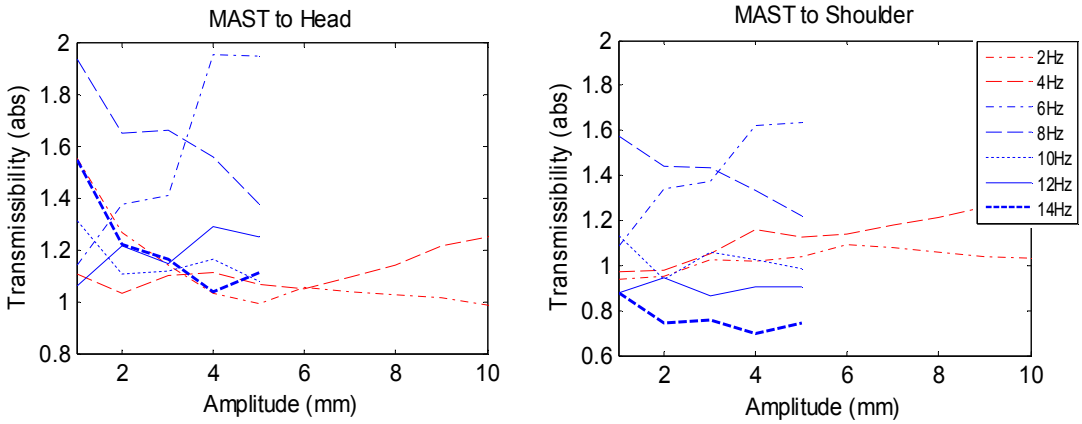

Figure 4.14: Vibration magnitude related non-linearity of the dummy on solid seat (vertical).

Fore-and-aft

Figure 4.15 shows the vibration magnitude related non-linearity of the dummy on the solid seat in the fore-and-aft direction. It can be seen that both the head and shoulder transmissibility shows a large change at 4 Hz when amplitude increases from 1 mm to 3 mm and remain stable at amplitudes above 3 mm. The head transmissibility tends to decrease with amplitude, increasing at frequencies above 4 Hz. However, the shoulder response appears to be more linear than the head response at frequencies above 4 Hz.

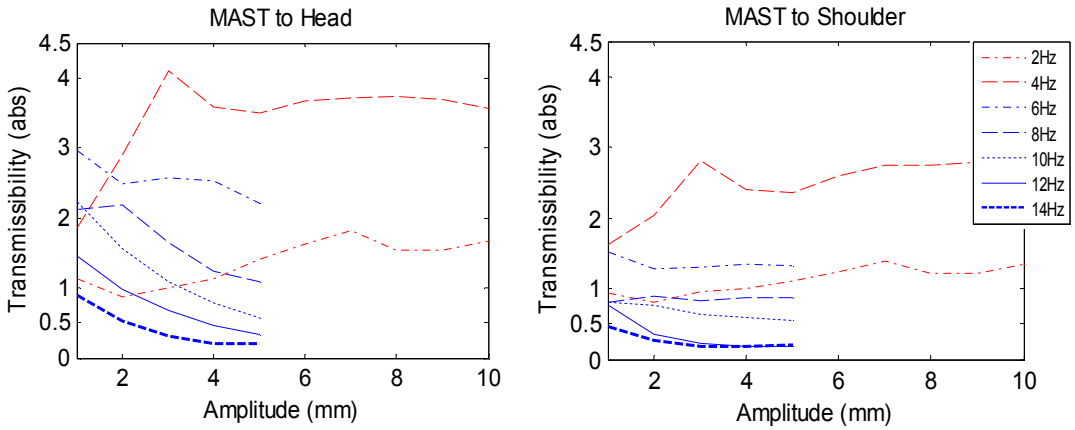

Figure 4.15 Vibration magnitude related non-linearity of the dummy on solid seat (fore-and-aft).

Excitation C: PSD and coherence analysis

Vertical

The PSD and coherence plots of the dummy on the solid seat in the vertical direction are shown in Figure 4.16 and Figure 4.17, respectively. In the PSD plots, a peak in the range of 8-10 Hz can be identified in both the head and shoulder signal. These peaks in the PSD are associated with the corresponding resonance modes which are observed in the overall transmissibility results under excitation A. The coherence magnitudes of the MAST and head, MAST and shoulder, MAST and pelvis, and head and shoulder remain constant, near one, at frequencies above 4 Hz. This may indicate an overall linear behaviour. However, both the MAST and head, MAST and shoulder coherence drop slightly at frequency near 10 Hz.

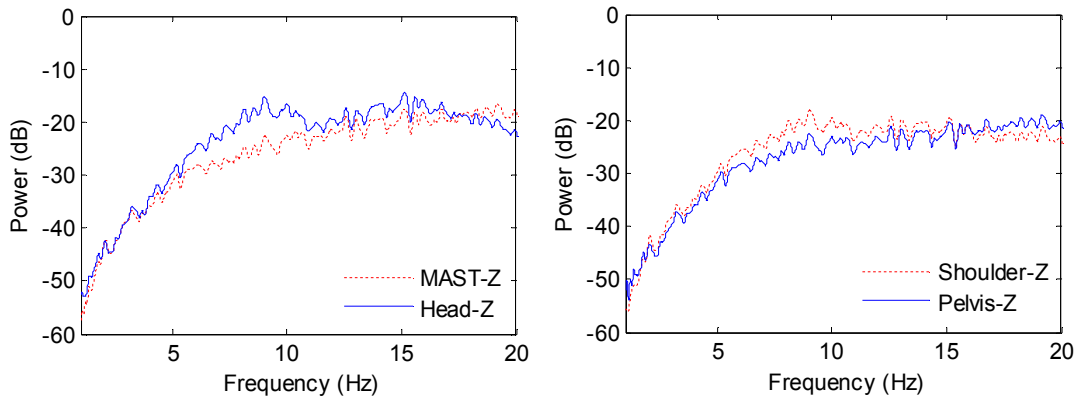

Figure 4.16: PSD plots of the dummy on solid seat in the vertical direction.

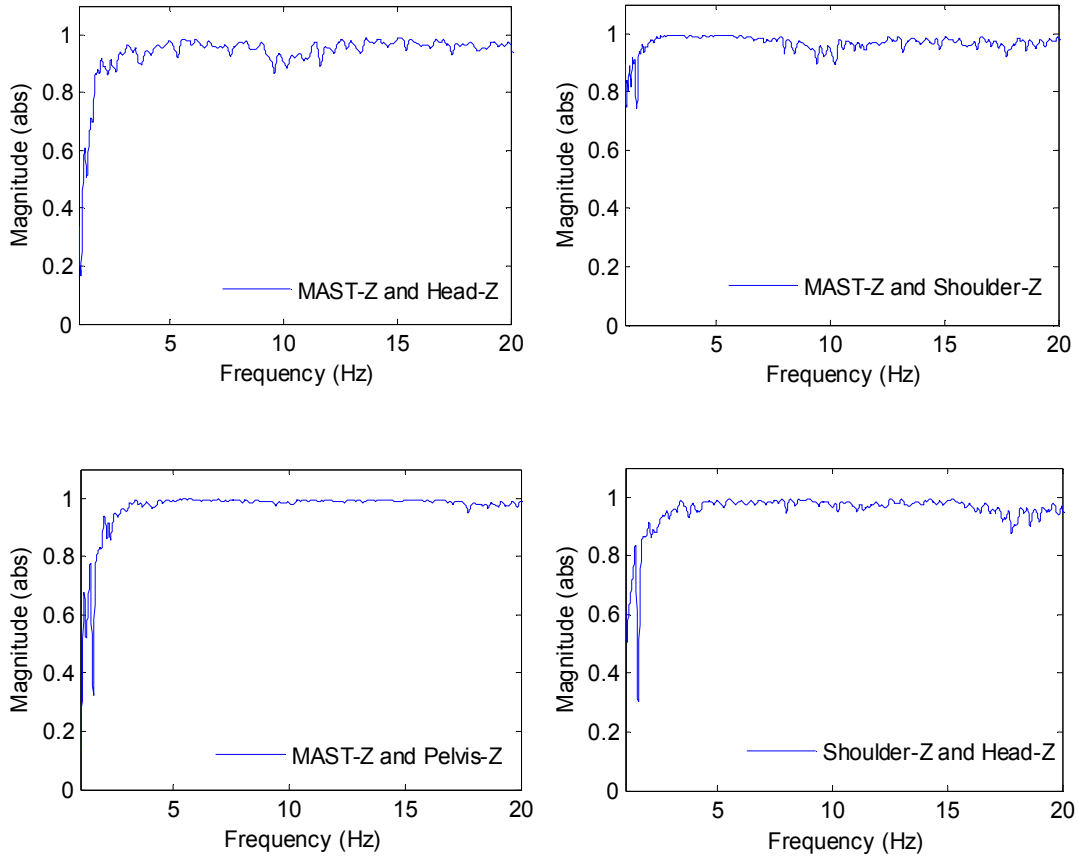

Figure 4.17: Coherence plots of the dummy on solid seat in the vertical direction.

Fore-and-aft

The PSD and coherence plots of the dummy on the solid seat in the fore-and-aft direction are shown in Figure 4.18 and Figure 4.19, respectively. As shown in the PSD plots, an obvious peak in the range of 4-6 Hz can be observed in both the head and shoulder signal. Similar to the vertical results, these peaks associated with the corresponding resonance modes are consistent with the overall transmissibility results in Figure 4.13. The coherence of the MAST and pelvis remains constant and high while the coherence of the MAST and head, MAST and shoulder, head and shoulder show noticeable fluctuation at frequencies above 5 Hz.

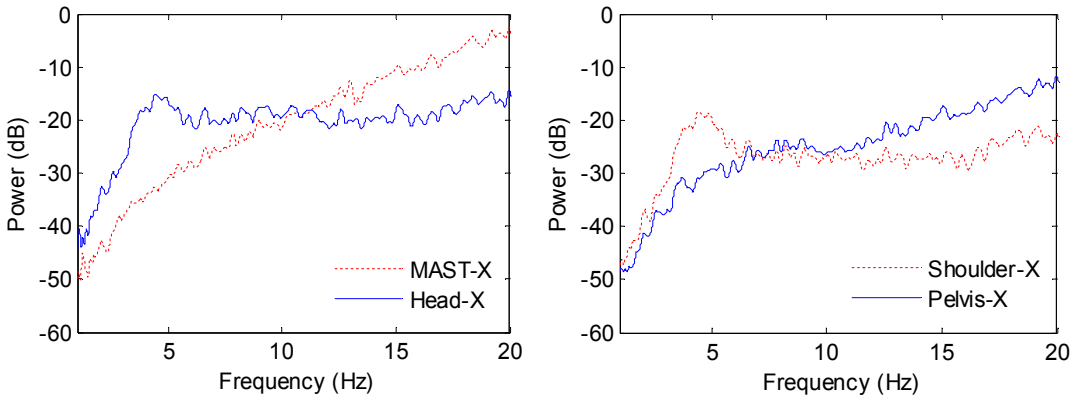

Figure 4.18: PSD plots of the dummy on solid seat in the fore-and-aft direction.

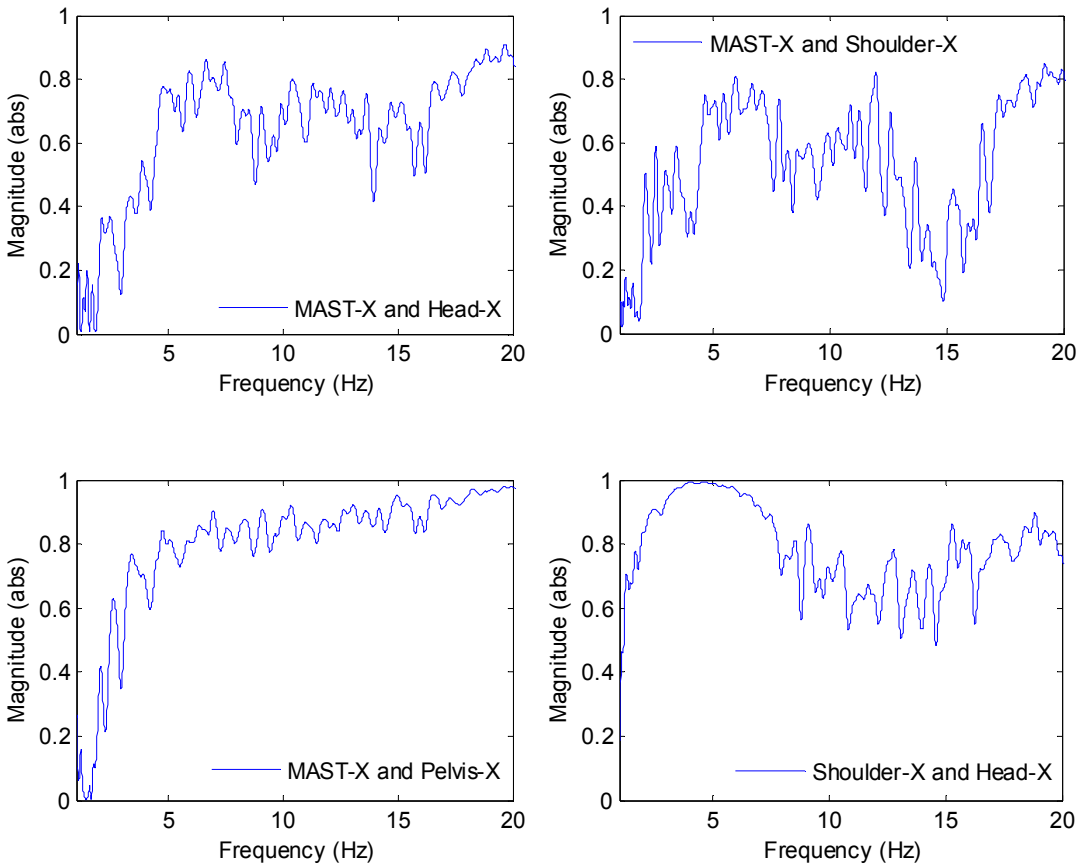

Figure 4.19: Coherence plots of the dummy on solid seat in the fore-and-aft direction.

4.4.2 Vehicle seat tests

Excitation A: Overall transmissibility

Vertical

Figure 4.20 shows the overall transmissibility of the dummy on the vehicle seat in the vertical direction. A dominant resonant frequency in the range of 4-8 Hz can be found. The peak transmissibility increases from around 2 at the pelvis, to above 3 at the head for both the excitation amplitudes. Again, this dominant whole body resonance is similar to some previous measurements on seated human subjects [7-9].

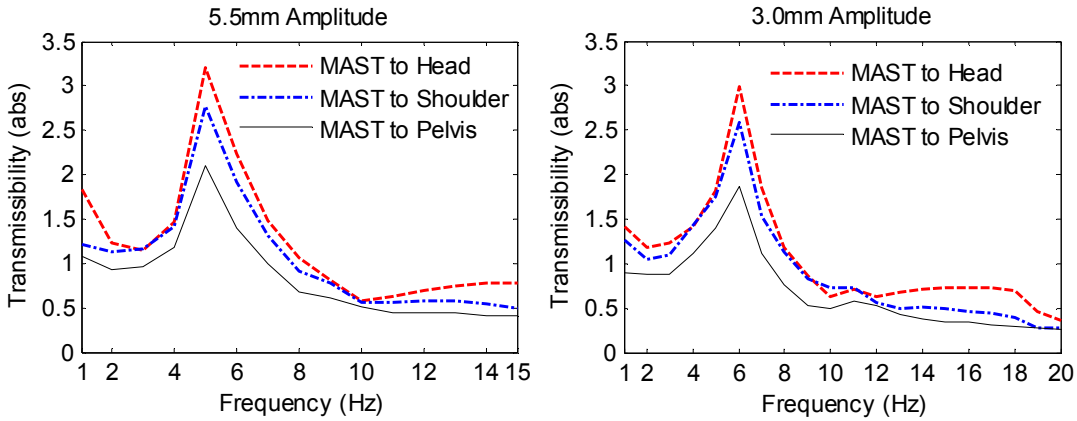

Figure 4.20: Overall transmissibility of the dummy on the vehicle seat (vertical).

Fore-and-aft

Figure 4.21 shows the overall transmissibility of the dummy on the vehicle seat in the fore-and-aft direction. It can be observed that a dominant resonant frequency occurs in the range of 3-6 Hz, with a peak transmissibility above 3 and 5 at the shoulder and head respectively. A second resonance in the range of 8-10 Hz can also be found at the head which was caused by a 'rocking' rotation about the neck.

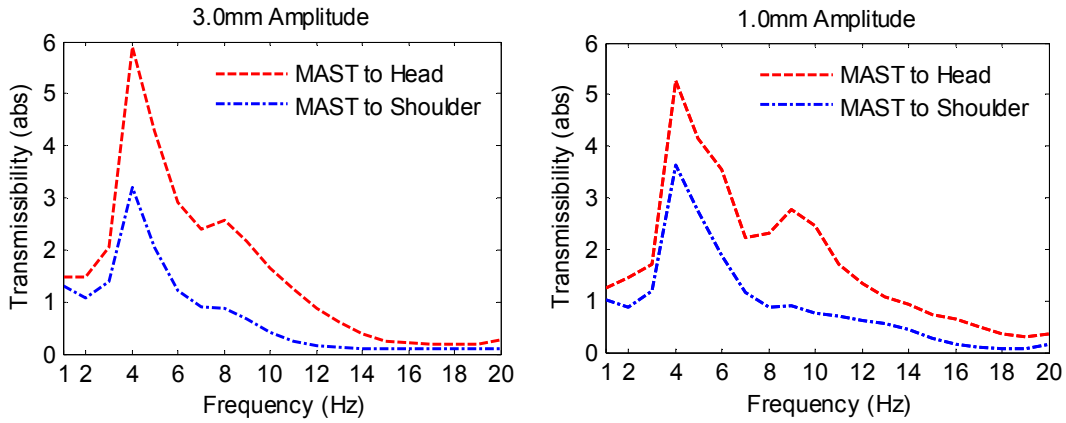

Figure 4.21: Overall transmissibility of the dummy on vehicle seat (fore-and-aft).

Excitation B: Vibration magnitude related non-linearity

Vertical

Figure 4.22 shows the vibration magnitude related non-linearity of the dummy on the vehicle seat in the vertical direction. Similar to the observation on the solid seat test, both the head and shoulder transmissibility change more significantly at frequencies above 6 Hz (close to the resonance frequency identified in Figure 4.20) than at other frequencies. Both the head and shoulder transmissibility remains relatively constant at higher frequencies (10, 12 and 14 Hz).

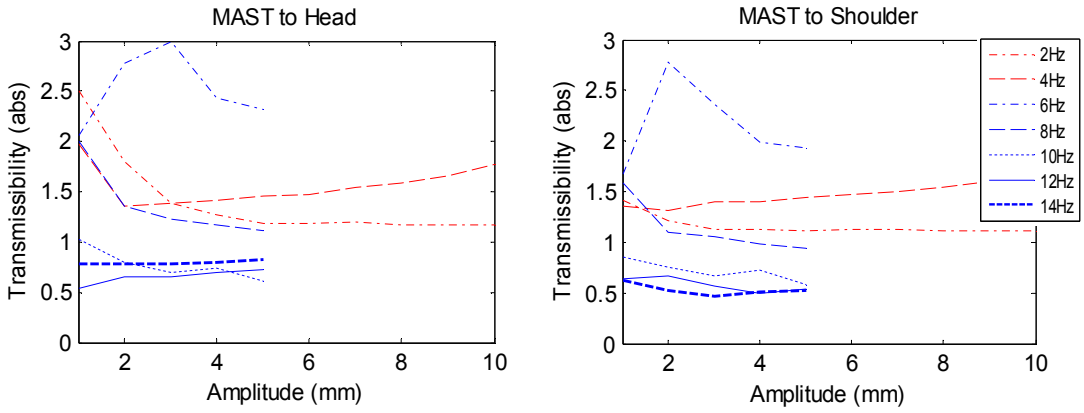

Figure 4.22: Vibration magnitude related non-linearity of the dummy on vehicle seat (vertical).

Fore-and-aft

Figure 4.23 shows the vibration magnitude related non-linearity of the dummy on vehicle seat in the fore-and-aft direction. The transmissibility at both the head and shoulder show much bigger change at a frequency of 4 Hz, which is close to the dominant resonant frequency identified in Figure 4.21. The head transmissibility also shows a relatively larger change at frequencies close to the second resonance. This, again, supports the general trend observed in the tests.

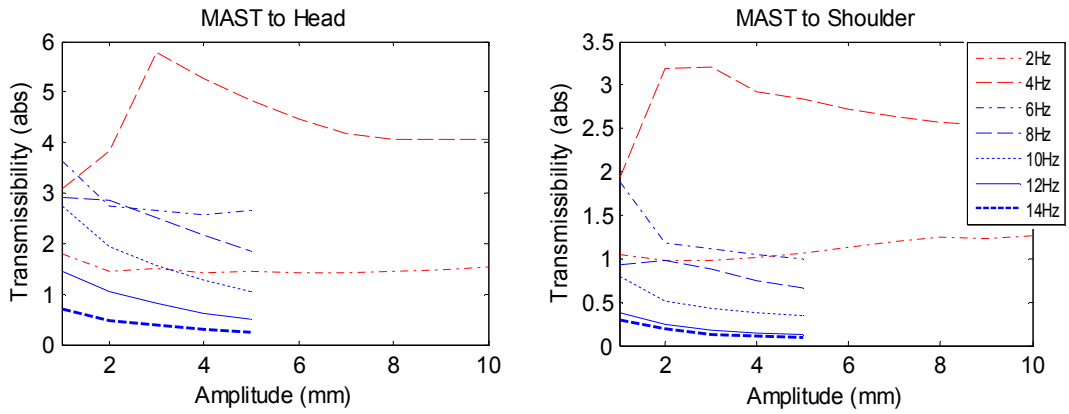

Figure 4.23: Vibration magnitude related non-linearity of the dummy on vehicle seat.

Excitation C: PSD and coherence analysis

Vertical

Figure 4.24 and 4.25 show the PSD and coherence plots of the dummy on the vehicle seat in the vertical direction, respectively. As shown in the PSD plots, an obvious peak in the range of 5-8 Hz can be observed in both the head and shoulder signal. These PSD peaks are associated with the corresponding resonance modes and the range is consistent with the observation in the overall transmissibility results presented in Figure 4.20. The overall coherence magnitudes of the MAST and head and the MAST and shoulder remain at high level, however, some small drops at frequencies near 8 and 12 Hz can be found.

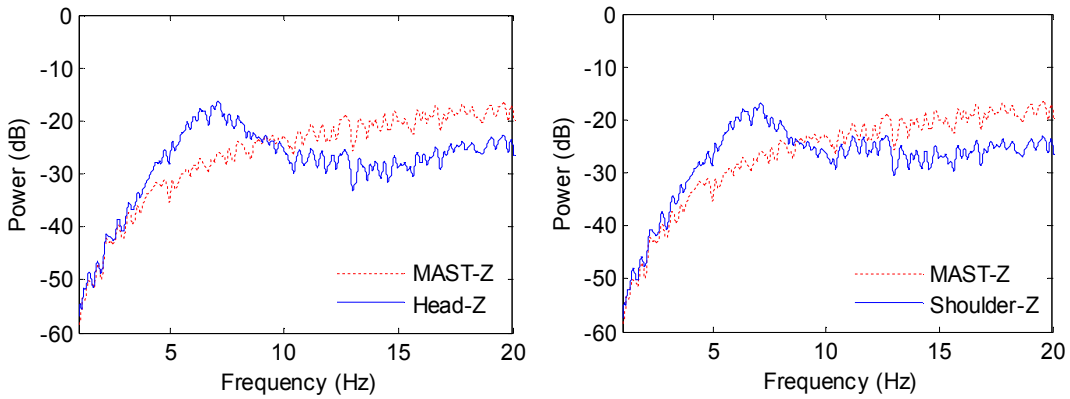

Figure 4.24: PSD plots of the dummy on vehicle seat in the vertical direction.

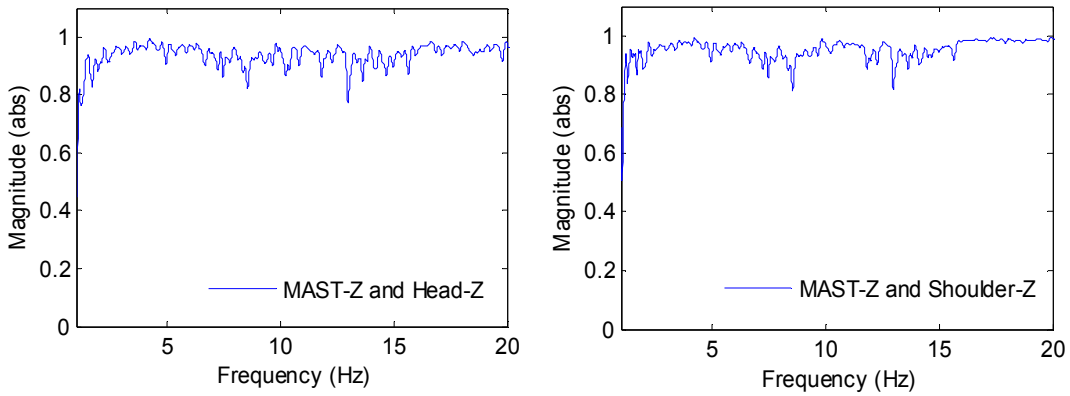

Figure 4.25: Coherence plots of the dummy on vehicle seat in the vertical direction.

Fore-and-aft

Figure 4.26 and 4.27 show the PSD and coherence plots of the dummy on the vehicle seat in the fore-and-aft direction, respectively. In the PSD plots, a peak near 4 Hz can be identified in both the head and shoulder signal, and there is a second peak in the head signal which occurs near 10 Hz. Again, these observations are generally consistent with the overall transmissibility results in Figure 4.21. The coherences between the MAST and head and the MAST and shoulder remain above 0.8 at frequencies above 4 Hz.

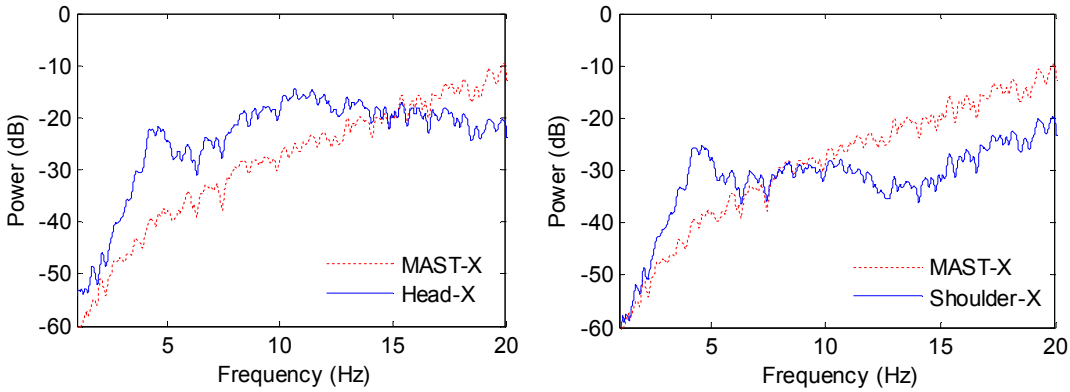

Figure 4.26: PSD plots of the dummy on vehicle seat in the fore-and-aft direction.

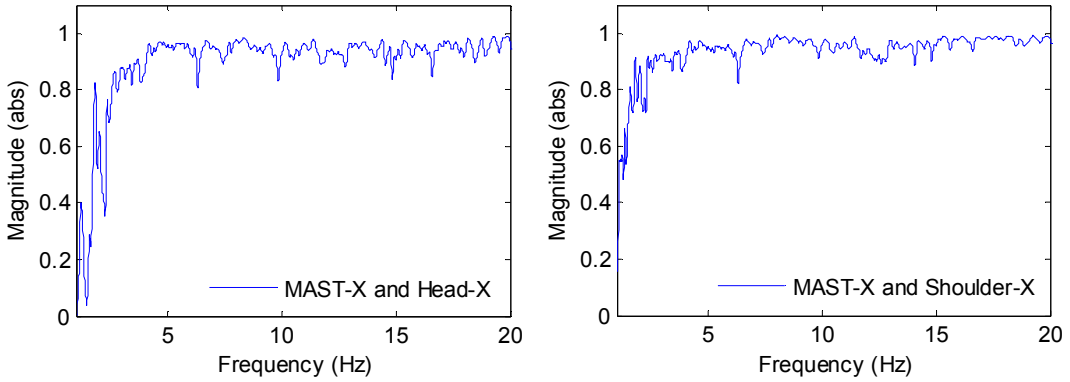

Figure 4.27: Coherence plots of the dummy on vehicle seat in the fore-and-aft direction.

4.5 Experimental measurements discussions

The vehicle seat vibration measurement results reveal several characteristics of the seat dynamic behaviour. For an empty seat, no obvious resonance is identified in the 1-15 Hz frequency range in the vertical direction, but there is a fore-and-aft mode near 9 Hz at the backrest. The effect of the vibration magnitude related non-linearity of the empty seat appears to be insignificant. For the seat transmissibility with a sandbag and a dummy, a dominant resonant frequency between 4 and 6 Hz can be clearly observed in the vertical direction. In addition, a resonance between 3 and 4 Hz can be found on the backrest in the fore-and-aft direction. These resonances are supported by the PSD analysis. Both the vertical and fore-and-aft transmissibilities at frequencies close to the resonant frequency show more significant changes than at other frequencies.. This may indicate that the vibration magnitude has a larger effect on the seat linearity near the

resonant frequency. It can also be observed that the seat transmissibility magnitude was up to several times higher at resonance, however it reduced significantly above 10Hz. This highlights the limits of the standard vehicle seat vibration isolation performance.

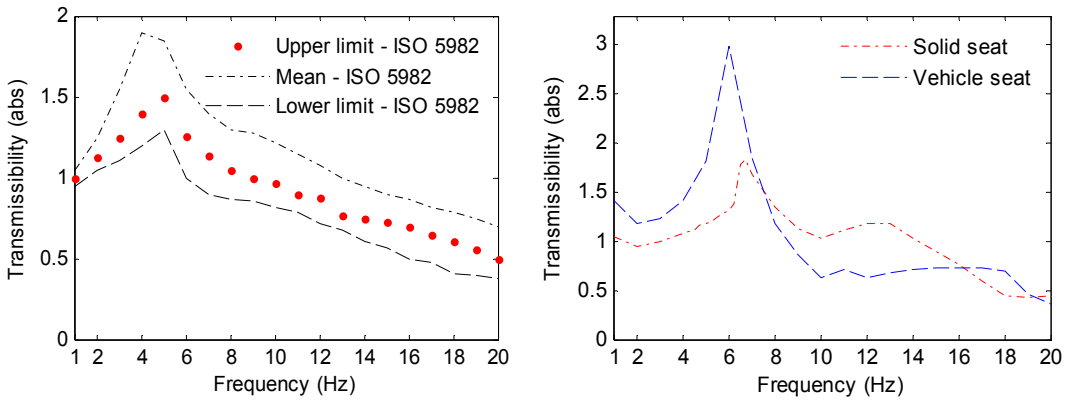

(a) STHT defined in ISO 5982 [8] (b) STHT of the dummy (3mm excitation).

Figure 4.28: Comparison of whole body resonances in the vertical direction.

Based on the analysis of the dummy vibration transmissibility results, a number of characteristics of the dummy dynamic response were identified. There is a distinctive vertical whole body mode in the 6-10 Hz frequency range on the solid seat, and a vertical whole body mode in the 4-8Hz frequency range on the vehicle seat. These resonances are broadly consistent with seated human body response as shown in the comparison in Figure 4.28. A fore-and-aft resonance in the range of 4-8 Hz and 3-6 Hz was found on the solid seat and the vehicle seat, respectively. In the fore-and-aft tests, a dominant rotational 'rocking' motion about the pelvis was observed in the response of the dummy, and a head resonance in the range of 8-10 Hz caused by a rotational 'rocking' motion about the neck was found. The head 'rocking' behaviour has not been observed on seated humans and is a characteristic of the dummy only. The vibration magnitude related non-linearity is significant at frequencies near the resonance in both the vertical and fore-and-aft responses. The coherence magnitudes in the vertical direction are generally high on both the solid and vehicle seat. However, some fluctuations indicated the frequency dependent non-linear behaviour of the dummy.

4.6 Conclusions

In this chapter, experimental measurements of the transmissibility of a test dummy and a vehicle seat were conducted in the laboratory. The overall transmissibility, vibration magnitude related non-linearity, the PSD and ordinary coherence were calculated using the recorded acceleration data. Several characteristics of the seat dynamic behaviour were identified, and the results highlighted the limited vibration isolation performance of the standard vehicle seats in the low frequency range. The dynamic response of the test dummy was characterised and the principal whole body modes were found to be broadly consistent with a seated human response. These findings enable the dummy to be used as a seated human body substitute in the active seat vibration cancellation tests in order to ensure an improved consistency in behaviour and avoid safety and ethical issues.

Chapter 5

Active Seat Structure and Dynamics

This chapter presents the details of the active seat structure and dynamics. The active seat was designed and built on the basis of the excitation frequency range (1-25 Hz) and an input displacement range of 0-30 mm. The constituent and mechanical structure of the active seat is described and illustrated by three-dimensional line drawings and photos. The characteristics of the active seat dynamics were identified via experimental tests.

5.1 Active seat mechanical structure

5.1.1 Overall structure

The mechanical model of the active seat is shown in Figure 5.1. The seat includes a passive suspension and an active actuation system. The passive suspension, which is composed of a spring and damper, supports the main static load of the seat pan and occupant. The active actuation system is composed of two electromagnetic linear actuators which are installed parallel at the front and the rear of the seat pan to provide active control authority. The moveable seat pan is supported at the middle of both sides by a two-bar lever mechanism that ensures parallel vertical motion. At the rear of the seat pan, two linear sliders are used to allow the seat pan to move vertically upwards. The linear rails are rigidly mounted on each side of the seat base and the linear carriages are connected to the seat pan via ball bearings in order to achieve a pitch rotational degree of freedom. The vertical and rotational motions of the seat pan are illustrated using dashed lines in Figure 5.1. The three-dimensional line drawings of the assembled active seat are shown in Figure 5.2. The unit of all the dimensions in the line drawings is millimetres.

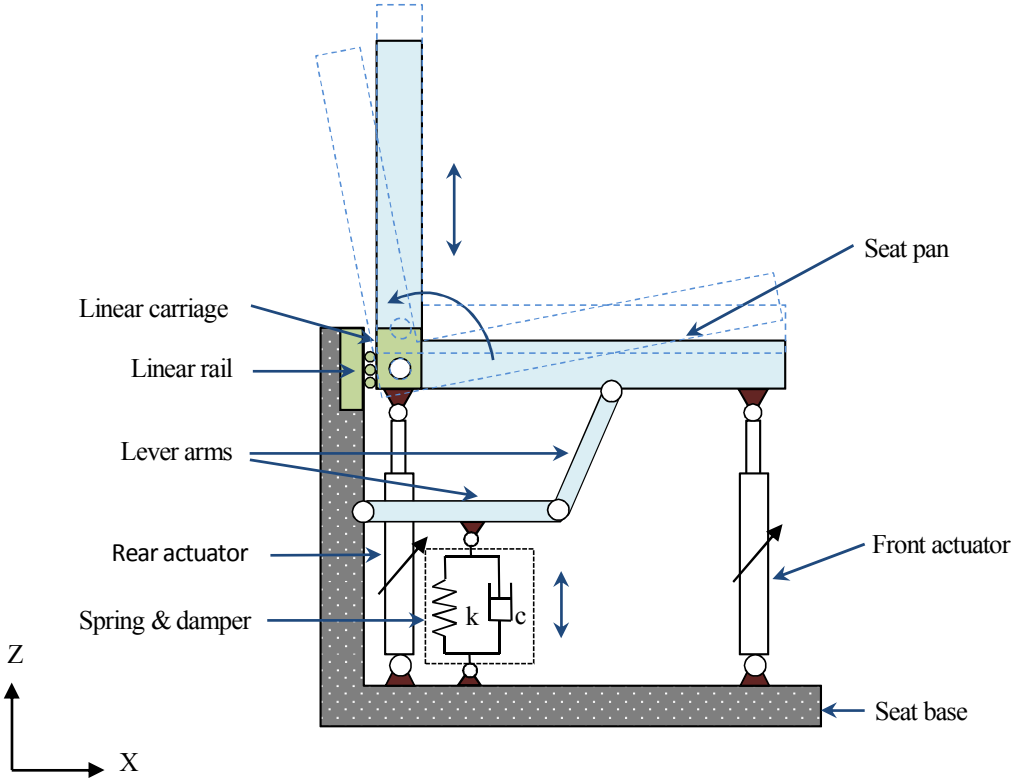

Figure 5.1: Mechanical model of the active seat.

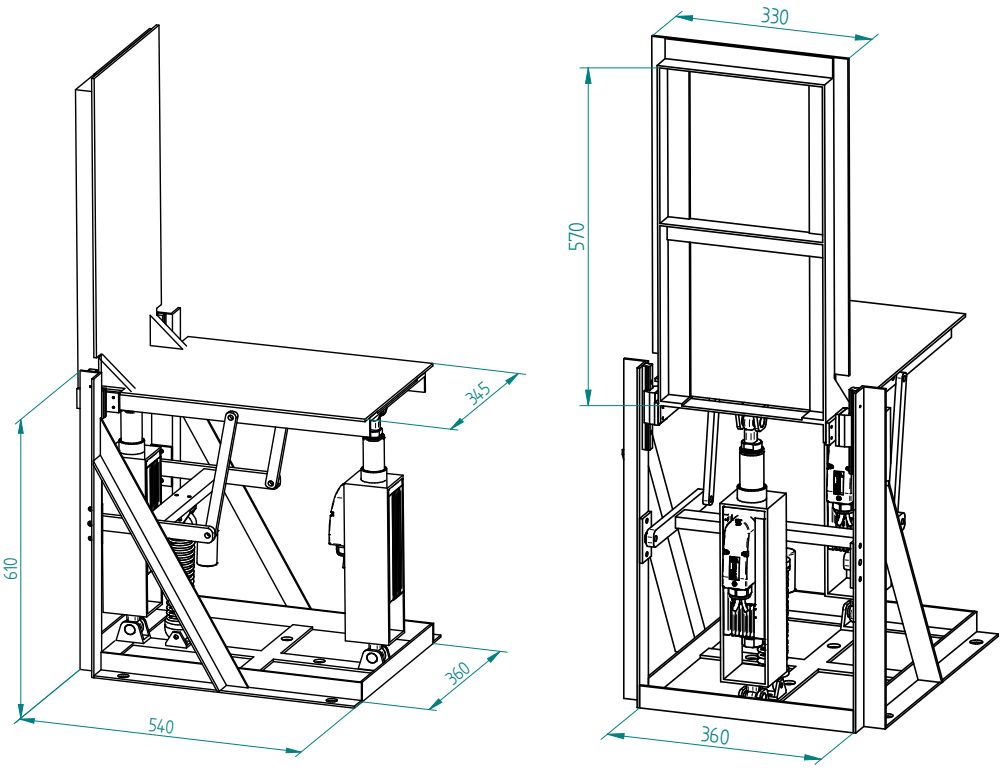

Figure 5.2: Line drawings of the assembled active seat.

5.1.2 Two-bar lever mechanism

The line drawings of the two-bar lever mechanism are shown in Figure 5.3. The lever was designed to obtain an appropriate supporting force from the spring and damper while keeping the passive suspension structure simple. Pin joints were used for the connections to maintain free rotation. The static ratio of the load force to the supporting force is approximately 2.6. As the seat pan moves up and down, the lower bar will rotate about the hinge A and the ratio will vary accordingly.

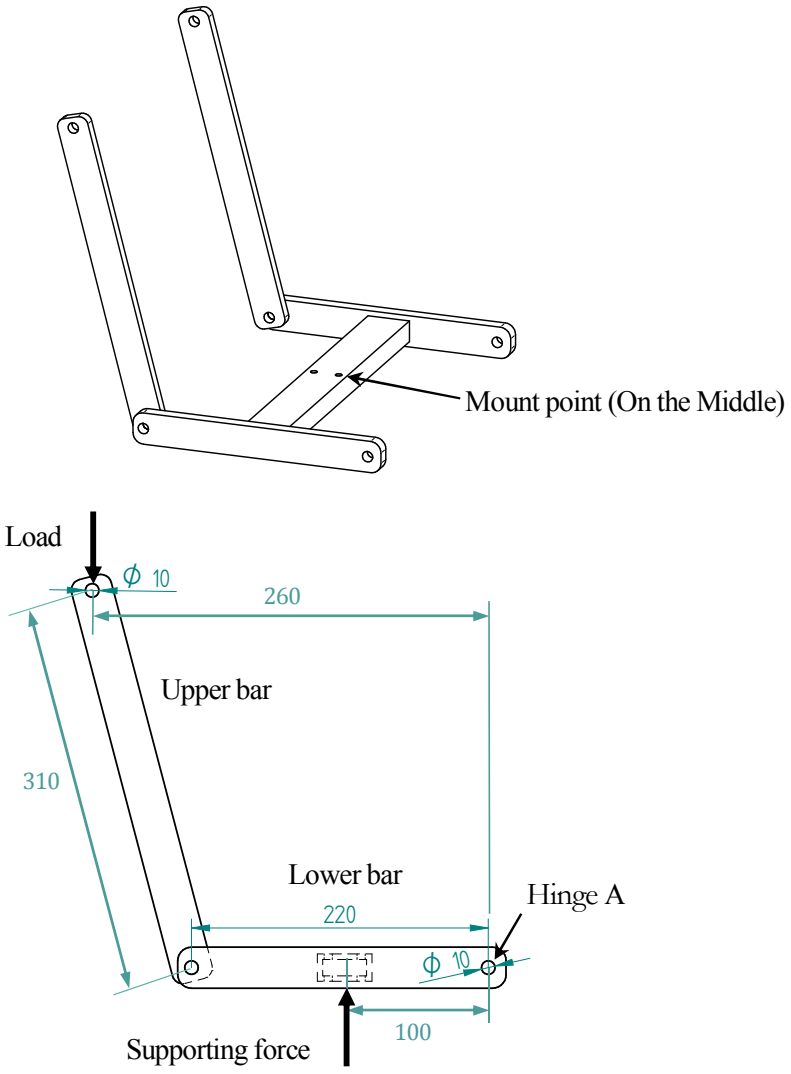

Figure 5.3: Line drawings of the two-bar level mechanism.

5.1.3 Linear slider mechanism

The line drawings of the linear slider mechanism are shown in Figure 5.4. As mentioned above, the linear sliders were used to allow the seat pan to move up and down vertically along the rail guides. The rail guides were rigidly mounted on each side of the seat base and the free moveable range for the carriage was ±45 mm approximately. Two ball bearings were mounted on the linear carriages using an attached holder plate to allow free rotation.

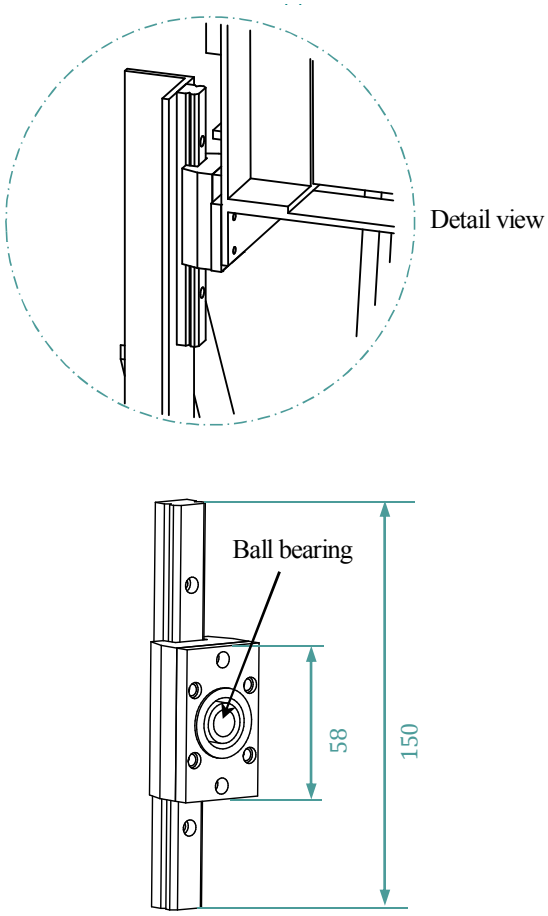

Figure 5.4: Line drawings of the linear slider mechanism.

5.1.4 Passive shock absorber

As shown in Figure 5.1, the two-bar lever is supported by a damper and spring unit, which constitutes the passive suspension of the active seat. To suit the design requirement, an Elka-stage-5 shock absorber which consists of a steel coil spring and an adjustable damper was selected as the passive suspension element. Figure 5.5 shows a photograph of the shock absorber.

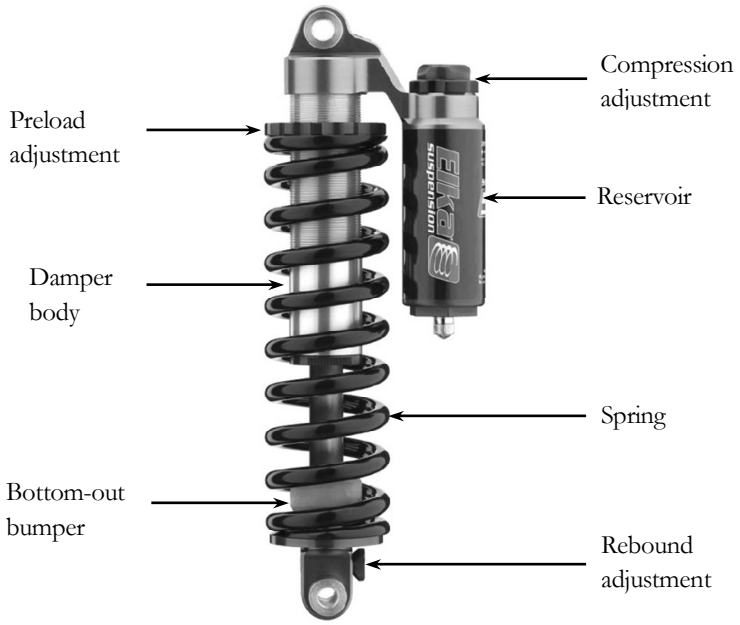

Figure 5.5: Photograph of the shock absorber.

5.1.5 Active actuation element

Two XTA-3806 electromagnetic linear actuators manufactured by the Dunkermotoren GmbH were chosen as the active struts. The actuators were installed in parallel at the front and the rear of the seat pan to provide active control authority in bounce and pitch. Figure 5.6 shows a photograph of the actuator. The specifications of the actuator are listed in Table 5.1.

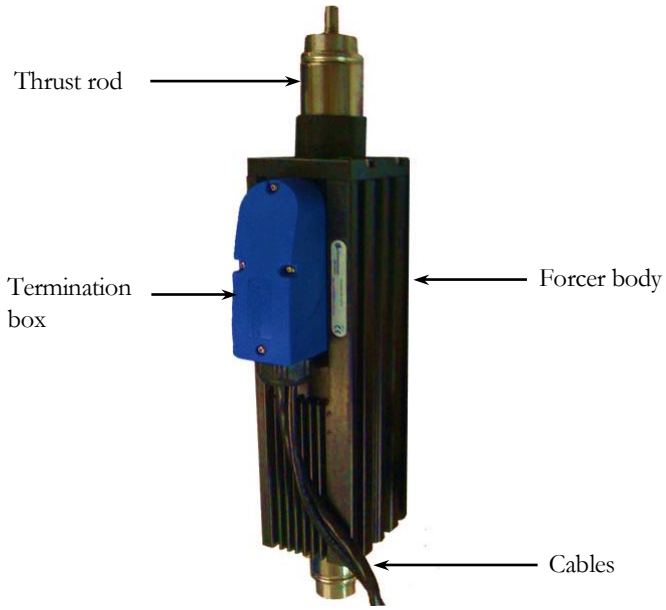

Figure 5.6: Photograph of the actuator.

Table 5.1: Actuator specifications.

Parameter	Value	Unit
Stroke	±30 (Limited range)	(mm)
Peak force	1116	(N)
Continuous stall force	168.2	(N)
Force constant	78.9	(N/Arms)
Peak acceleration	313	(m/s^2)
Maximum speed	3.8	(m/s)
Thrust rod mass/metre	8.3	(kg/m)
Forcer mass (excluding thrust and cables)	3.75	(kg)

5.2 Active seat dynamics

5.2.1 Shock absorber dynamics

The passive spring stiffness, at a lever ratio of 2.6, was chosen to achieve around 30 mm of compression under a load of an average adult. The stiffness of the spring and the damper characteristics were identified through experimental tests. Three separate sets of tests were conducted: spring force tests, damper force tests and resultant force (i.e. combined spring and damper force) tests. These tests were carried out on a suspension dynamometer, and two sinusoidal input speeds were chosen for each set of tests.

Figure 5.7 and 5.8 show the plots of the spring force against displacement and velocity, respectively. The spring constant was calculated to be 71.97 kN/m and is indicated by the black thick line in Figure 5.7.

The damper force against the displacement and velocity plots are shown in Figure 5.9 and 5.10, respectively. A hysteretic and non-linear behaviour of the damper is observed in the force-velocity curve. The damper force is around 200 N with a speed of 0.15 m/s.

Figure 5.11 and 5.12 show the plots of the resultant force against the displacement and velocity, respectively.

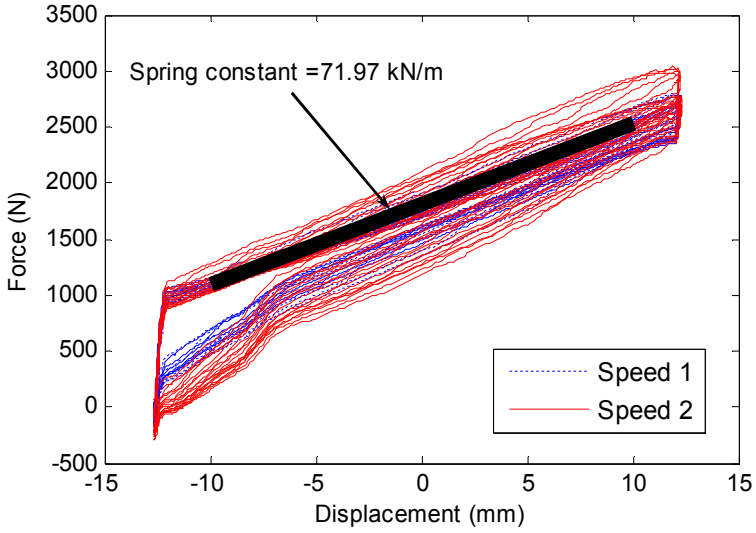

Figure 5.7: Spring force against displacement.

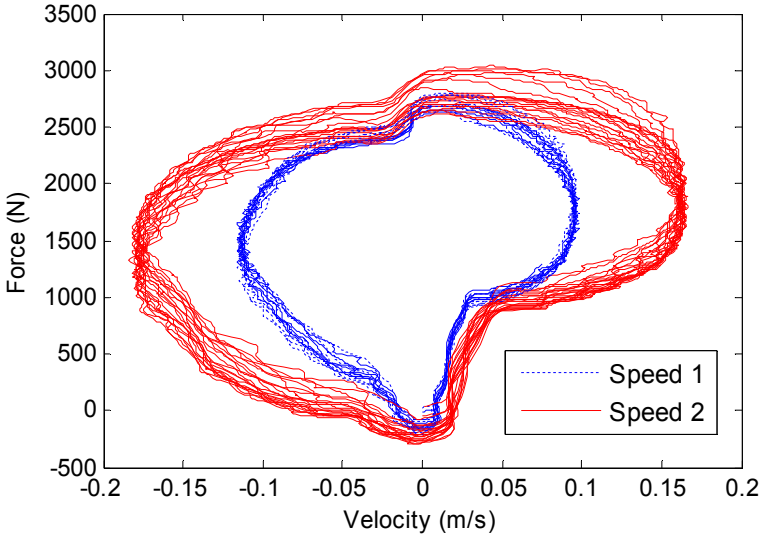

Figure 5.8: Spring force against velocity.

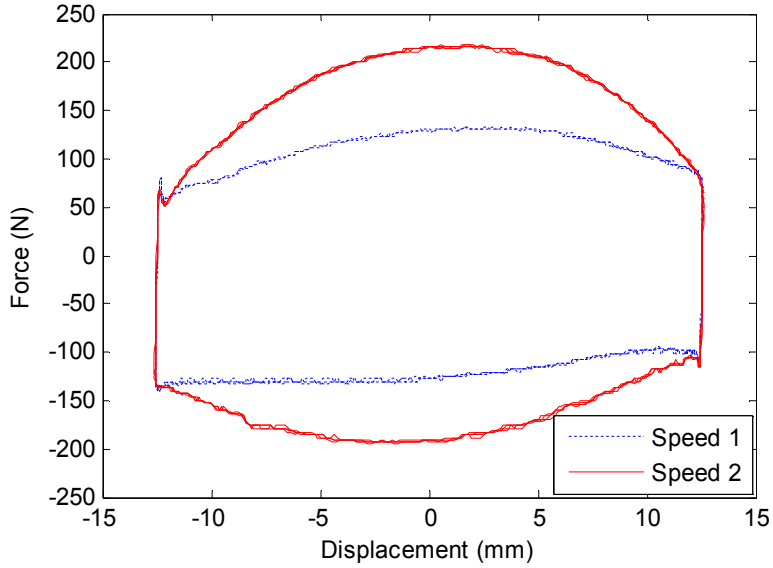

Figure 5.9: Damper force against displacement.

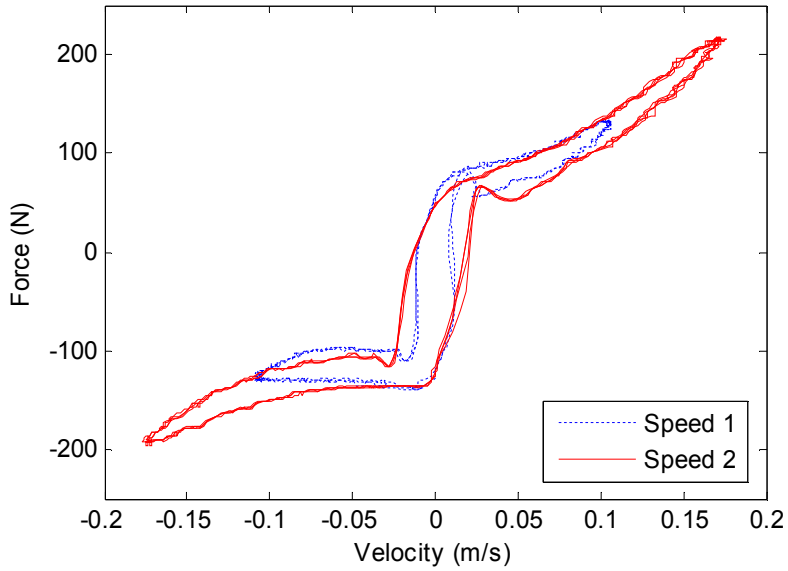

Figure 5.10: Damper force against velocity.

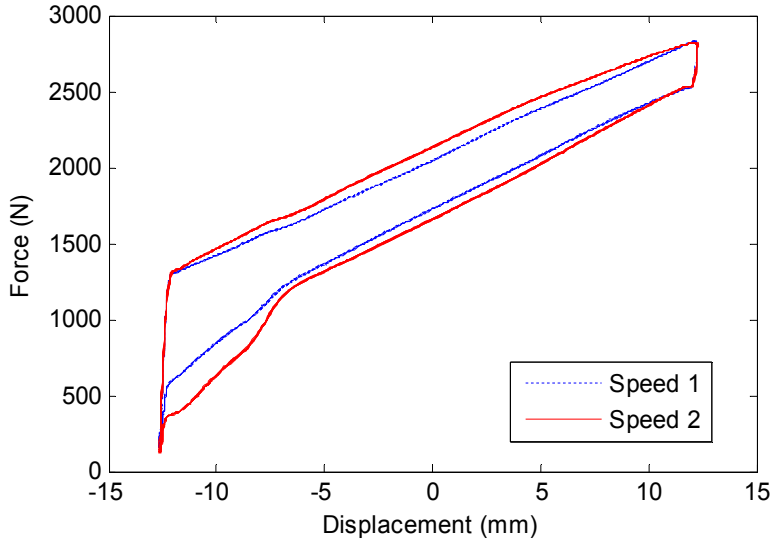

Figure 5.11: Resultant force against displacement.

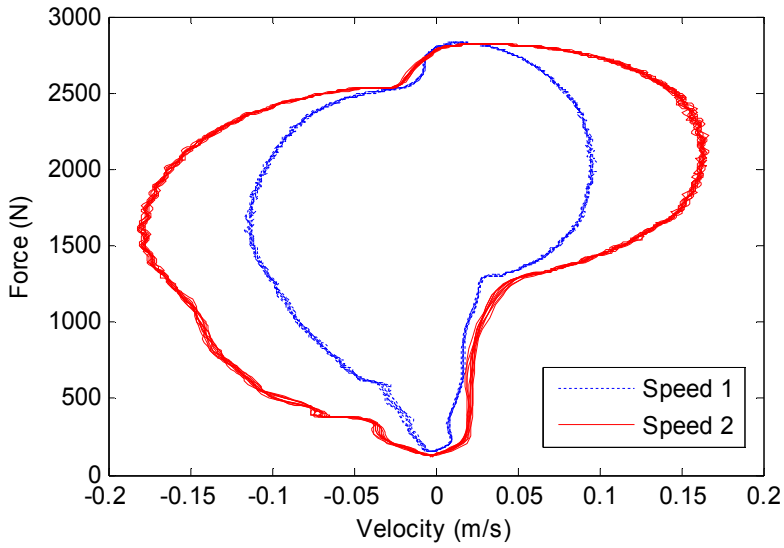

Figure 5.12: Resultant force against velocity.

5.2.2 Vibration transmissibility of the empty seat

Experimental tests were carried out using the University of Bath MAST (Multiple Axis Simulation Table) to identify the dynamic characteristics of the active seat. As shown in Figure 5.13, the vibration transmissibility in the vertical axis from the seat base (MAST input) to the seat pan without external load and with the actuators powered off was measured. This was obtained by measuring the acceleration level at the seat base and the seat pan simultaneously under sinusoidal excitation in the frequency range of 1-25 Hz with a frequency interval of 0.5 Hz and input acceleration range of 0.05-5 g. The transmissibility curve reveals a dominant resonant frequency between 10 and 14 Hz, and the associated peak magnitude is over 2.

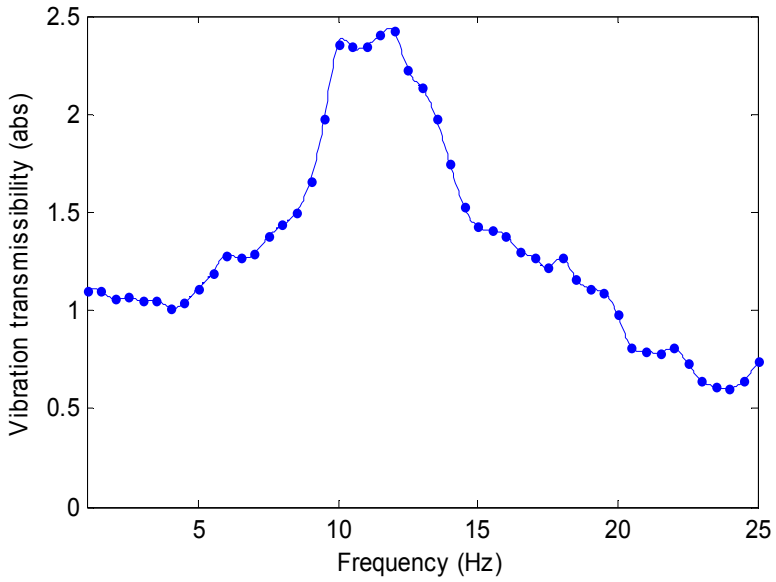

Figure 5.13: Empty seat vibration transmissibility from the seat base to the seat pan.

5.2.3 Frequency responses of the empty seat

Figure 5.14 shows the magnitude and phase responses of the active seat under the excitation force generated by the two actuators. Sinusoidal signals starting from 0.5 Hz to 25 Hz with a frequency interval of 0.5 Hz were used to drive the actuators. Three different force levels: peak values at 55.8 N, 83.7 N and 111.6 N for each actuator, were chosen for the response test. It can be observed that there are distinctive peaks in the magnitude response curves between the 10-20 Hz frequency range, and these are due to the resonance near the

fundamental frequency of the active seat. It is also found that the frequency range of the resonance tends to broaden as the excitation force increases. The phase responses show a general good consistency below 10 Hz and a bigger difference between 10 Hz and 25 Hz. This is caused by the non-linearity of the seat system. Moreover, the fundamental frequency of the active seat increases compared with those revealed by the transmissibility curve, shown in Figure 5.13, when the actuators are powered off. This is because the overall dynamic stiffness of the system is increased by the added force when the actuators are powered on.

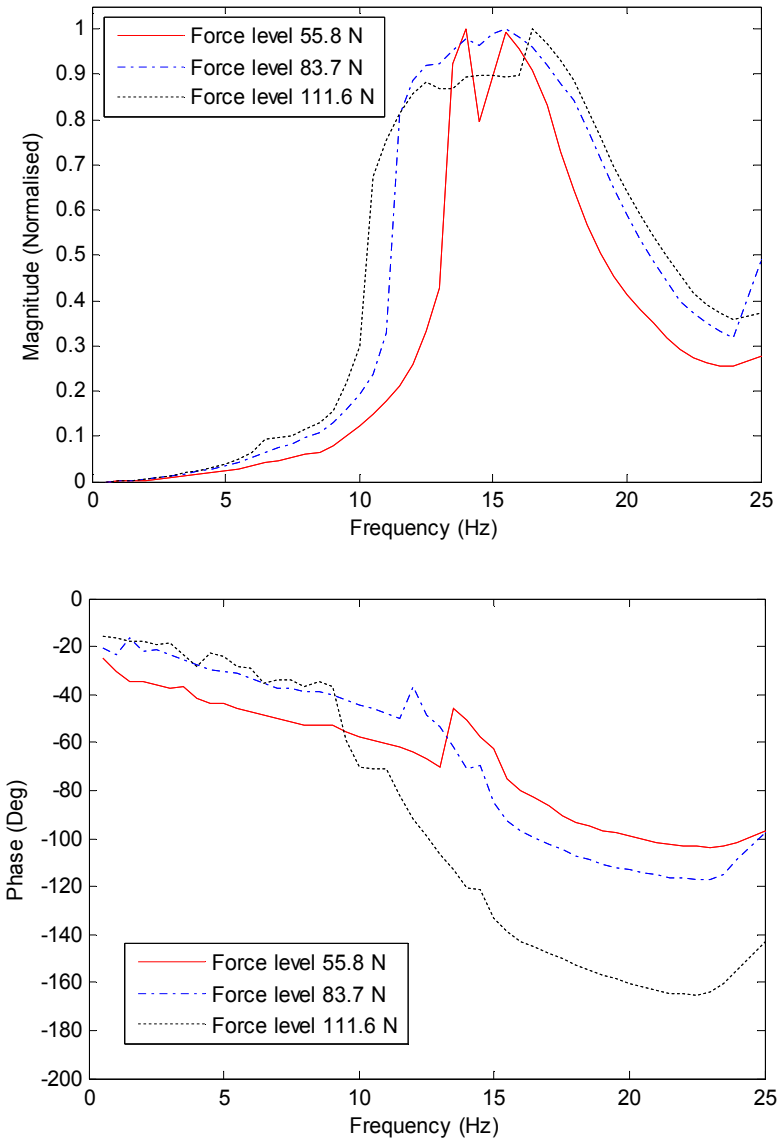

Figure 5.14: Magnitude and phase responses of the empty seat under the actuator excitation force.

5.2.4 Frequency responses of the active seat with a dummy

Figure 5.15 shows the magnitude and phase responses of the active seat with a dummy under the excitation force generated by the two actuators. Similarly, sinusoidal signals starting from 0.5 Hz to 25 Hz with a frequency interval of 0.5 Hz were used to drive the actuators. Two different force levels: peak values of 83.7 N and 111.6 N for each actuator, were chosen for the response test. It can be observed that the first resonance of the active seat goes down to below 10 Hz due the added mass of the dummy. Good consistency can be observed between the magnitude responses using two different force levels above 6 Hz.

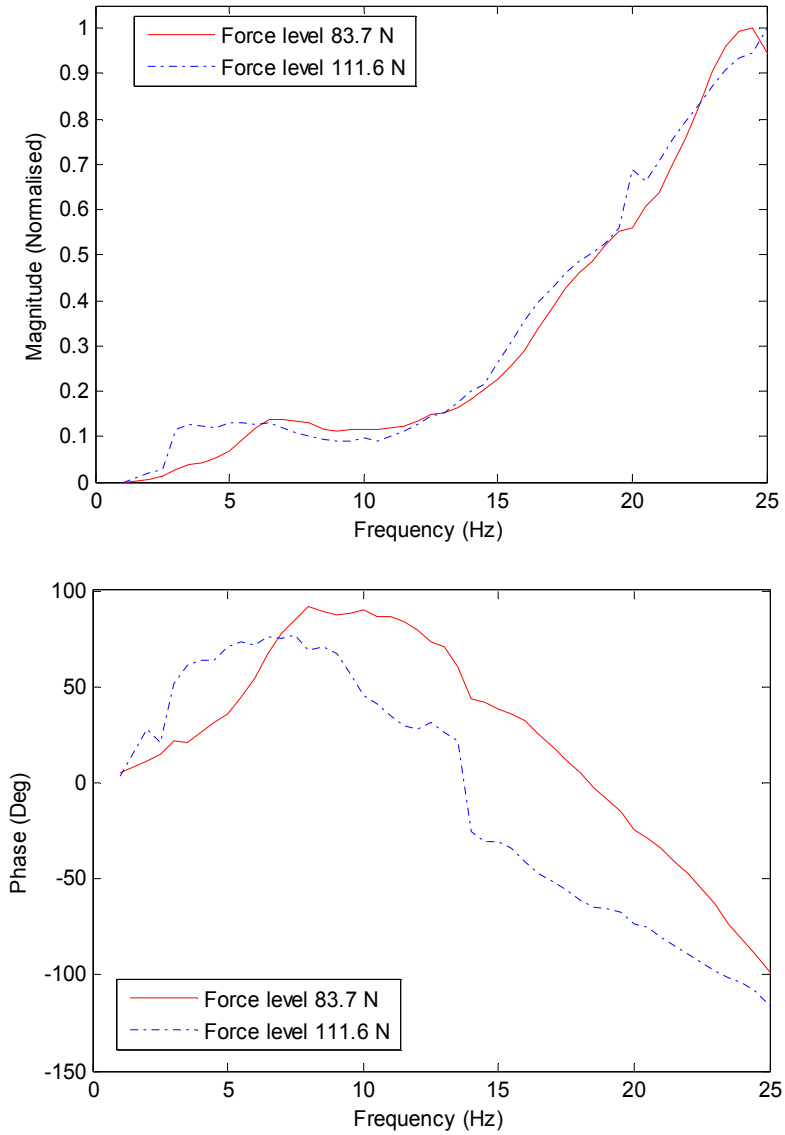

Figure 5.15: Magnitude and phase responses of the active seat with a dummy under the actuator excitation force.

5.3 Active seat dynamics discussions

The experimental tests revealed the characteristics of the shock absorber. The hysteretic and non-linear behaviour of the shock absorber contributed to the overall non-linearity of the active seat's passive suspension.

The vibration transmissibility of the empty seat from the seat base to the seat pan with the actuators powered off shows a dominant resonant frequency between 10 and 14 Hz, and the associated peak magnitude is over 2. The empty seat dynamics have also been illustrated by the frequency response of the seat to active force inputs. Some distinctive peaks are observed in the magnitude response curves in the 10-20 Hz frequency range for all the three different excitation force levels. These resonant frequencies are different to those of the passive seat with the actuators de-energised as it would seem that the stiffness of the system was increased by the additional force generated by the actuators. It was also found that the frequency range of the resonance tends to broaden as the excitation force increases, which indicates a non-linear system. The phase responses show a general good agreement below 10 Hz and a bigger difference between 10 Hz and 25 Hz.

The frequency responses of the active seat with a dummy show no obvious resonant peak in the frequency range of interest (1-25 Hz). The magnitude responses obtained by using two different excitation force levels show a good consistency above 6 Hz. However, a relatively big difference can be found between the phase responses. The results also show that the active seat dynamics changed significantly when an external load (i.e. the dummy) was added.

From the above dynamic analysis, it can be seen that the active seat system is subject to complex non-linear behaviour. Furthermore, the system is also influenced by the time-varying effects which would result from the external load disturbance (i.e. occupant's weight variations), temperature changes and ageing of the system. As such it would prove difficult to design a linear controller for active vibration isolation using this system and a more sophisticated controller is likely to be required.

5.4 Conclusions

The details of the active seat structure and dynamics were described and illustrated in this chapter. The active seat was designed and built on the basis of the required vibration isolation performance in a low frequency excitation range of (1 - 25 Hz). The characteristics of the active seat dynamics were identified through experimental tests. Based on the identified system dynamics, the rig is suitable for the development of an active seat to attenuate the vibration experienced by a passenger in a vehicle.

Chapter 6

Experimental Studies: Feedforward Plus PI Control Tests

The vibration cancellation performance of the active seat was initially examined by feedforward plus proportional-integral (PI) control tests. Firstly, the system was tested by cancelling a single frequency excitation. Then, multiple harmonics cancellation tests were carried out. Moreover, the system was also tested under low-frequency large amplitude disturbances. The purpose of these tests is to investigate the vibration cancellation capability of the active seat with simple controllers and gain an understanding of the real-time implementation.

6.1 Feedforward plus PI feedback control

Combined feedforward plus proportional-integral-derivative (PID) feedback control is one of the most commonly used strategies in different control applications due mainly to the simplicity of its structure and implementation. For the purpose of an initial investigation of the vibration cancellation performance of the active seat, a combined feedforward plus PI (the derivative was set to zero in this case) controller was applied to the system.

Figure 6.1 shows the block diagram of the implementation of the feedforward plus PI controller on the active seat. The diagram consists of the feedback loop with feedback PI controller, active cancellation path $S(z)$, measured seat base vibration signal $v(n)$, control signal $u(n)$, and error signal $e(n)$. The seat base vibration is transmitted through the passive seat suspension causing a disturbance $d(n)$ which influences the feedback

loop. The measured seat base vibration is fed through the feedforward controller G_{ff} to compensate the disturbance effects.

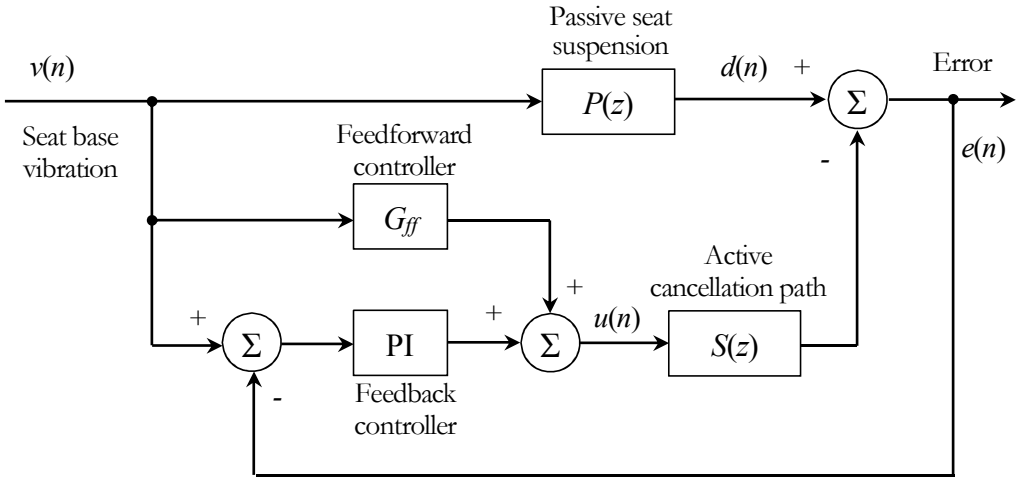

Figure 6.1: Implementation of the feedforward plus PI controller on the active seat.

The feedforward controller in this application is of the form of a discrete-time lead-lag compensator with gain:

$$G_{ff}(z) = K_{ff}\frac{Z - T_z}{Z - T_p} \tag{6.1}$$

where K_{ff} is the gain of the feedforward controller. The DC gain (i.e. the low-frequency gain) of the lead-lag compensator is equal to $(1\text{-}T_z)/(1\text{-}T_p)$, where T_z is the zero and T_p is the pole of the compensator. The controller implements a lead compensator when $0<T_p<T_z<1$, and implements a lag compensator when $0<T_z<T_p<1$.

The parameters of the feedforward controller were found based on the identified system dynamics in Chapter 5. The PI controller parameters were tuned by using the Ziegler–Nichols method. All parameters are not optimal in any sense. However, empirical iterations were carried out to exploit the whole potential of the control system.

6.2 Experimental setup

The established experimental apparatus is shown in Figure 6.2. The active seat was rigidly mounted on the platform of a multi-axis vibration simulation table (MAST). A vibration test dummy, whose dynamic characteristics are presented in Chapter 4, was used as a seated human body substitute in the tests in order to ensure an improved consistency in behaviour and avoid safety and ethical issues. The dummy was secured on the seat using a standard seat belt and a chest strap. A total of four piezoresistive accelerometers (Entran, EGCS-D1CM-25) were used to measure the acceleration levels and provide feedback signals. The mounting locations of the accelerometers are: the simulator platform (i.e. seat base), the middle of the seat pan, the dummy pelvis and the dummy shoulder. All the acceleration measurements were in the vertical direction. The I/O interface is a NI PCI-6229 board and the control algorithm was implemented on a xPC target system with a sampling rate of 1 kHz. The specification of the experimental setup is given in Table 6.1.

Table 6.1: Specification of the experimental setup.

Number	Name	Specification
1	MAST	Operational frequency range:0-50 Hz Stroke: ±75 mm Peak acceleration: 60 ms^{-2}
2	Test dummy	Mass: 55 kg (Seated human body mass supported by the seat)
3	Accelerometer (EGCS-D1CM-25)	Frequency response range: 0-240 Hz Sensitivity: 8 mV/g Non-linearity: ±1% FSO
4	I/O board (NI PCI-6229)	16-Bit, 250 kS/s, 32 analog inputs and 4 analog ouputs

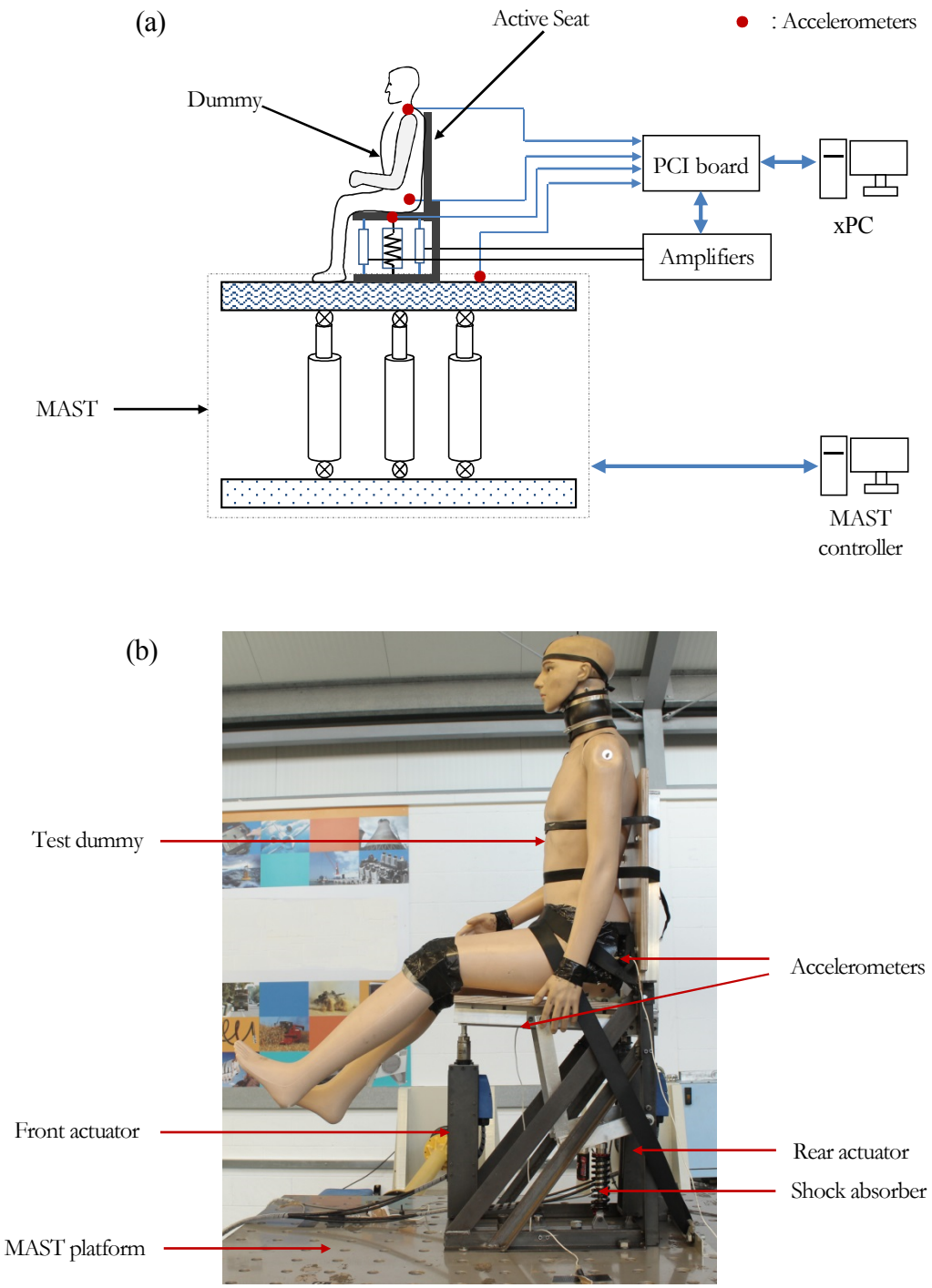

Figure 6.2: The experimental setup.

6.3 Experimental results

In the experimental studies, the residual vibration on the seat pan was selected as the error signal. The vibration signal on the simulator platform (i.e. seat base) was used to drive the feedforward controller. Initially, the system was configured to cancel a sinusoidal vibration at a single frequency. Then, the system was tested by cancelling of a periodic vibration comprising 5 harmonic frequencies: 2, 4, 6, 8 and 10 Hz. Additionally, the vibration cancellation performance of the system under low-frequency large amplitude disturbances was also investigated. The experimental results are presented in the following sections.

6.3.1 Single frequency cancellation

In this set of tests, 4 separate single frequency excitations: 2, 4, 6, and 8 Hz sine waves were chose and applied to the system. The peak input acceleration for each excitation is approximately: 0.02 g, 0.05 g, 0.08 g and 0.13 g, respectively. The experimental data was filtered through a 0.5-25 Hz band-pass filter and recorded in time series. The duration of each test was 30 seconds and the controller was switched on 10 seconds after the test was begun. The parameters of the feedforward and PI controllers are listed in Table 6.2.

Table 6.2: Parameters used for the feedforward and PI controllers.

Excitation frequency	Lead compensator	Feedforward gain	P	I
2 Hz	(Z-0.98)/(Z-0.15)	9000	10	0.1
4 Hz	(Z-0.995)/(Z-0.001)	3400	15	0.1
6 Hz	(Z-0.993)/(Z-0.001)	1600	10	0.1
8 Hz	(Z-0.993)/(Z-0.001)	1700	10	0.1

Figure 6.3 shows the vibration cancellation results on the seat pan in the time domain. It is observed that a good level of vibration cancellation was achieved after the controller was turned on for all the tests. The largest reduction was approximately 70% at the 4 Hz single frequency test.

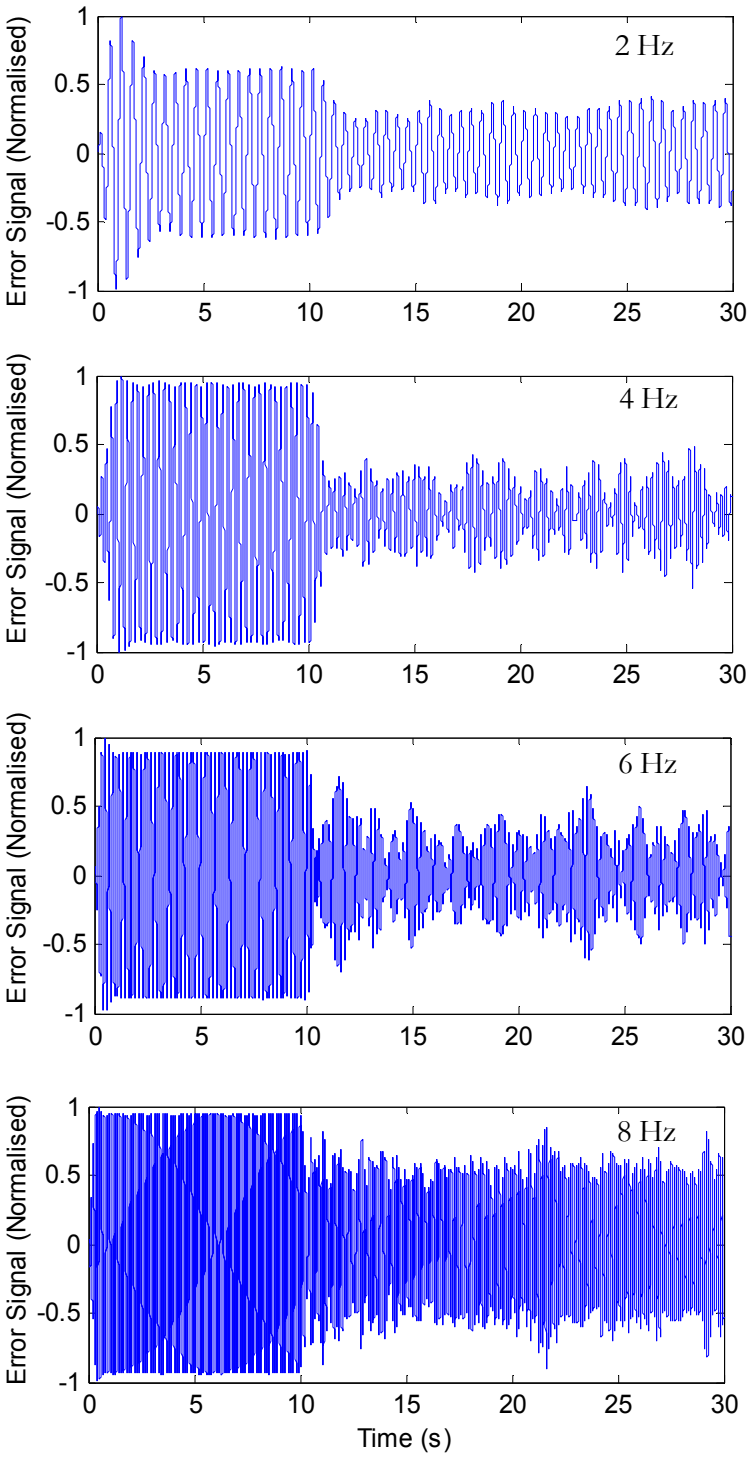

Figure 6.3: Single frequency cancellation results in the time domain.

The experimental data has also been presented in the frequency domain, as shown in Figure 6.4 and 6.5, by applying FFT transform. In these plots, the original uncontrolled vibration on the seat pan was obtained by taking the power spectrum of the data set between 4 seconds and 10 seconds. The controlled vibration was obtained by taking the power spectrum of the data set between 15 seconds and 30 seconds. Both of the data sets in the test ramp up and the control transient periods were excluded from the calculation.

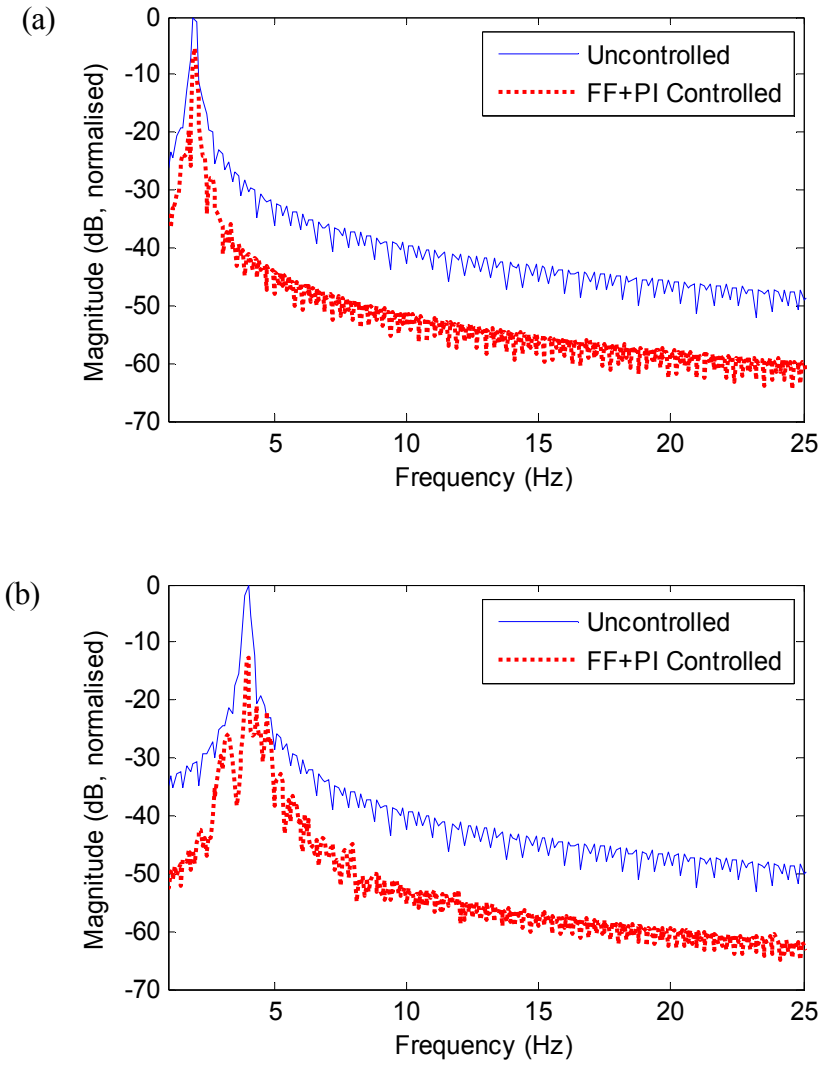

Figure 6.4: Single frequency cancellation results in the frequency domain: (a) 2 Hz result, (b) 4 Hz result.

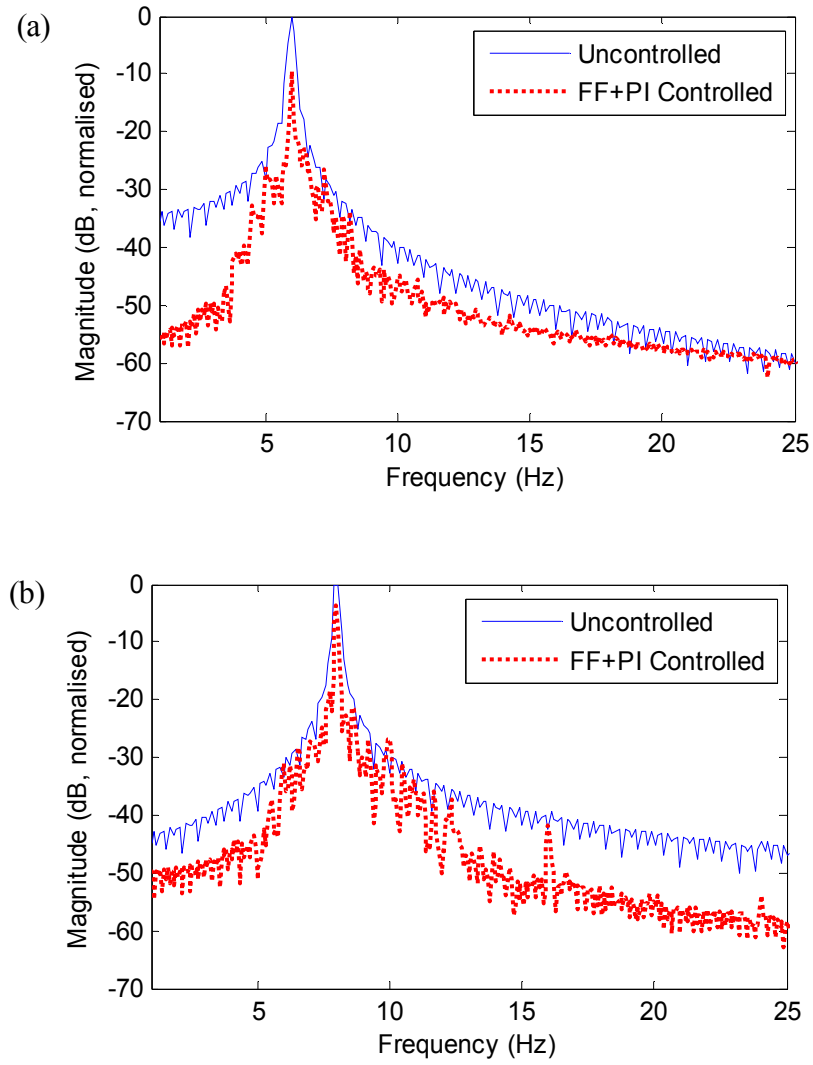

Figure 6.5: Single frequency cancellation results in the frequency domain: (a) 6 Hz result, (b) 8 Hz result.

6.3.2 Multiple harmonics cancellation

A vibration signal containing five harmonic frequencies: 2 Hz, 4 Hz, 6 Hz, 8Hz and 10 Hz, was used to excite the system. The overall peak input acceleration is 0.1 g approximately. The lead compensator is (Z-0.995)/(Z-0.001), the feedforward gain is 800, the **P** value is 1 and the **I** value is 0.1. The duration of each test was 30 seconds and the controller was switched on 10 seconds after the test was begun. The cancellation results are presented in Figure 6.6. Again, these plots were obtained by taking the power

spectrum of the data set in the stable periods: 4-10 seconds for the original uncontrolled result; 15-30 seconds for the controlled result.

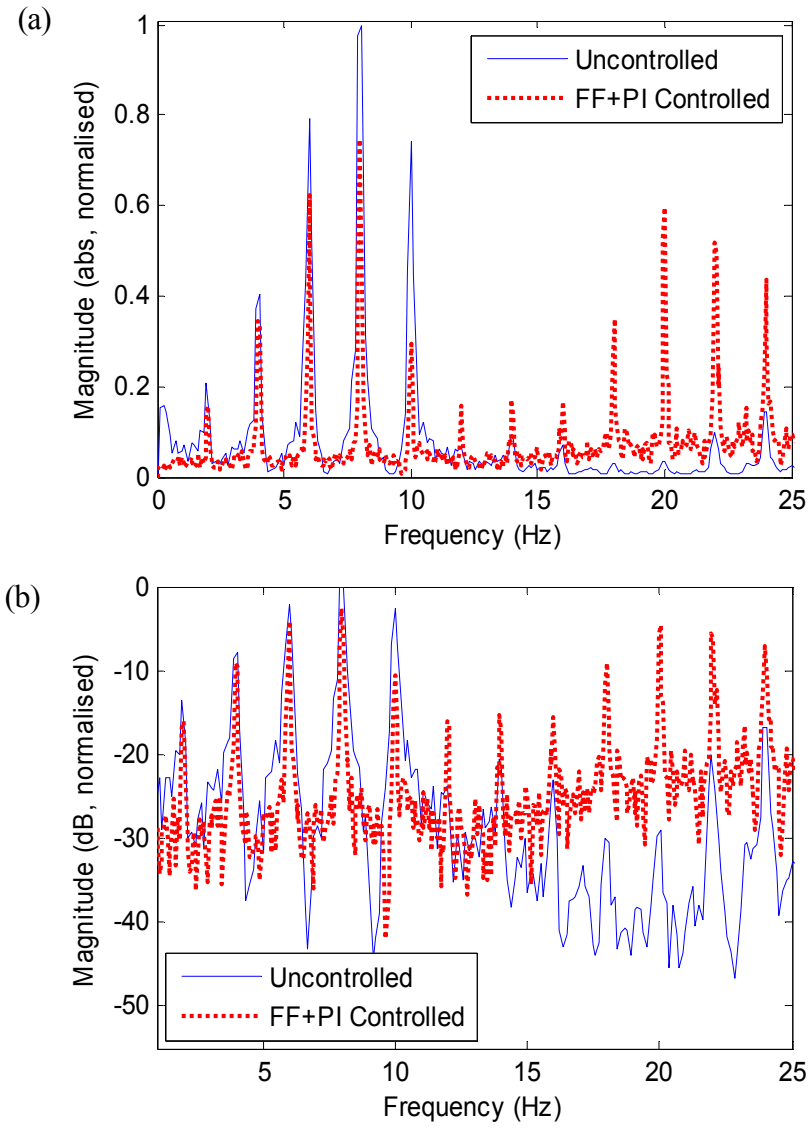

Figure 6.6: Cancellation results of the multiple harmonics test:
(a) Normalised magnitude in abs, (b) normalised magnitude in dB.

As can be seen, no substantial cancellation level was achieved for the multiple harmonics disturbance. A good reduction is found at 10 Hz, but the cancellation is not extensive for the rest frequencies. It is also noted that some higher harmonics were excited by the active cancellation force, which, adversely, makes the vibration in the higher frequency range worse with control.

6.3.3 Performance under low-frequency large amplitude disturbance

In practice, the target vibration frequencies are usually accompanied by some unfiltered low-frequency large amplitude disturbances. It is crucial that the control algorithm can effectively reject these disturbances during the operation. In this test, the performance of the active seat with feedforward PI controller was examined by cancelling a 6 Hz single frequency vibration (0.1 g peak input acceleration approximately) combined with a 1 Hz large amplitude disturbance (0.09 g peak input acceleration approximately). The lead compensator is (Z-0.993)/(Z-0.001), the feedforward gain is 1600, the **P** value is 10 and the **I** value is 0.1.

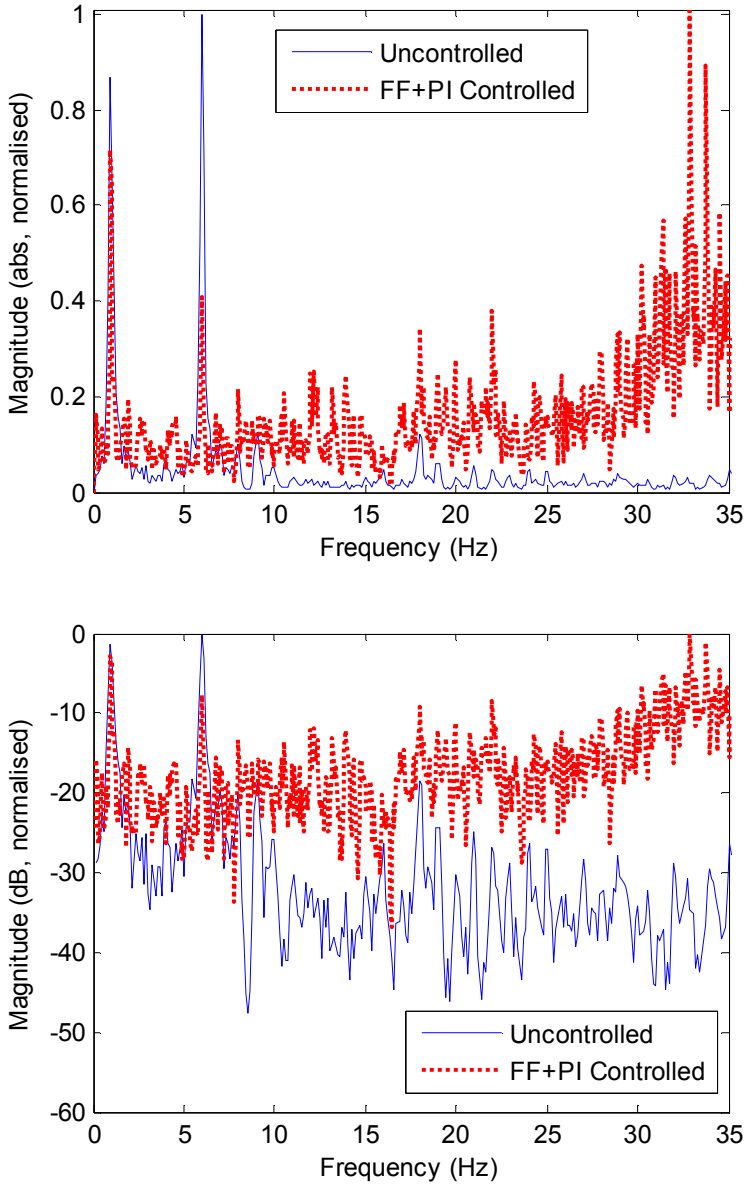

Figure 6.7: Cancellation performance under low-frequency large amplitude disturbance.

As shown in Figure 6.7, general good cancellation is achieved at the 6 Hz target frequency. However, substantial noise was introduced across the whole frequency region of interest, especially in the higher frequency range. To highlight this, the upper frequency limits of the plots were extended to 35 Hz. The deteriorated performance was found mainly caused by the saturated actuation force which resulted from the controller responding to the low-frequency large amplitude disturbance.

6.4 Problems and discussion

The initial experimental tests show that the active seat as a whole system works very promisingly in real-time implementation. A good level of vibration reduction was achieved for cancelling single frequency excitations, which indicates that the actuation system has an effective control authority. From the test results of the multiple harmonics cancellation and the cancellation under low-frequency large amplitude disturbances, some limitations of the feedforward plus PI controller were revealed. Firstly, the controller was not able to efficiently cancel multiple frequency components in the exaction signal. Secondly, the control performance was significantly influenced by the unfiltered low-frequency disturbance.

It is also noted that the parameters of the feedforward controller were chosen based on the identified system dynamics, which means that *a priori* knowledge of the system is required to implement the controller. In addition, the PI controller was found to be sensitive to the tuned parameters and easy to be unstable. What's more, as described in Chapter 5, the active seat system is subject to non-linear and time-varying behaviour which cannot be accommodated by the feedforward plus PI controller.

Therefore, in order to achieve effective vibration suppression and robust performance using the active seat, a control method which can adapt the non-linear and time-varying effects by performing on-line system identification could be used.

6.5 Conclusions

This chapter examined the vibration cancellation performance of the active seat using feedforward plus PI control method. Through these tests, the effectiveness of the actuators control authority was verified and an understanding of the real-time implementation was gained. However, these tests also revealed the limitations of the feedforward plus PI control method when applied to this non-linear system. This indicates that an advanced adaptive control strategy is required to exploit the whole potential vibration cancellation capability of the active seat.

Chapter 7

Adaptive Controller Design and Simulation

In this chapter, the derivation of the Least-Mean-Square (LMS) adaptive algorithm is presented. The secondary path effect in the implementation of the LMS algorithm is discussed and the Filtered-x LMS (FXLMS) algorithm is introduced for solving this problem. Different approaches for secondary path identification are compared and evaluated through simulation exercises. The fast-block LMS (FBLMS) algorithm is found to offer robust performance in the presence of destabilising signal content. Additionally, the effectiveness of the FXLMS algorithm with the FBLMS system identification is validated through a simulated system for narrow-band vibration cancellation.

7.1 The LMS adaptive algorithm

As is known, the active seat is subject to non-linear and time-varying behaviour. The use of a fully adaptive control strategy is required to maintain optimum vibration isolation performance. The LMS adaptive algorithm which was originally developed by Widrow and Hoff [52] has been applied to numerous active noise and vibration cancellation problems, and it has been found to offer a stable and robust performance. For the purpose of providing a necessary theoretical background, an overview of the derivation of the LMS algorithm is given in the following parts of this section.

The LMS algorithm is a linear adaptive filtering algorithm, which consists of a signal filtering process and a filter coefficients adaptive process. Generally, there are two filter structures that can be used for adaptive filtering: finite impulse response (FIR), shown in Figure 7.1, and infinite impulse response (IIR) structures [92]. The FIR, or transversal, filter incorporates only zeros and hence the filter is always stable. Also, the output of the FIR filter is dependent solely upon the input signal. The IIR filter is a recursive structure

(uses both input and feedback signals to compute the output) and it is not unconditionally stable. The LMS algorithm is based on the FIR filter structure.

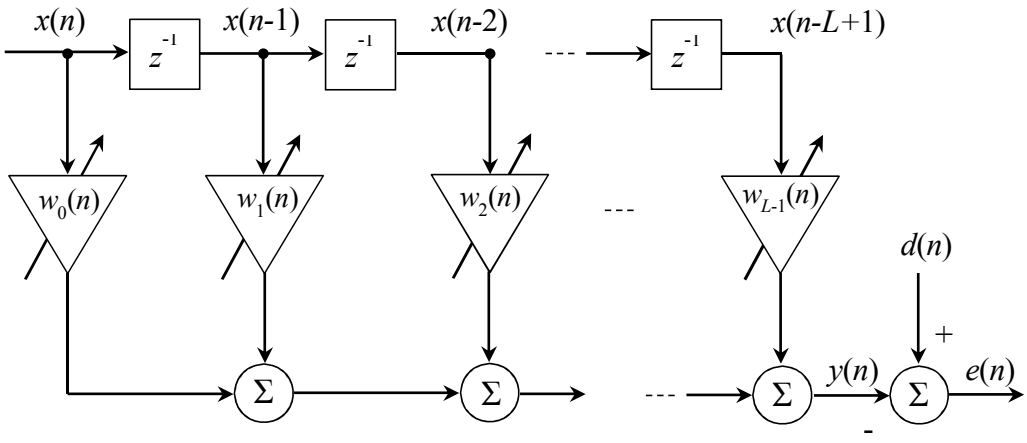

Figure 7.1: Adaptive FIR (transversal) filter structure.

As shown in Figure 7.1, the tap inputs $x(n)$, $x(n\text{-}1)$, …, $x(n\text{-}L\text{+}1)$, which form the L – by-1 input vector $\mathbf{x}(n)$, is obtained by operating L-1 unit delay elements z^{-1} upon the input signal $x(n)$. The filter coefficients vector $\mathbf{w}(n)=[w_0(n), w_1(n), \ldots, w_{L-1}(n)]$ is adjustable and updated by the LMS adaptive algorithm to minimise a cost function based on the measured error signal $e(n)$ between the desired response $d(n)$ and the filter output $y(n)$. The output signal $y(n)$ and the error signal $e(n)$ can be expressed by equation 7.1 :

$$y(n) = \mathbf{w}^T(n)\mathbf{x}(n) = \mathbf{x}^T(n)\mathbf{w}(n) \tag{7.1}$$

$$e(n) = d(n) - y(n) = d(n) - \mathbf{w}^T(n)\mathbf{x}(n) \tag{7.2}$$

Taking the square of equation 7.2 gives:

$$e^2(n) = d^2(n) - 2d(n)\mathbf{w}^T(n)\mathbf{x}(n) + \mathbf{w}^T(n)\mathbf{x}(n)\mathbf{x}^T(n)\mathbf{w}(n) \tag{7.3}$$

The cost function is based on the mean-square error (MSE):

$$\xi(n) = E[e^2(n)] \tag{7.4}$$

where $E[\cdot]$ denotes expected value which represents the statistical average of $e^2(n)$. Assuming the adaptive weight vector $\mathbf{w}(n)$ is a deterministic sequence, then the MSE performance function (i.e. the cost function) can be determined from equation 7.3, giving:

$$\xi(n) = E[d^2(n)] - 2\mathbf{p}^T\mathbf{w}(n) + \mathbf{w}^T(n)\mathbf{R}\mathbf{w}(n) \tag{7.5}$$

where $\mathbf{p}$ is the cross-correlation vector between the desired signal $d(n)$ and the tap input vector $\mathbf{x}(n)$

$$\mathbf{p} = E[d(n)\mathbf{x}(n)] = E\begin{bmatrix} d(n)x(n) \\ d(n)x(n-1) \\ \vdots \\ d(n)x(n-L+1) \end{bmatrix} \tag{7.6}$$

and $\mathbf{R}$ is the input autocorrelation matrix, which is defined as follows:

$$\mathbf{R} = E[\mathbf{x}(n)\mathbf{x}^T(n)]$$

$$= E\begin{bmatrix} x(n)x(n) & x(n)x(n-1) & \dots & x(n)x(n-L+1) \\ x(n-1)x(n) & x(n-1)x(n-1) & \dots & x(n-1)x(n-L+1) \\ \vdots & \vdots & \ddots & \vdots \\ x(n-L+1)x(n) & x(n-L+1)x(n-1) & \dots & x(n-L+1)x(n-L+1) \end{bmatrix} \tag{7.7}$$

It is noted that the MSE performance function $\xi(n)$ is a quadratic function of the tap weight $\mathbf{w}(n)$, assuming the tap input vector $\mathbf{x}(n)$ and the desired response $d(n)$ are jointly stationary. This function forms a $(L+1)$ dimensional MSE performance space (MSE surface) with a unique minimum at the point of zero gradient. For $L=2$, this corresponds to an MSE surface in a three-dimensional space [92].

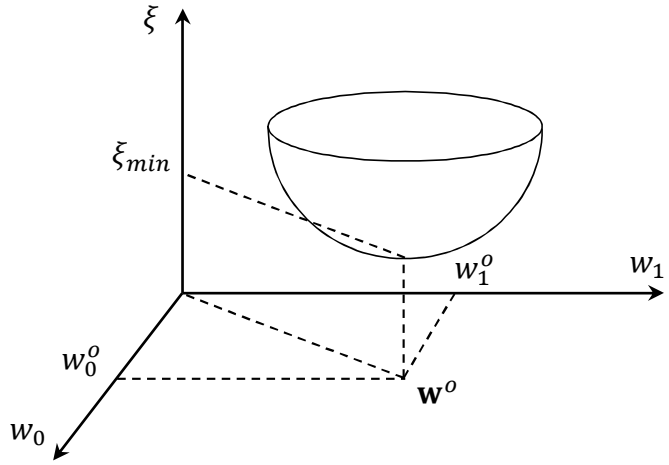

Figure 7.2: Three-dimensional MSE performance surface, L=2 case.

A generic three-dimensional MSE surface for the case L=2 is shown in Figure 7.2 [92], where $\mathbf{w}^o = [w_0^o \ w_1^o]^T$ is the optimal coefficient vector and ξ_{min} is the minimum MSE. It can be seen that adjusting the weights to minimize the MSE involves descending along the concave surface until reaching the "bottom of the bowl". The steepest-descent method in which the filter weights are updated at each iteration in the direction of the negative gradient of the error surface is ideally suitable for this purpose. The gradient of the error surface is defined as the vector of the directional derivatives:

$$\nabla\xi(n) = \begin{bmatrix} \frac{\partial\xi(n)}{\partial w_0(n)} \\ \frac{\partial\xi(n)}{\partial w_1(n)} \\ \vdots \\ \frac{\partial\xi(n)}{\partial w_{L-1}(n)} \end{bmatrix} = -2\mathbf{p} + \mathbf{2Rw}(n) \tag{7.8}$$

Setting $\nabla\xi(n) = \mathbf{0}$ in equation 7.8 gives the optimal solution for the filter coefficients, known as the Wiener-Hopf equation:

$$\mathbf{w}^o = \mathbf{R}^{-1}\mathbf{p} \tag{7.9}$$

It is noted that a considerable amount of computation is needed for this optimal solution as it requires continuous estimation of the autocorrelation matrix $\mathbf{R}$ and the

cross-correlation vector $\mathbf{p}$. Rather than explicitly finding the minimum point on the MSE surface, the LMS algorithm employs the steepest-descent method to converge upon the optimal solution. An initial guess of the filter weights vector $\mathbf{w}(n)$ is arbitrarily chosen to calculate the gradient vector $\nabla\xi(n)$ on the error surface. The next value of $\mathbf{w}(n)$ is obtained by adjusting the $\mathbf{w}(n)$ in the negative gradient direction, as shown in the following equation:

$$\mathbf{w}(n+1) = \mathbf{w}(n) - \frac{\mu}{2}\nabla\xi(n) \tag{7.10}$$

where μ is a positive real constant used to control stability and the rate of descent to the optimal point.

In many practical applications, it is not possible to evaluate the gradient vector $\nabla\xi(n)$ since that would require prior knowledge of the input signal $x(n)$. The LMS algorithm uses the instantaneous squared error, $e^2(n)$, to estimate the mean-square error given in equation 7.4. The autocorrelation matrices $\mathbf{R}$ and the cross-correlation vector $\mathbf{p}$ are now defined by the equations:

$$\hat{\mathbf{R}}(n) = \mathbf{x}(n)\mathbf{x}^T(n) \tag{7.11}$$

$$\hat{\mathbf{p}}(n) = d(n)\mathbf{x}(n) \tag{7.12}$$

where ($\hat{}$) denotes the instantaneous estimate.

The instantaneous estimate of the cost function (equation 7.5) becomes:

$$\hat{\xi}(n) = E[d^2(n)] - 2\hat{\mathbf{p}}^T(n)\mathbf{w}(n) + \mathbf{w}^T(n)\hat{\mathbf{R}}(n)\mathbf{w}(n) \tag{7.13}$$

By differentiating this estimate with respect to $\mathbf{w}(n)$, an instantaneous estimate of the gradient is obtained:

$$\hat{\nabla}\xi(n) = -2d(n)\mathbf{x}(n) + 2\mathbf{x}(n)\mathbf{x}^T(n)\mathbf{w}(n) \tag{7.14}$$

Substituting this instantaneous gradient estimate to equation 7.10 gives:

$$\mathbf{w}(n+1) = \mathbf{w}(n) + \mu\,\mathbf{x}(n)[d(n) - \mathbf{x}^T(n)\mathbf{w}(n)]$$

$$= \mathbf{w}(n) + \mu\,\mathbf{x}(n)e(n) \tag{7.15}$$

which is the LMS recursive algorithm.

The algorithm can be summarized as follows:

1. Compute the adaptive filter output

$$y(n) = \sum_{m=0}^{L-1} w_m(n)\; x(n-m) \tag{7.16}$$

2. Calculate the error signal

$$e(n) = d(n) - y(n) \tag{7.17}$$

3. Update the weight vector

$$\mathbf{w}(n+1) = \mathbf{w}(n) + \mu\,\mathbf{x}(n)e(n) \tag{7.18}$$

It can be seen that each iteration, the LMS algorithm only requires the most recent values of $\mathbf{x}(n)$, $d(n)$ and $\mathbf{w}(n)$. And only $2L$+1 multiplications and $2L$-1 additions are needed.

The stability condition of the LMS algorithm is [80]:

$$0 < \mu < \frac{2}{\lambda_{\max}} \tag{7.19}$$

where $\lambda_{\max}$ is the largest eigenvalue of the input autocorrelation matrix $\mathbf{R}$.

The stability constraint on μ is not practical to apply because computation of $\lambda_{\max}$ is very difficult when L is large. Therefore, it is desirable to estimate $\lambda_{\max}$ using a simple method in practical applications.

Since that

$$\lambda_{\max} \leq \sum_{m=0}^{L-1} \lambda_m = MP_x \tag{7.20}$$

where P_x denotes the power of $x(n)$, L is the length of filter weights. Therefore, the stability condition given in equation 7.19 can be satisfied by setting

$$0 < \mu < \frac{2}{LP_x} \tag{7.21}$$

From equation 7.21, it can be seen that the upper bound on μ is inversely proportional to the filter length and the input signal power. Small μ is required for large length filter and high power signals.

It also noted that practical implementation of the algorithm using DSP systems leads to the accumulation of rounding errors in the filter weight, which can result in poor performance and instability. A leakage factor β, chosen in the range $0 < \beta < 1$ and close to 1, may be applied to the weight update equation 7.15. In this case the LMS weight update equation becomes:

$$\mathbf{w}(n+1) = \beta\mathbf{w}(n) + \mu\,\mathbf{x}(n)e(n) \tag{7.22}$$

7.2 Effect of secondary path dynamics

The implementation of the LMS algorithm for an active vibration control (AVC) system is shown in Figure 7.3. The use of the LMS algorithm assumes that an error signal is available that is the difference between the primary disturbance signal $d(n)$ and the output of the adaptive filter $y(n)$. In the case of the active seat system, the output cancelling signal $y(n)$ will be modified by the transfer function $S(z)$, known as the secondary path dynamics, which includes the antialiasing filter, D/A and A/D converters, power amplifier, actuator and error accelerometer.

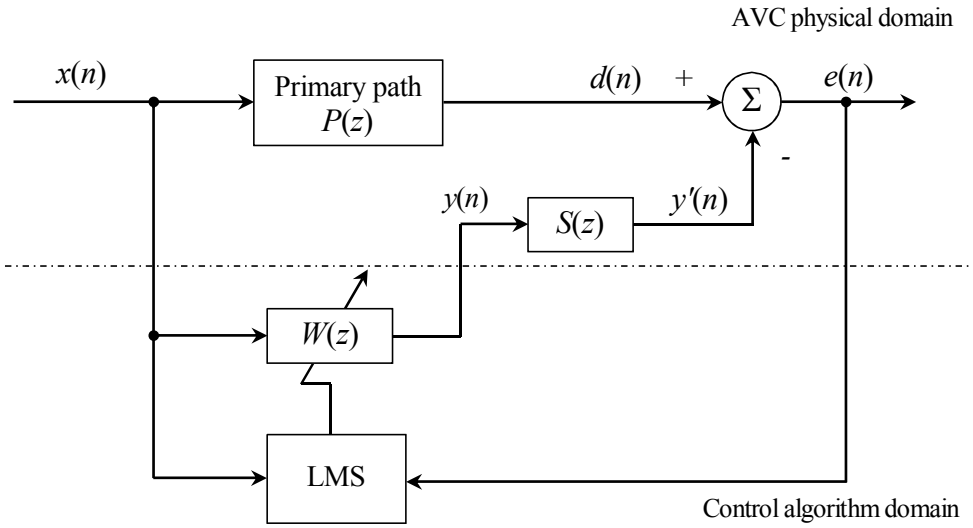

Figure 7.3: Block diagram of the LMS algorithm in AVC system.

The added secondary dynamics will result in a phase shift in the error signal $e(n)$, which means the error signal will not be correctly "aligned" in time with the reference signal $x(n)$. The presence of the phase shift will eventually cause instability. In order to implement the adaptive algorithm on the active seat system, a modification of the conventional LMS algorithm is therefore required to ensure the secondary path effect is compensated. In the next section, the Filtered-x LMS (FXLMS) algorithm is introduced for this purpose.

7.3 The FXLMS algorithm

The FXLMS algorithm is developed from the conventional LMS adaptive filter [52] to compensate the secondary path effect as mentioned above. It has been widely applied in the field of active noise and vibration control and it has been found to offer robust and effective performance for periodic vibration attenuation. The block diagram of the FXLMS algorithm in an active vibration control (AVC) system is depicted in Figure 7.4.

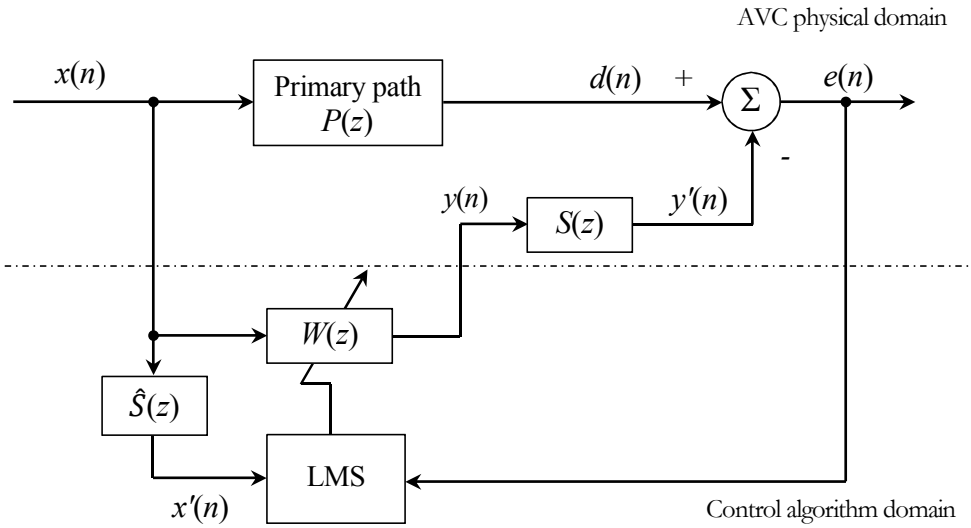

Figure 7.4: Block diagram of the FXLMS algorithm in AVC system.

The FXLMS algorithm solves the problem by placing an additional plant $\hat{S}(z)$, the estimate of the secondary path $S(z)$, in the reference signal path before the weight update of the LMS algorithm. The error signal $e(n)$ is given by the equation:

$$E(z) = D(z) - Y(z)S(z) = X(z)[P(z) - W(z)S(z)] \tag{7.23}$$

where $E(z), D(z), X(z)$ and $Y(z)$ are the z-transforms of the signal $e(n)$, $d(n)$, $x(n)$ and $y(n)$, respectively.

So for $E(z)$=0:

$$W(z) = \frac{P(z)}{S(z)} \tag{7.24}$$

With the added secondary path estimate $\hat{S}(z)$, the LMS update algorithm given in equation 7.15 now becomes:

$$\mathbf{w}(n+1) = \mathbf{w}(n) + \mu\, \mathbf{x}'(n)e(n) \tag{7.25}$$

where $\mathbf{x}'(n)=[x'(n)\ \ x'(n-1)\ \ \cdots\ \ x'(n-L+1)]^T$ is the filtered reference signal vector $\mathbf{x}(n)$ by the $\hat{S}(z)$, and is given by:

$$\mathbf{x}'(n) = \hat{S}^T(n)\mathbf{x}(n) \tag{7.26}$$

The FXLMS algorithm will converge providing the difference in phase between $S(z)$ and $\hat{S}(z)$ is not greater than 90^o [81]. The estimation of $S(z)$ is usually performed off-line, before the operation of active cancellation. However, in the case of the secondary path dynamic being time-varying, it is necessary to perform the on-line identification and cancellation processes simultaneously to assure the stability and convergence of the adaptive algorithm.

7.4 On-line secondary path identification techniques

As mentioned in Chapter 5, in the case of the active seat system, the secondary path dynamic is time-variant. Thus it is desirable to perform adaptive on-line secondary path identification. Therefore, $S(z)$ can be either occasionally or continuously estimated and the most recent estimate $\hat{S}(z)$ used in the adaptive control algorithm. Generally, the on-line secondary path identification techniques can be divided into two main categories: the techniques that use auxiliary random noise as an excitation signal and the one without using auxiliary noise (i.e. overall on-line secondary path modelling techniques).

7.4.1 Overall modelling technique

The overall on-line secondary path modelling technique has the capability to model the secondary path without using an additional excitation signal [82; 83]. The concept of this technique is illustrated in Figure 7.5 [92]. As it can be seen that an additional adaptive filter $\hat{P}(z)$ is introduced to model the primary path $P(z)$. Altogether, the complete AVC system uses three adaptive filters, $W(z)$, $\hat{S}(z)$ and $\hat{P}(z)$, to perform the secondary path identification and vibration cancellation tasks.

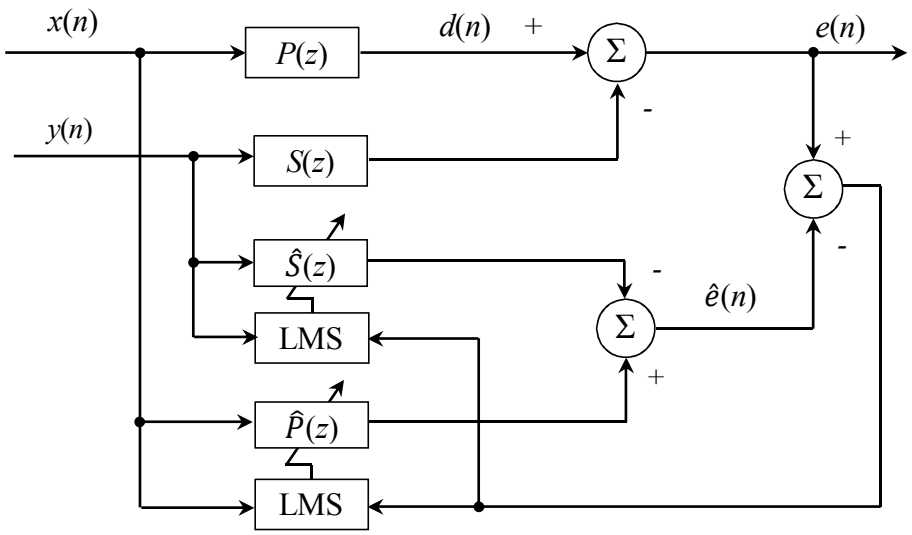

Figure 7.5: The concept of overall on-line secondary path modelling technique.

The convergence of the overall modelling algorithm depends on the secondary signal and thus on the primary noise. The obtained secondary path estimate is dependent on the frequency content of the primary disturbance, which may not have sufficient excitation over the entire band and furthermore may be changing. This can slow the convergence of the cancellation filter and reduce the system stability margin [92]. Detailed evaluations of this technique can be found in [84; 85].

7.4.2 Auxiliary random noise technique

The online secondary path modelling approach that uses auxiliary noise was early proposed by Eriksson and Allie [87], and later improved by many other researchers [84; 89; 90]. A block diagram of the technique using the LMS algorithm is shown in Figure 7.6.

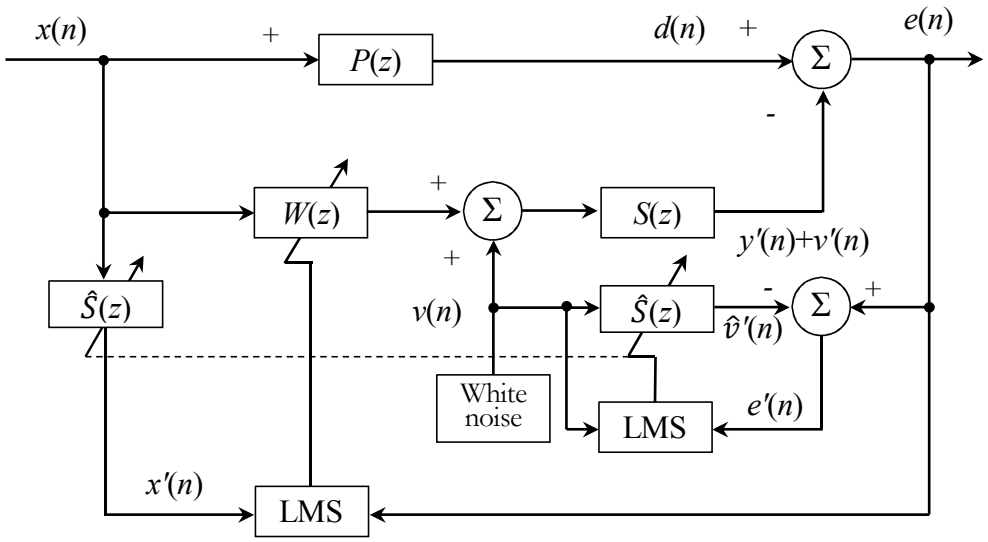

Figure 7.6: Block diagram of AVC system with on-line secondary path modelling using auxiliary random noise technique.

A low-level white noise $v(n)$, which is uncorrelated with the primary disturbance, is added to the secondary signal $y(n)$ produced by the adaptive filter $W(z)$ to drive the secondary source. The noise component is passed to the error signal $e(n)$ and fed back to an additional LMS filter $\hat{S}(z)$ which is connected in parallel with the secondary path to model $S(z)$. The error signal of the secondary path modelling process is

$$e'(n) = e(n) - \hat{v}'(n) \tag{7.27}$$

where $\hat{v}'(n) = \hat{s}(n)\, v(n)$ is the output of the modelling filter $\hat{S}(z)$. The residual error $e(n)$ now becomes:

$$e(n) = d(n) - y'(n) - v'(n) \tag{7.28}$$

where

$$y'(n) = s(n)y(n)$$

$$v'(n) = s(n)v(n) \tag{7.29}$$

The updating equation of the estimated secondary path vector can be expressed as

$$\hat{\mathbf{s}}(n+1) = \hat{\mathbf{s}}(n) + \mu' \mathbf{v}(n)e'(n) \tag{7.30}$$

where $\mathbf{v}(n)=[v(n) \;\; v(n-1) \;\; \cdots \;\; v(n-L+1)]^T$ is the buffered random noise input.

It is generally known that the auxiliary random noise technique is superior to the overall modelling technique in terms of independence between the primary disturbance attenuation and the on-line secondary path modelling processes, speed to response to changes in primary disturbance and secondary path, convergence rates of both AVC controller and secondary path modelling filter and frequency band range of secondary path model [85, 86, 88]. Therefore, only the identification technique using auxiliary random noise will be further studied in later sections.

7.5 FBLMS on-line secondary path identification

In practice, the measured residual error signal usually contains some components uncorrelated with the reference noise $v(n)$, which can cause problems with the on-line identification when using a time-domain filter [79]. The corrupted estimation of $S(z)$ can increase the convergence time of the cancellation filter and result in system instability. The FBLMS algorithm which operates in the frequency domain can solve this problem and substantially improve the robustness of the system identification [92]. The block diagram of the FBLMS algorithm is shown in Figure 7.7.

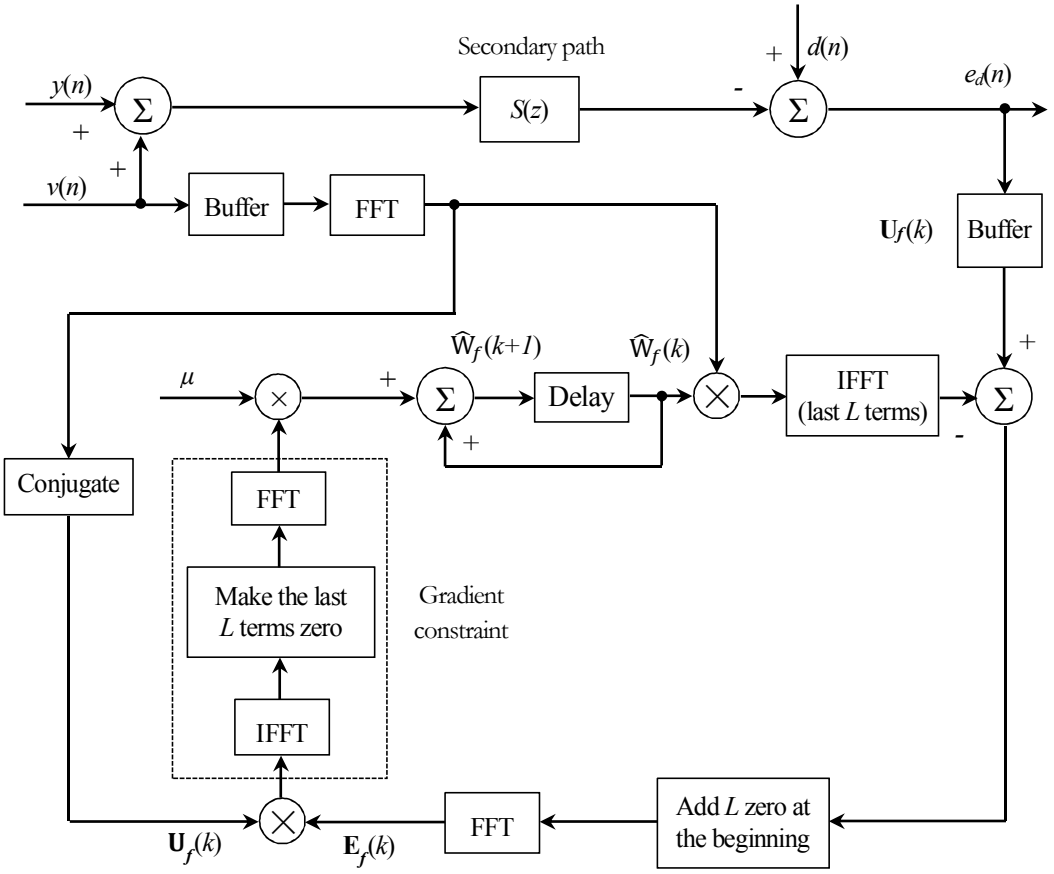

Figure 7.7: Block diagram of the FBLMS algorithm for on-line secondary path identification.

In the FBLMS algorithm, the overlap-save method, which applies the discrete Fourier transform (DFT), is used for efficient computation of linear convolution. It has been found that the use of 50 percent overlap (i.e. the block length equals to the filter weights length) is the most efficient [91].

The time-domain weight vector $\hat{\mathbf{w}}(k)$ with size of L-by-1 is extended to $2L$-by-1 vector $\hat{\mathbf{w}}_e(k)$ by padding an equal size zero vector, and the frequency domain weight $\hat{\mathbf{W}}_f(k)$ is defined as:

$$\hat{\mathbf{W}}_f(k) = FFT[\hat{w}_e(k)\,] = FFT\begin{bmatrix}\hat{\mathbf{w}}(k)\\ \mathbf{0}\end{bmatrix} \tag{7.31}$$

where k denotes the block index. The weight $\hat{\mathbf{W}}_f(k)$ recursion is obtained as:

$$\widehat{\mathrm{W}}_f(k+1) = \widehat{\mathrm{W}}_f(k) + \mu FFT\begin{bmatrix}\rho(k)\\ \mathbf{0}\end{bmatrix}$$

$$\rho(k) = P_{L,0}IFFT[\mathbf{U}_f(k)\mathbf{E}_f(k)] \tag{7.32}$$

where $P_{L,0}$ is a $2L$-by-$2L$ windowing matrix which ensures that the last L terms of the updated weight vector $\widehat{\mathrm{W}}_f(k+1)$ remain zero, $\mathbf{E}_f(k)$ is the frequency domain error signal, $\mathbf{U}_f(k)$ is obtained by taking FFT of the two successive blocks of noise signal $u(n)$ and is expressed as:

$$\mathbf{U}_f(k) = diag\{FFT[u(kL-L),\ldots,u(kL-1),u(k),\ldots,u(kL+L-1)]\} \tag{7.33}$$

where $diag$ donates an L-by-L diagonal matrix.

The convergence rate of the FBLMS algorithm can be improved by using the step-normalization technique, which is achieved by assigning individually normalized step-size parameters to each element of the weight vector $\widehat{\mathrm{W}}_f(k)$. The step-size parameter μ becomes a function of the power spectral density (PSD) of the reference signal. However, it is a function of the PSD of the measured error signal for this application.

$$\mu_i(k) = \frac{\mu_0}{\boldsymbol{P}_i(k)} \tag{7.34}$$

where μ_0 is a constant, $i = 0,1\ldots,2L-1$, k is the block number, $\boldsymbol{P}_i(k)$ are the power estimates of the samples of the filter input in the frequency domain and they can be obtained by using a first order low-pass filter as follows:

$$\boldsymbol{P}_i(k) = \beta\boldsymbol{P}_i(k-1) + (\mathbf{1}-\beta)|\,\mathrm{E}_{\boldsymbol{i}}(k)|^2,\ i = 0,1,\ldots,2L-1 \tag{7.35}$$

where $E_{\boldsymbol{i}}(k)$ is the measured error applied to the i^{th} weight in the FBLMS algorithm, β is a forgetting factor chosen in the range $0 < \beta < 1$, and close to 1.

By using the step-normalization, a lower adaption rate is applied to the frequency bins containing signal power relating to the uncancelled seat vibration components and the corruption of the estimate $\hat{S}(z)$ is reduced.

7.6 Simulation of on-line secondary path identification

In order to validate the effectiveness of on-line secondary path identifications using the FBLMS method, a simulation study has been conducted. A simplified linear model of the secondary path dynamic of the active seat with a dummy described in Chapter 5 is used for the simulation. The linear model plant $S(z)$ is represented by a second-order continuous transfer function $S(s)$ with 0.001 second sampling time interval:

$$S(s) = \frac{\lambda\omega_n^2}{s^2 + 2\xi\omega_n s + \omega_n^2} \tag{7.36}$$

with gain λ=1.2, damping ratio ξ=0.2 and natural frequency ω_n=157 rad/s.

For the on-line identification of the known plant, an additional 10 Hz disturbance is applied to the residual error signal to represent un-cancelled vibration on the target point. An over-length filter (256 taps) is deliberately used in both the conventional LMS (Time-domain) and the FBLMS (Frequency-domain) identification techniques in order to show the effect of the 10 Hz disturbance upon on-line identifications.

The identification results of the known plant obtained by using off-line (i.e. only the identification white noise is acting on the plant) methods were presented firstly for comparison. Figure 7.8 shows the identification results in the form of the filter impulse response. It can be seen that very close estimates are obtained for both the off-line Time-domain and Frequency-domain identification methods.

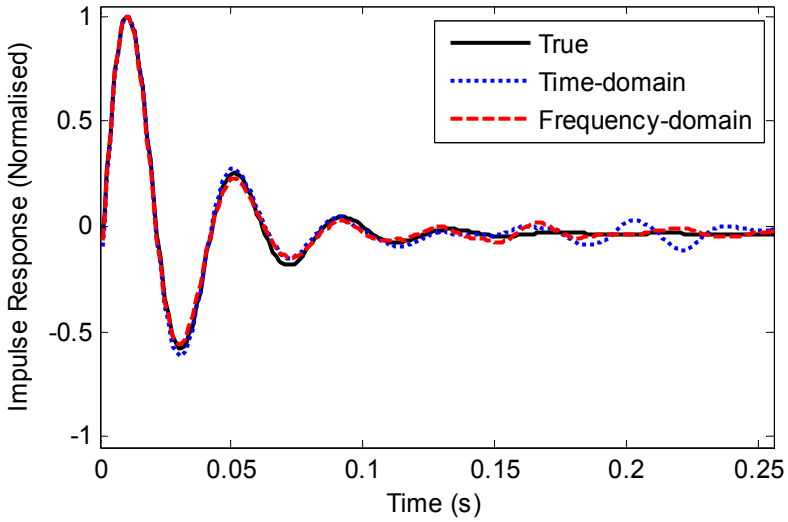

Figure 7.8: Off-line identification results using Time-domain and Frequency-domain LMS.

Figure 7.9 shows the off-line identification results in the form of magnitude and phase responses. As can be seen, good agreement is achieved between the true and the estimated responses for both the Time-domain and Frequency-domain methods. As previously mentioned, the difference in phase between the true and estimated secondary path transfer functions must not be greater than 90^{o} in order to guarantee the stability of the FXLMS algorithm. As shown in the phase responses, the phase error for both methods is sufficiently small in the whole frequency range to ensure the stability of the cancellation filter.

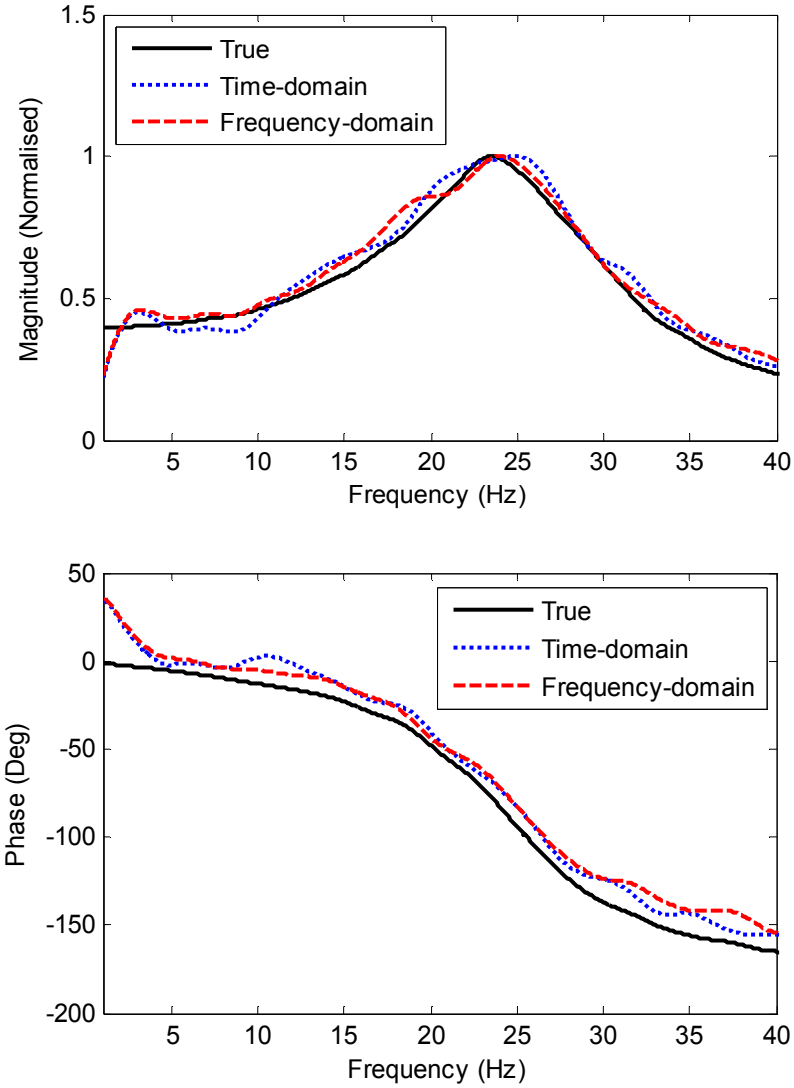

Figure 7.9: Off-line identification results using Time-domain and Frequency-domain LMS.

Figure 7.10 shows the on-line identification results in the form of the filter impulse response. In this case, it is clear that the Frequency-domain identification method generated a more accurate estimate of the known plant. The Time-domain identification result is significantly affected by the added 10 Hz disturbance. The effect of the extra disturbance can be seen more clearly from the magnitude and phase responses in Figure 7.11.

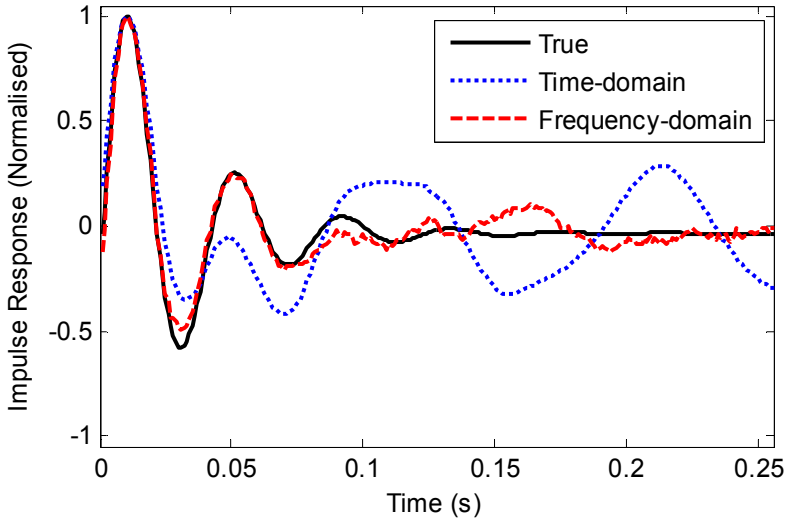

Figure 7.10: On-line identification results using Time-domain and Frequency-domain LMS.

Figure 7.11 shows the on-line identification results in the form of magnitude and phase responses. It is seen that the Frequency-domain result remains generally good across the frequency range, and the phase error is well within the stability criterion. By contrast, the estimated result achieved using the Time-domain method is greatly corrupted by the 10 Hz disturbance. Poor accuracy in the magnitude response is seen, and the phase error at some frequencies is considerably large.

For the application of the active seat, the measured residual error signal would contain substantial disturbance components uncorrelated with the identification noise, which would be derived from external inputs and from un-cancelled vibration on the target point. The use of the FBLMS identification technique operating in the frequency-domain should substantially improve the robustness and stability of the cancellation system.

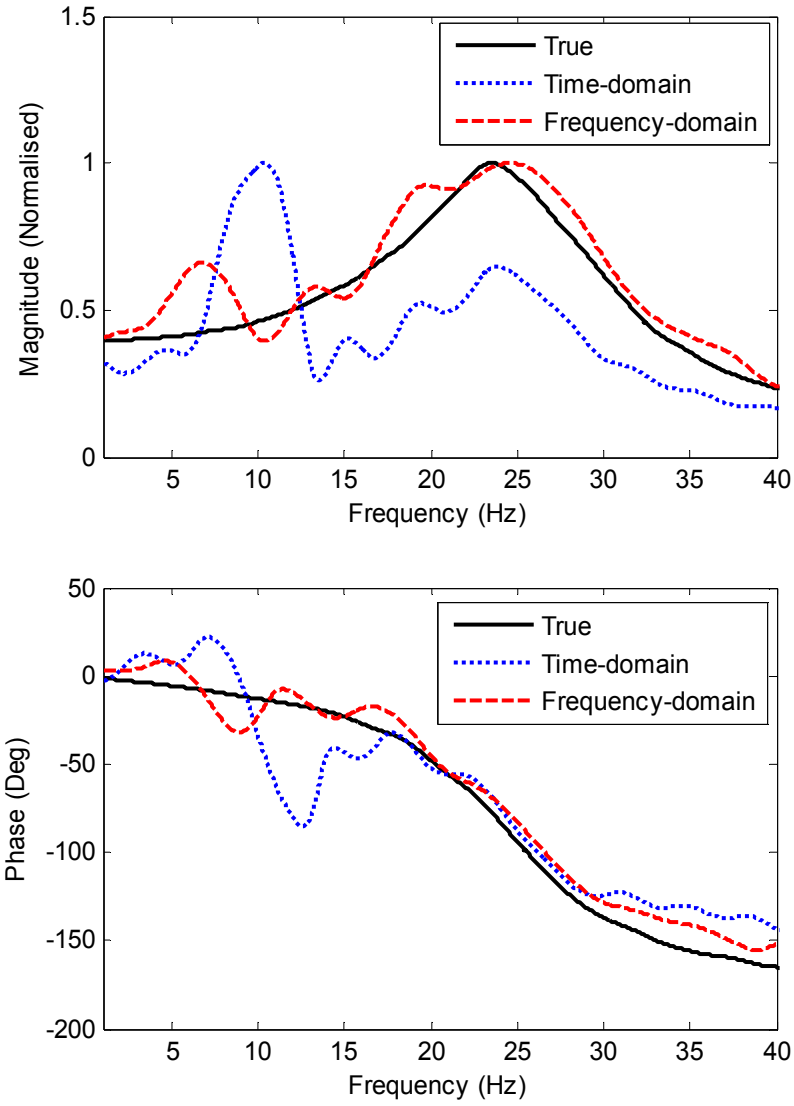

Figure 7.11: On-line identification results using Time-domain and Frequency-domain LMS.

7.7 Active narrow-band vibration cancellation

Vibration for vehicle seats can be generally divided into broad-band and narrow-band according to the energy distribution across the frequency band. Broad-band vibration on vehicle seats can be introduced by rough road profiles, while narrowband vibration can result from periodic engine vibration and aerodynamics. For the case of broad-band vibration cancellation, a vibration sensor which is capable of providing a broad-band reference signal is needed. Also, the filter length must be sufficiently long to adequately model the impulse response of the system dynamics. For narrow-band cancellation, the

reference sensor can be replaced by other non-vibration sensors, such as a tachometer or an optical sensor. In this case, the cancellation filter will aim to reduce the primary spectral components within a narrow-band centred about the measured reference frequency. The filter length must be sufficiently long to model the majority of one period of the slowest mode within the reference signal [55]. In this section, narrow-band vibration cancellation methods are studied.

7.7.1 Single-frequency cancellation using the FXLMS algorithm

For many applications, the primary vibration is produced by rotating or reciprocating machines and is normally periodic. The fundamental frequency that requires cancellation can be generated by detecting the vibration using a tachometer or optical sensor. The block diagram of a single-frequency cancellation system using the FXLMS algorithm is illustrated in Figure 7.12.

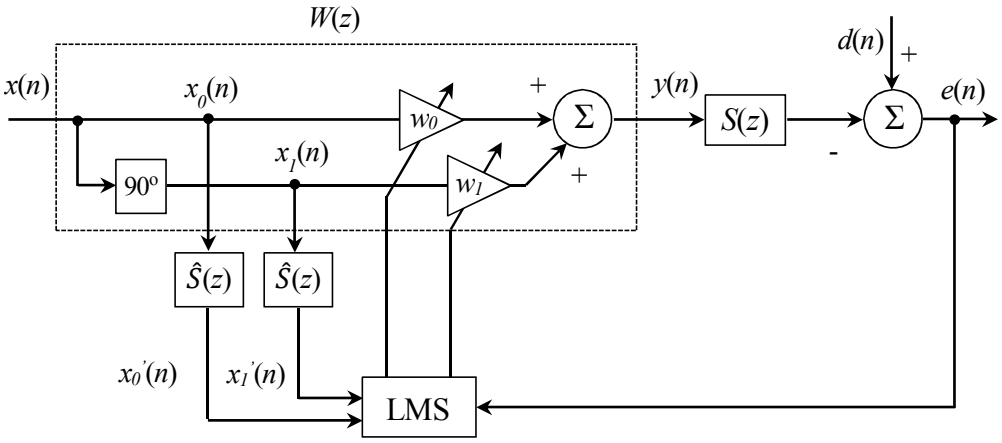

Figure 7.12: Single-frequency cancellation system using the FXLMS algorithm.

As it is shown, two synthesised orthogonal components $x_0(n)$ and $x_1(n)$ are used for the reference signals, which contain only the frequencies that require cancellation. The reference signals can be defined by the equations:

$$x_0(n) = A_0 \sin(\omega_e n \Delta t) \tag{7.37}$$

$$x_1(n) = A_1 \cos(\omega_e n \Delta t) \tag{7.38}$$

where A_0 and A_1 are the amplitudes, ω_e is the estimated vibration frequency which require cancellation, and Δt is the fixed sampling interval. In this case, the LMS algorithm takes the form of an adaptive notch filter.

Two adaptive weights are required for every frequency present in the reference signals for cancellation. The weights are iterated by the equations:

$$w_0(n+1) = w_0(n) - \mu x_0'(n) e(n) \tag{7.39}$$

$$w_1(n+1) = w_1(n) - \mu x_1'(n) e(n) \tag{7.40}$$

where $x_0'(n)$ and $x_1'(n)$ are the reference signals filtered by the secondary path estimate $\hat{S}(z)$, μ is the convergence rate (a positive real constant) of the algorithm, and $e(n)$ is the error signal.

Assuming that the primary signal $d(n)$ is given by

$$d(n) = A_d \cos(\omega_0 n \Delta t + \emptyset_d) \tag{7.41}$$

and the estimated secondary path $\hat{S}(z)$ is equal to the actual path $S(z)$, the error signal at the frequency ω_0 can be expressed as

$$e(n) = A_d \cos(\omega_0 n \Delta t + \emptyset_d) - A A_w A_s \cos(\omega_0 n \Delta t + \emptyset_w + \emptyset_s) \tag{7.42}$$

where A_w and $\emptyset_w$ are the amplitude and phase of the adaptive filter at ω_0, A_s and $\emptyset_s$ are the amplitude and phase of the secondary path $S(z)$, respectively.

Therefore, the required controller magnitude and phase response can be expressed as

$$A_w = \frac{A_d}{A A_s} \tag{7.43}$$

and

$$\emptyset_w = \emptyset_d - \emptyset_s \tag{7.44}$$

Thus, the function of the adaptive filter $W(z)$ is to compensate the amplitude and phase difference between the primary signal and the cancelling signal.

It is shown in [79] that the equivalent close-loop transfer function between the primary input $d(n)$ and the error output $e(n)$ is

$$H(z) = \frac{1}{1 + \frac{S(z)Y(z)}{E(z)}}$$

$$= \frac{z^2 - 2z\cos(\omega_0 \Delta t) + 1}{z^2 - 2z\cos(\omega_0 \Delta t) + 1 + \beta S(z)[z\cos(\omega_0 \Delta t - \emptyset_s) - \cos\emptyset_s]} \tag{7.45}$$

where

$$\beta = \mu A^2 A_s \tag{7.46}$$

and $Y(z)$ and $E(z)$ are the z transform of the cancelling signal $y(n)$ and error signal $e(n)$, respectively.

For the secondary path $S(z)$=1, thus, A_s=1 and $\emptyset_s$=0. The magnitude and phase response of the transfer function $H(z)$ for μ=0.2 and μ=0.02 is shown in Figure 7.13.

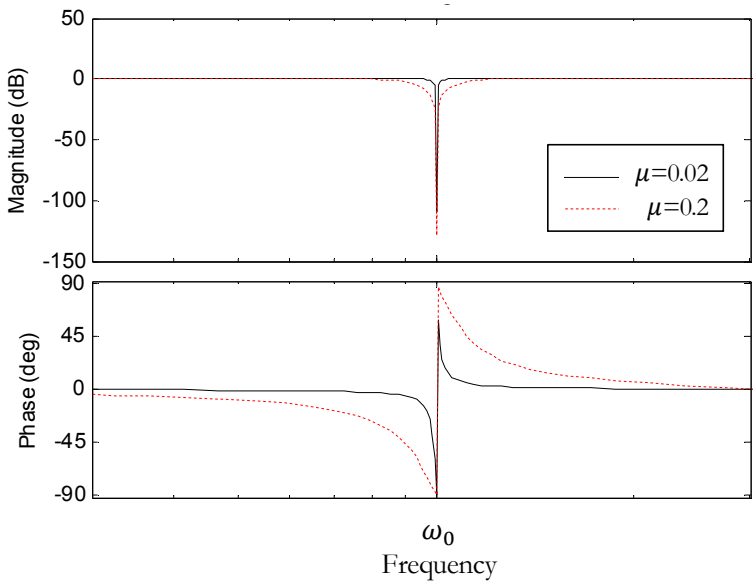

Figure 7.13: Magnitude and phase response of transfer function $H(z)$.

It can be seen that the responses are of the form of a notch filter with the notch frequency equal to ω_0. The value of μ determinates the width of the notch. The notch becomes sharper when μ decreases.

For some applications, the adaptive filter may be required to cancel a particular frequency but preserve others contained within the same signal. A large value of μ is desired to achieve good cancellation of the target frequency, and also respond to system changes rapidly. However, significant attenuation of other frequency components will occur due to the big notch width with large value of μ. Therefore, the selection of the convergence rate μ is a trade-off between tracking performance and filter notch width.

7.7.2 Multiple harmonics cancellation using the FXLMS algorithm

In practice, the periodic vibration usually contains tones at the fundamental frequency plus several harmonics. The single-frequency FXLMS algorithm can be extended to cancel multiple frequencies by adding additional controllers to each harmonic. For the case to cancel M harmonics in a periodic vibration, M two-weight adaptive filters can be applied in parallel. Figure 7.14 shows the configuration of parallel narrow-band AVC systems.

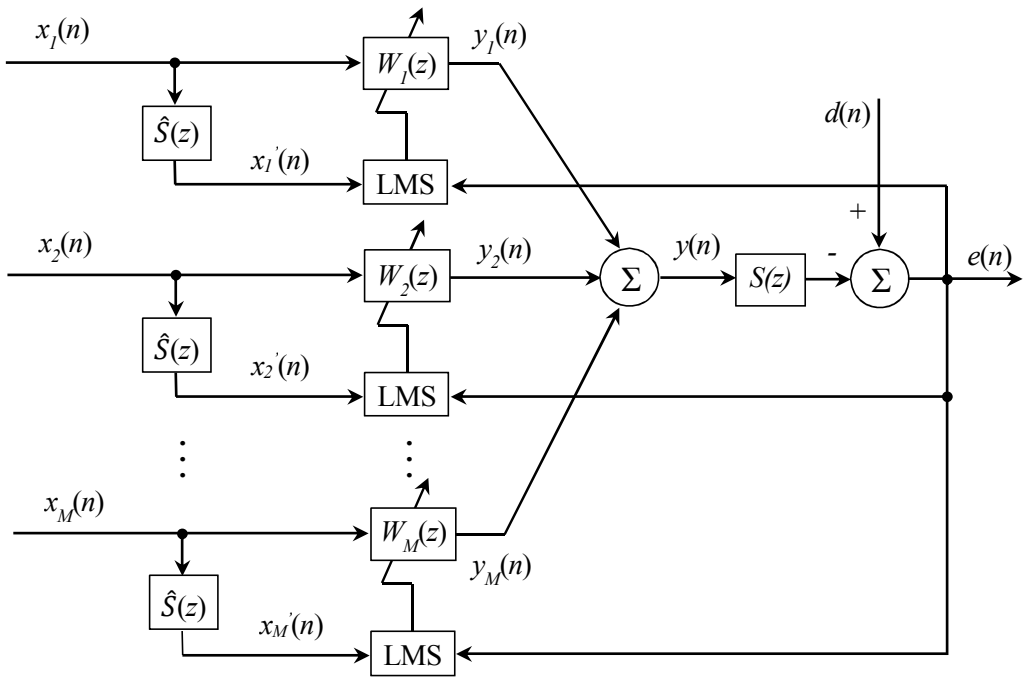

Figure 7.14: Parallel narrow-band AVC system for multiple frequencies cancellation.

The cancelling signal now is the sum of the M adaptive filter outputs as given by:

$$y(n) = \sum_{m=1}^{M} y_m(n)$$

$$y_m(n) = w_{m,0}(n)x_{m,0}'(n) + w_{m,1}(n)x_{m,1}'(n),\ m = 1,2,\dots,M \quad (7.47)$$

where $x_{m,0}'(n)$ and $x_{m,1}'(n)$ are the filtered reference signals with 90 degrees phase shift.

The filter weights can be updated by using the FXLMS algorithm

$$w_{m,0}(n+1) = w_{m,0}(n) + \mu x_{m,0}'(n)e(n),\ m = 1,2,\dots,M \quad (7.48)$$

$$w_{m,1}(n+1) = w_{m,0}(n) + \mu x_{m,1}'(n)e(n),\ m = 1,2,\dots,M \quad (7.49)$$

where m is the channel index number.

7.8 Simulation of active narrow-band vibration cancellation

In the simulation study, a simplified linear model of the primary path of the active seat with a dummy described in Chapter 5 is used. The linear model plant $P(z)$ is represented by a second-order continuous transfer function $P(s)$ with 0.001 second sampling time interval:

$$P(s) = \frac{\lambda\omega_n^2}{s^2 + 2\xi\omega_n s + \omega_n^2} \quad (7.50)$$

with gain λ=1, damping ratio ξ=0.35 and natural frequency ω_n=75 rad/s. The secondary path dynamic is represented by a similar model described in Section 7.6.

The narrow-band FXLMS algorithm was applied to the simulated system to cancel vibration signals containing a single frequency and multiple harmonic frequencies, respectively. The cancellation results obtained using the FBLMS on-line identification technique are compared with those obtained using the FBLMS off-line identification technique.

7.8.1 Simulation of single-frequency cancellation

For the single-frequency cancellation, the simulated system was configured to cancel a 6 Hz sinusoidal signal applied on the primary path. A filter length of 256 was used for both the off-line and on-line FBLMS secondary path identification. The on-line identification white noise variance was 1×10^{-4} and the convergence rate was set at 0.1 to give a fast response.

Figure 7.15 shows the single-frequency cancellation results in the time domain. As can be seen, good cancellation was achieved for both the off-line and on-line cases after a short adaptive period. The convergence rate of the cancellation filter is 2×10^{-4} for both cases, but the adaptive period of the on-line case is longer than the off-line case because of the secondary path identification process. This difference can be seen more clearly in the comparison of the tap weights of the cancellation filter in Figure 7.16.

Figure 7.17 shows the comparison of the power spectra of the error signals after cancellation using both the off-line and on-line identification techniques. A good level of cancellation can be seen in both cases, but inevitably the on-line identification adds a low-level noise to the system and reduces the overall cancellation effect.

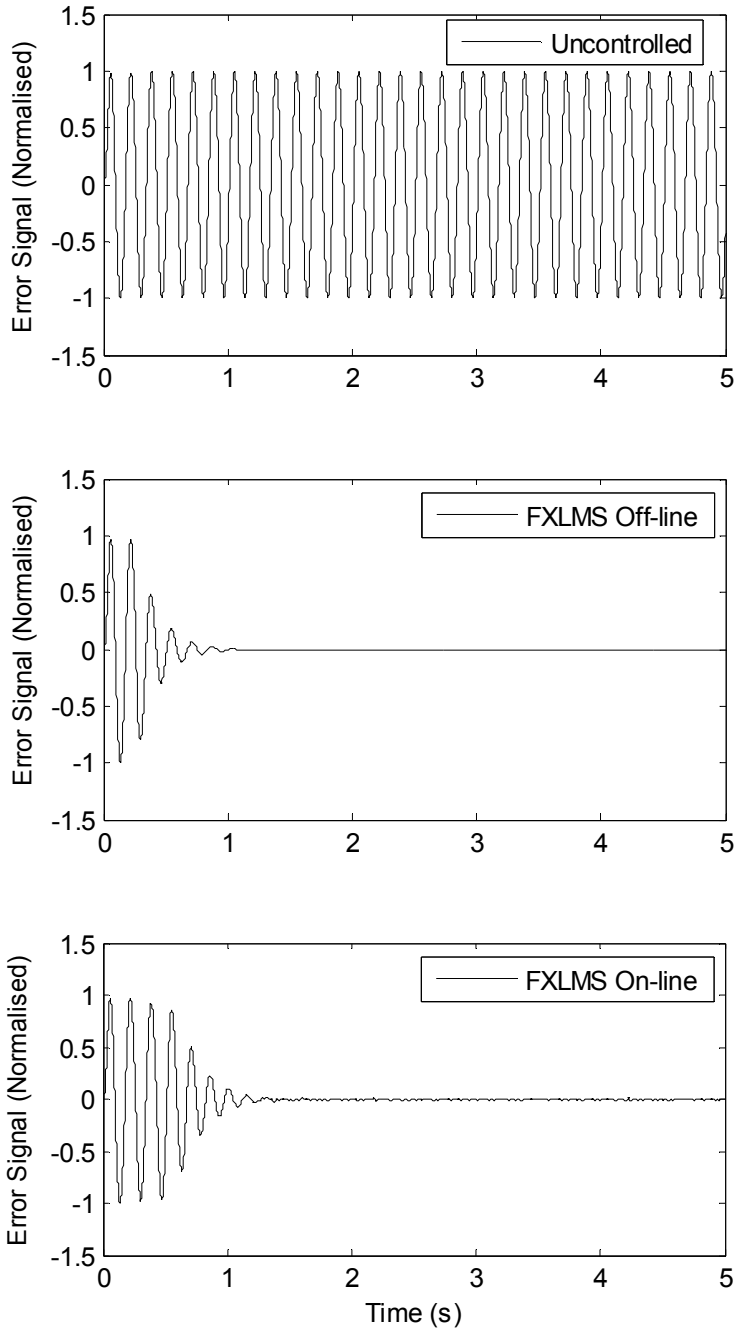

Figure 7.15: Single-frequency cancellation results by using FXLMS algorithm with FBLMS off-line and on-line secondary path identification.

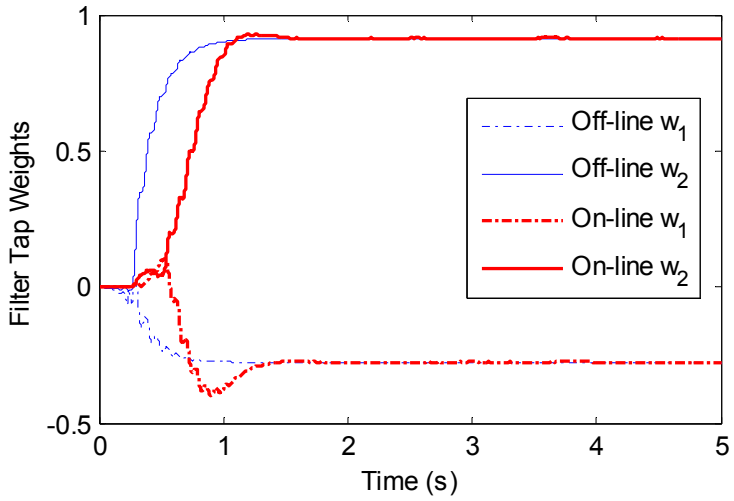

Figure 7.16: Comparison of the off-line and on-line tap weight trajectories of the cancellation filter.

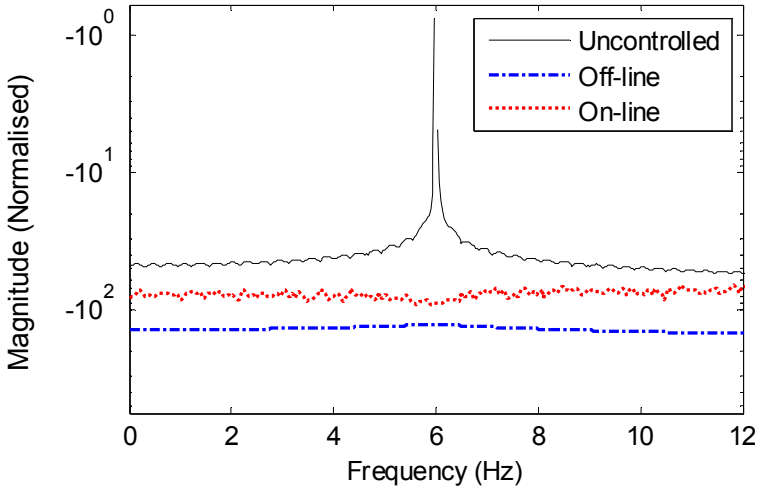

Figure 7.17: Comparison of the power spectra of the error signals after cancellation.

7.8.2 Simulation of multiple harmonics cancellation

As mentioned previously the periodic vibration usually contains tones at the fundamental frequency plus several harmonics in real applications. In order to validate the effectiveness of the FXLMS algorithm for multiple harmonics cancellation, a vibration signal containing three frequencies (the fundamental frequency at 4 Hz, the

second and third harmonics at 8 and 12 Hz) was used to excite the system, and the single frequency FXLMS algorithm was extended to cancel each frequency component by adding additional sub-controllers. The amplitudes for the three frequency components are 0.8, 0.6 and 0.4, respectively. Same as for the single-frequency cancellation, a filter length of 256 was used for both the off-line and on-line identification filter. The on-line identification white noise variance was 1×10^{-4} and the convergence rates for each adaptive filter are listed in Table 7.1.

Table 7.1: Convergence rates used for the adaptive filters in the multiple harmonics cancellation simulation.

Off-line cancellation		**On-line cancellation**	
Adaptive filter	Convergence rate	Adaptive filter	Convergence rate
4 Hz filter	2×10^{-4}	4 Hz filter	1.3×10^{-4}
8 Hz filter	1×10^{-4}	8 Hz filter	8×10^{-5}
12 Hz filter	3×10^{-5}	12 Hz filter	5×10^{-5}
		On-line identification filter	1×10^{-1}

Figure 7.18 shows the comparison of the multiple harmonics cancellation results in the time domain. It can be seen again, the primary vibration was reduced to nearly zero level for both the off-line and on-line cases after a short adaptive period. As shown in Table 7.1, different convergence rates were used for the three sub-controllers to guarantee an overall stable performance. The adaptive period of the multiple harmonics cancellation thus depended on the smallest convergence rate. Again, an additional on-line secondary path identification time was added for the on-line case.

Figure 7.19 shows the tap weight trajectories comparison between the off-line and on-line cancellation filter of each frequency. It is observed that all the filter weights successfully converged to near constant stable values for both the off-line and on-line cases. The differences in the adaptive period between the two cases are clearly seen in these plots.

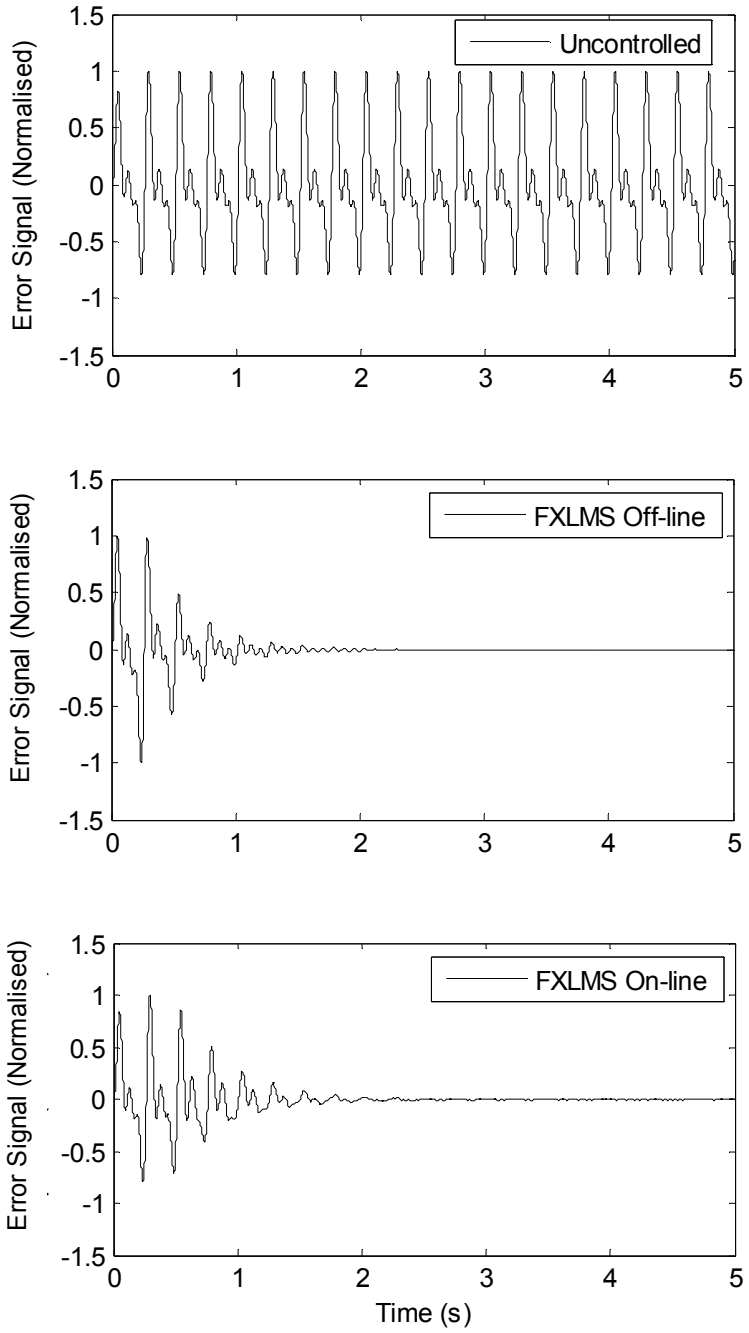

Figure 7.18: Multiple harmonics cancellation results by using FXLMS algorithm with FBLMS off-line and on-line secondary path identification.

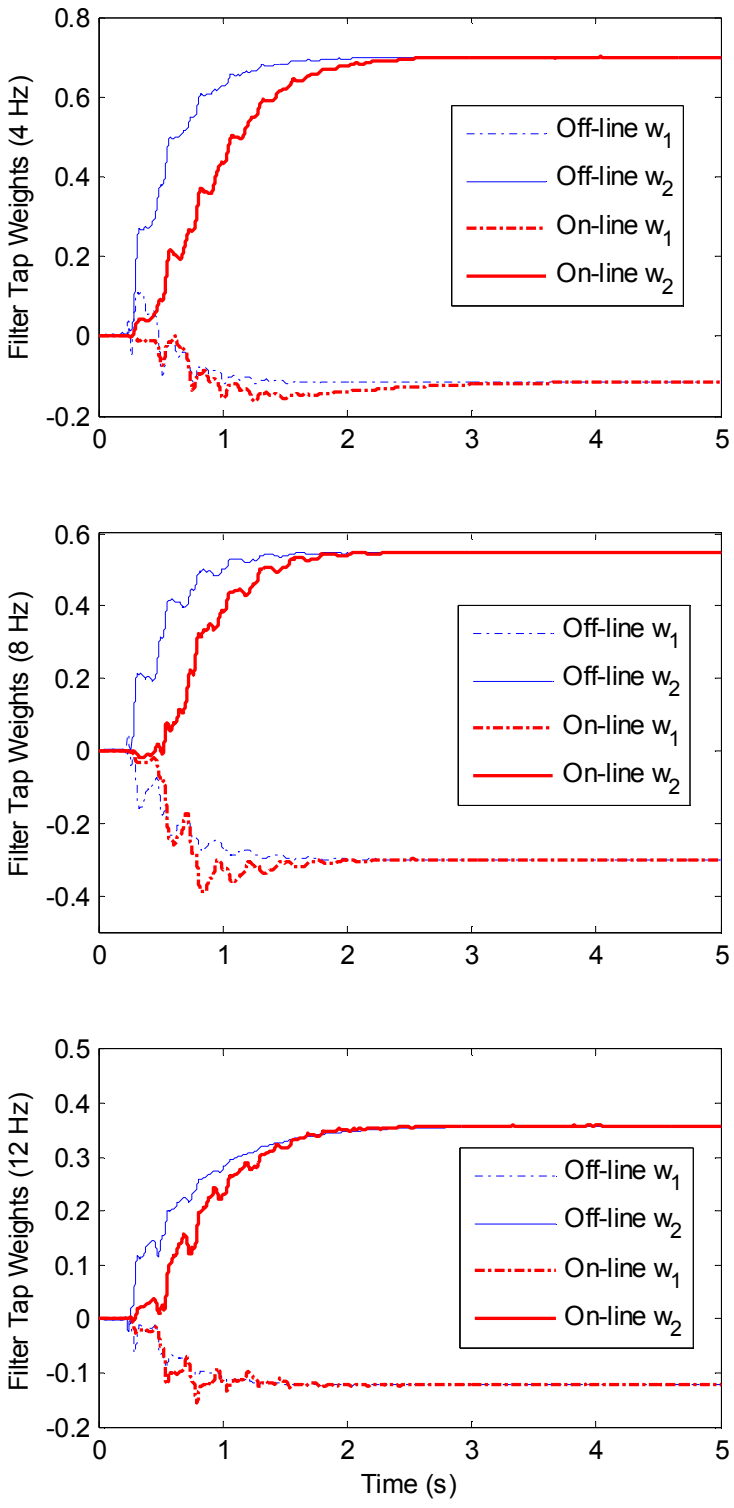

Figure 7.19: Comparison of the off-line and on-line tap weight trajectories of the cancellation filter for each frequency.

Figure 7.20 shows the comparison of the power spectra of the error signals after cancellation. In both the off-line and on-line cases, good levels of cancellation for all the three frequencies were achieved. Same as the single-frequency cancellation, the multiple harmonics cancellation with on-line identification inevitably added a low-level noise to the system and reduces the overall cancellation effect.

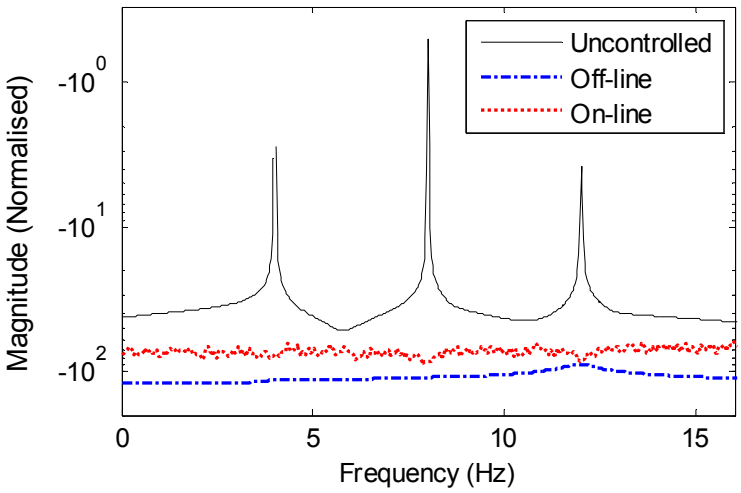

Figure 7.20: Comparison of the power spectra of the error signals after cancellation.

It can be concluded that multiple harmonic frequencies can be efficiently cancelled by using parallel adaptive notch filter based on the FXLMS algorithm. The accurate estimation of the secondary path dynamic obtained by the FBLMS off-line identification technique can enable an excellent cancellation performance for a time-invariant system. Nearly good level of cancellation can also be achieved using the FBLMS on-line identification technique after a slightly longer adaptive period. Different convergence rates can be used for different sub-controllers to guarantee an overall stable cancellation performance.

7.9 Conclusions

This chapter presents the derivation of the FXLMS algorithm. Several secondary path identification techniques have been introduced and the FBLMS algorithm operating in the frequency domain has been investigated via simulation examples. In addition, the

FXLMS algorithm with the FBLMS system identification technique has been evaluated through a simulated system for narrow-band vibration cancellation. The effectiveness of this combination has been proved and thus this method was applied in the experimental studies described in Chapter 8.

Chapter 8

Experimental Studies: Adaptive Control Tests

In this chapter, the vibration cancellation performance of the active seat using adaptive control methods is investigated. The combination of the FXLMS algorithm with the FBLMS system identification technique described in chapter 7 was applied to the experimental rig. Initially, the system performance was measured by cancelling periodic vibrations containing single and multiple frequencies. Then, transient switching frequency cancellation tests were carried out to evaluate the speed of response and the robustness of the adaptive control system. In addition, the stability of the control system was further examined by cancelling vibration signals accompanied by low-frequency, large amplitude disturbances.

8.1 Experimental setup and the secondary path

The adaptive control tests were conducted on the experimental rig described in Chapter 6. The active seat was rigidly mounted on the MAST platform. As previously stated, a vibration test dummy was used as a seated human body substitute in order to ensure an improved consistency in behaviour and avoid safety and ethical issues. In these tests, a total of four piezoresistive accelerometers were used to measure the acceleration (all in the vertical direction) and provide feedback signals. The mounting locations of the accelerometers were: the MAST platform (i.e. seat base), the middle of the seat pan, the dummy pelvis and the dummy shoulder, as shown in Figure 8.1.

Two different secondary paths were selected for the experimental tests:

1. Secondary path from the MAST to the seat pan;

2. Secondary path from the MAST to the dummy shoulder.

For the secondary path from the MAST to the seat pan, the residual vibration on the seat pan was selected as the error signal and the secondary path represents the dynamics from the control output to the measured residual acceleration. This includes an antialiasing filter, a D/A converter, a A/D converter, a power amplifier, and the actuator and error accelerometer dynamics. In this case, the vibration on the seat pan was set as the target to be reduced. Also, the vibration on the dummy pelvis and shoulder was measured and evaluated. Similarly, for the secondary path from the MAST to the dummy shoulder, the residual vibration on the dummy shoulder was selected as the error signal. The secondary path now also includes the dummy dynamics. In this case, the control aim was to minimise the vibration on the dummy shoulder.

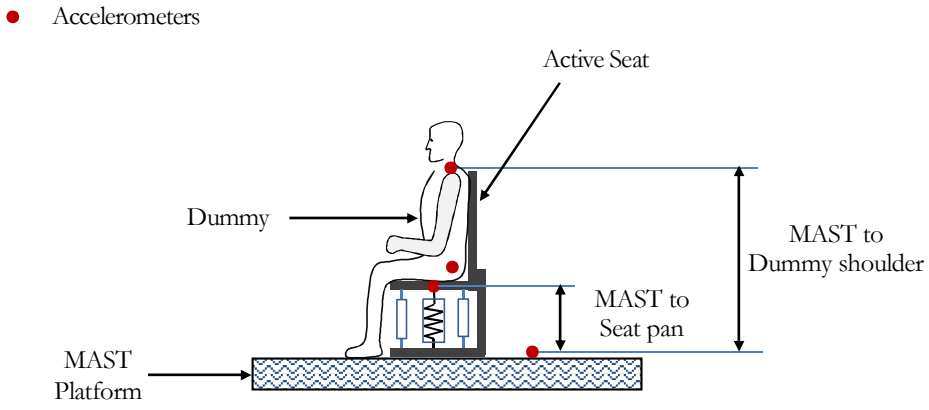

.

Figure 8.1: Accelerometer mounting locations and the two different secondary paths.

8.2 Single frequency cancellation

The performance of the active system was initially measured by cancelling a single frequency vibration. A 6 Hz disturbance with peak input acceleration approximately 0.1 g was applied to the system by the MAST platform, and the vibration cancellation results using the FXLMS algorithm with the FBLMS on-line secondary path identification method are compared with those obtained using an off-line identification method on three locations: the seat pan (SP), the dummy pelvis (DP) and the dummy shoulder (DS).

8.2.1 Results for the secondary path 1

In this test, a filter length of 128 was used for both the off-line and on-line secondary path identification. The estimated secondary path dynamic in the form of the filter impulse response is shown in Figure 8.2. It can be seen that good agreement was achieved between the off-line and on-line results. The oscillations in both the impulse responses settle to near zero values after 0.07 seconds, which indicate the filter length is long enough to capture the essential characteristic of the secondary path.

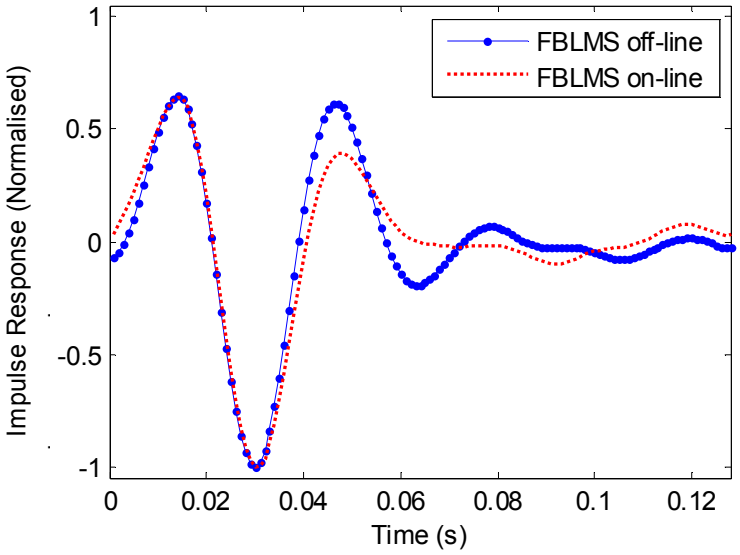

Figure 8.2: FBLMS off-line and on-line identification results for the secondary path 1.

The duration of the single frequency cancellation test was 60 seconds and the controller was switched on at 10 seconds for both the off-line and on-line cases. The convergence rate of the on-line identification filter was set as 8×10^{-3}, and the convergence rates of the cancellation filters were set as 1.6×10^{-3} and 5×10^{-3} for the on-line case and off-line case, respectively. Figure 8.3 shows the comparison of the tap weights (normalised values) of the cancellation filters following the controller switch-on. It is observed that both the off-line and on-line cancellation filters have a stable adaption, and it is clear that the adaptive period of the on-line case is longer than the off-line case because of the secondary path identification process.

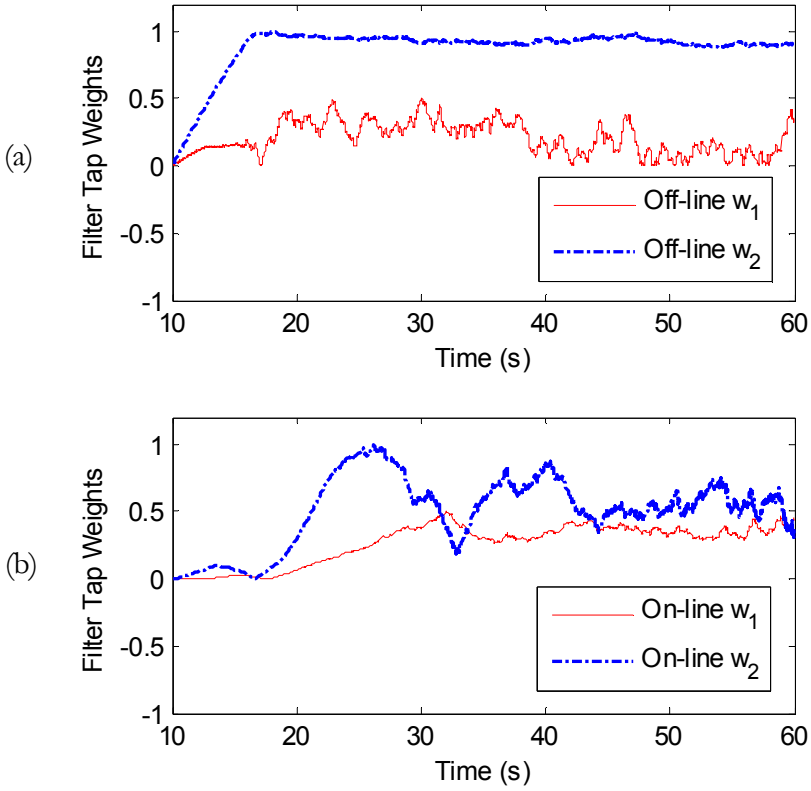

Figure 8.3: Tap weight trajectories of the cancellation filter. (a) Off-line weights; (b) on-line weights.

Figure 8.4 shows the comparison of the single frequency cancellation results on the seat pan. The cancellation results are the pseudo steady-state performance when the controller was fully adapted. It can be seen that around 30 dB reduction is achieved for the off-line case and approximately 20 dB reduction is achieved for the on-line case, at the frequency of 6 Hz. It is clearly seen that the average cancellation level of the on-line case is lower than that of the off-line case because of the white noise introduced by the on-line identification process. A dashed line at -20 dB is placed in Figure 8.4, 8.5 and 8.6 to highlight the cancellation levels.

Figure 8.5 presents a comparison of the cancellation results on the dummy pelvis. It is seen that the vibration level is reduced by more than 15 dB for both cases at the frequency of 6 Hz. Also, it can be observed that the random noise content is generally lower than that on the seat pan due to attenuation through the seat and dummy interface.

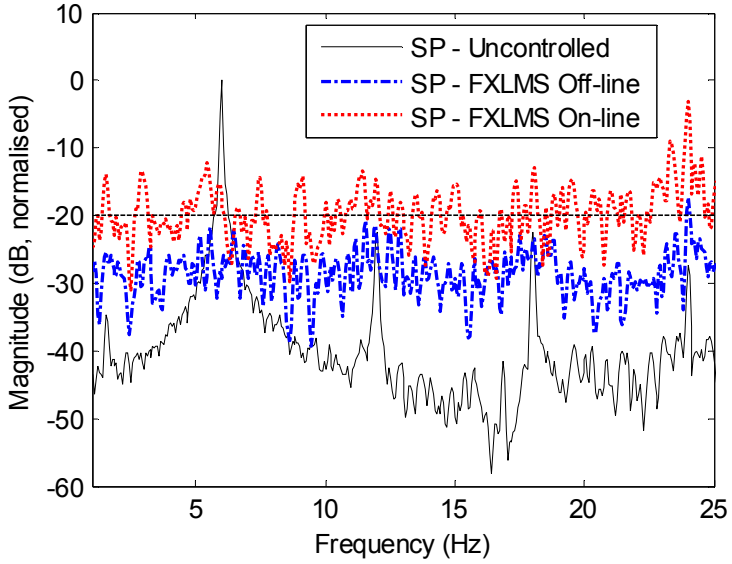

Figure 8.4: Single frequency cancellation results on the seat pan.

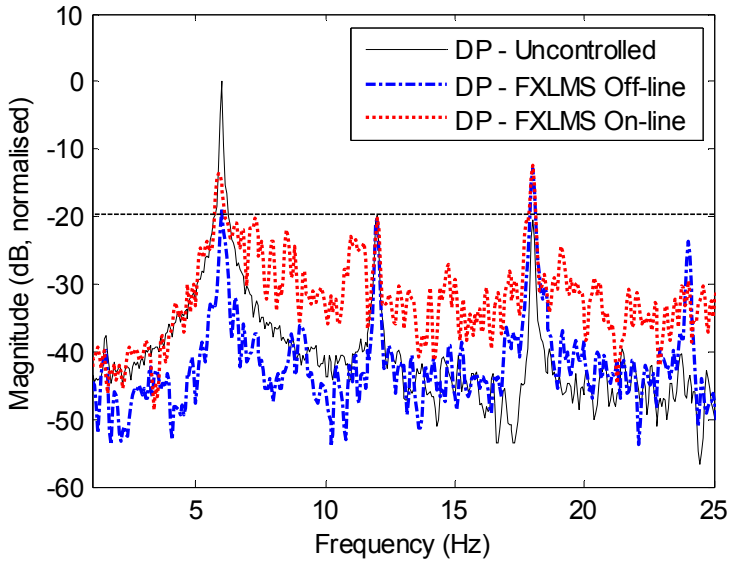

Figure 8.5: Single frequency cancellation results on the dummy pelvis.

Figure 8.6 presents a comparison of the cancellation results on the dummy shoulder. It can be seen that a similar level of vibration reduction to the dummy pelvis is achieved. However, some higher harmonics (the second harmonic 12 Hz, the third harmonic 18 Hz and the forth harmonic 24 Hz) were excited by the active cancellation force.

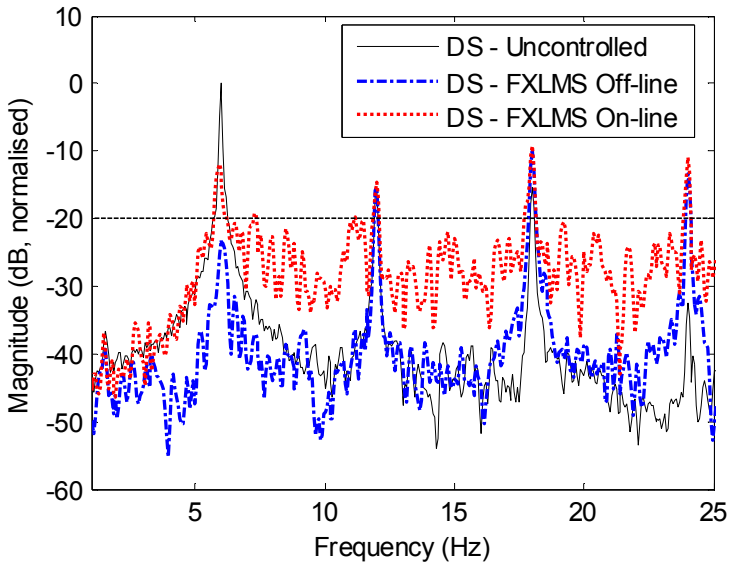

Figure 8.6: Single frequency cancellation results on the dummy shoulder.

8.2.2 Results for the secondary path 2

In this second case, the secondary path now also includes the dummy dynamics, an additional level of complexity. Thus, a filter length of 256 was used for both the off-line and on-line secondary path identification to ensure that the major dynamic characteristic is captured.

Figure 8.7 shows the estimated secondary path in the form of the filter impulse response. A relatively large deviation is seen between the two estimated results, especially in the region from 0 to 0.1 seconds. This difference may result from the system non-linearity. It is also found that there is approximately a 10 sample delay for the on-line identification result.

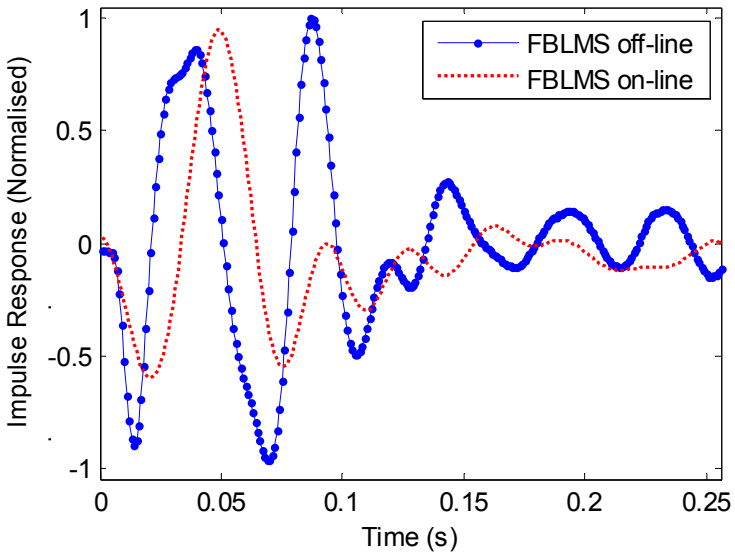

Figure 8.7: FBLMS off-line and on-line identification results for the secondary path 2.

The duration of this test was 60 seconds and the controller was switched on at 10 seconds for both the off-line and on-line cases. The convergence rate of the on-line identification filter was set as 7×10^{-2}, and the convergence rates of the cancellation filters for the on-line case and off-line case were set as 1.2×10^{-3} and 1×10^{-3}, respectively.

Figure 8.8 shows the comparison of the tap weights (normalised values) of the cancellation filters following the controller switch-on. It is seen that both the off-line and on-line cancellation filters have a stable adaption. The weights for the off-line cancellation rapidly settle to near constant values within approximately 2 seconds. However, the on-line cancellation weights took over 10 seconds to reach their stable values.

Figure 8.9 presents a comparison of the single frequency cancellation results on the seat pan for the secondary path 2. The cancellation results are the pseudo steady-state performance when the controller was fully adapted. It can be seen that approximately 20 dB reduction is achieved for the off-line case at the frequency of 6 Hz. The reduction of the on-line controller was slightly affected by the identification noise. A dashed line at -20 dB is placed in Figure 8.9, 8.10 and 8.11 to highlight the cancellation levels.

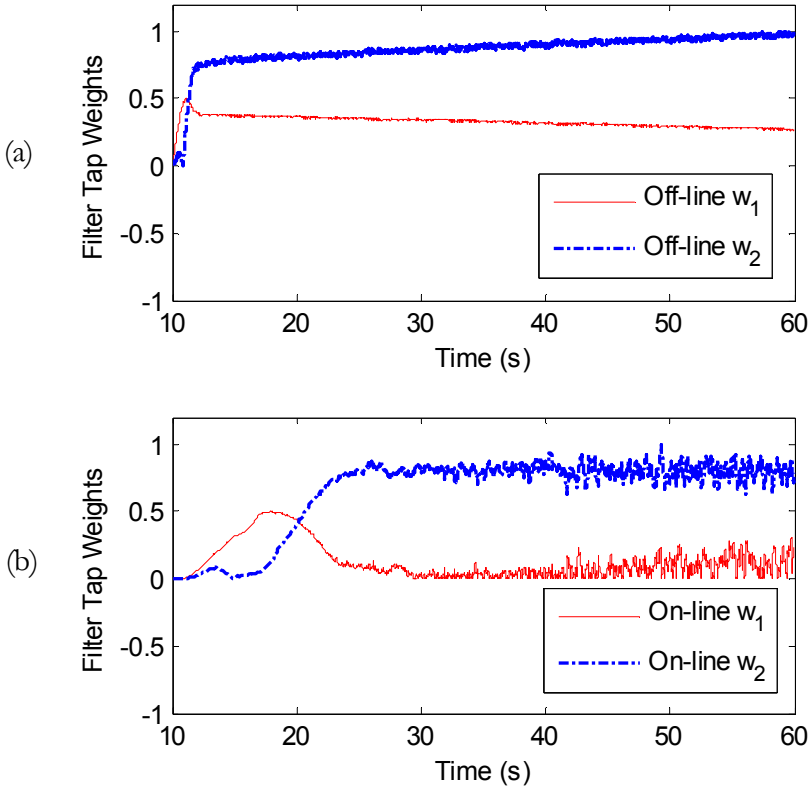

Figure 8.8: Tap weight trajectories of the cancellation filter. (a) Off-line weights; (b) on-line weights.

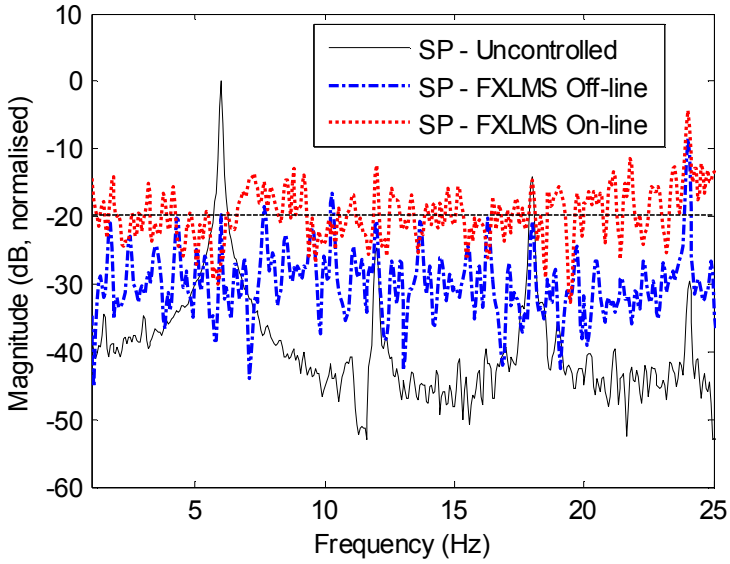

Figure 8.9: Single frequency cancellation results on the seat pan.

Figure 8.10 and 8.11 show a comparison of the cancellation results on the dummy pelvis and shoulder, respectively. It can be seen that substantially larger vibration reduction was achieved on the dummy shoulder by using the secondary path 2 than that achieved by using the secondary path 1 shown in Figure 8.6.

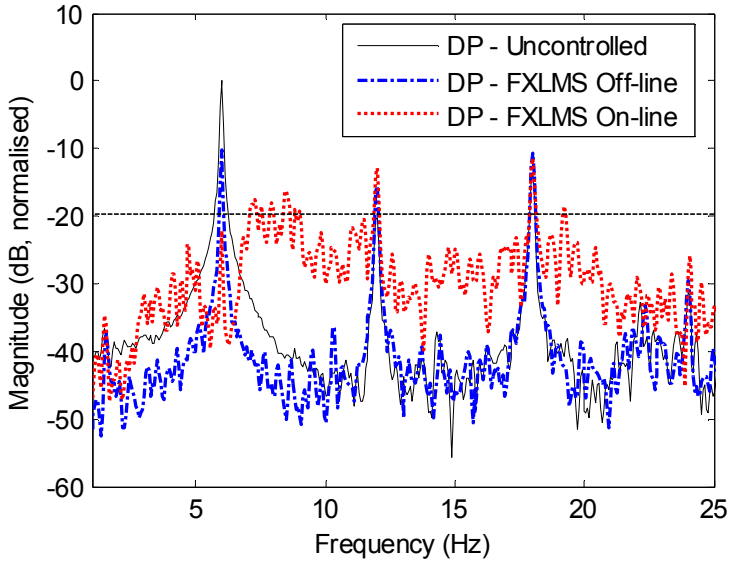

Figure 8.10: Single frequency cancellation results on the dummy pelvis.

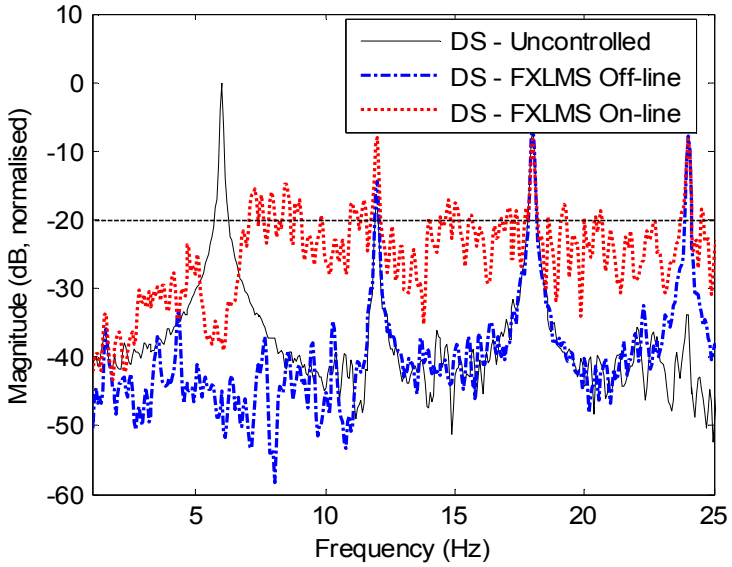

Figure 8.11: Single frequency cancellation results on the dummy shoulder.

8.3 Multiple harmonics cancellation

A vibration signal containing four frequencies was used to excite the system, and the single frequency FXLMS algorithm was extended to cancel each frequency component by adding additional sub-controllers. The selected four frequencies are 4 Hz and 6 Hz and their second harmonics 8 Hz and 12 Hz. The overall peak input acceleration is approximately 0.1 g. In this test, only the secondary path 1- the MAST to the seat pan was selected for the investigation. Again, the cancellation results presented in Figure 8.14, 8.15 and 8.16 are the pseudo steady-state performances when the controllers were fully adapted.

The cancellation results were achieved by using both the off-line and on-line FBLMS secondary path identification method with a filter length of 128. The on-line identification white noise variance was 0.4 and the convergence rates for each adaptive filter are listed in Table 8.1. It can be seen that different convergence rates were used for different sub-controllers to guarantee an overall stable performance.

Table 8.1: Convergence rates used for the adaptive filters in the multiple harmonics cancellation test.

Off-line cancellation		**On-line cancellation**	
Adaptive filter	Convergence rate	Adaptive filter	Convergence rate
4 Hz filter	5×10^{-3}	4 Hz filter	1.6×10^{-3}
6 Hz filter	5×10^{-3}	6 Hz filter	1.4×10^{-3}
8 Hz filter	1×10^{-4}	8 Hz filter	6×10^{-4}
12 Hz filter	2×10^{-4}	12 Hz filter	1.8×10^{-4}
		On-line identification filter	8×10^{-3}

Figure 8.12 shows the filter tap weights of different sub-controllers for the off-line cancellation case. It can be observed that all the weights took less than 10 seconds to reach near constant values. Figure 8.13 shows the filter tap weights of different sub-controllers for the on-line cancellation case. A relatively longer adaptive period is seen when compared with the off-line case.

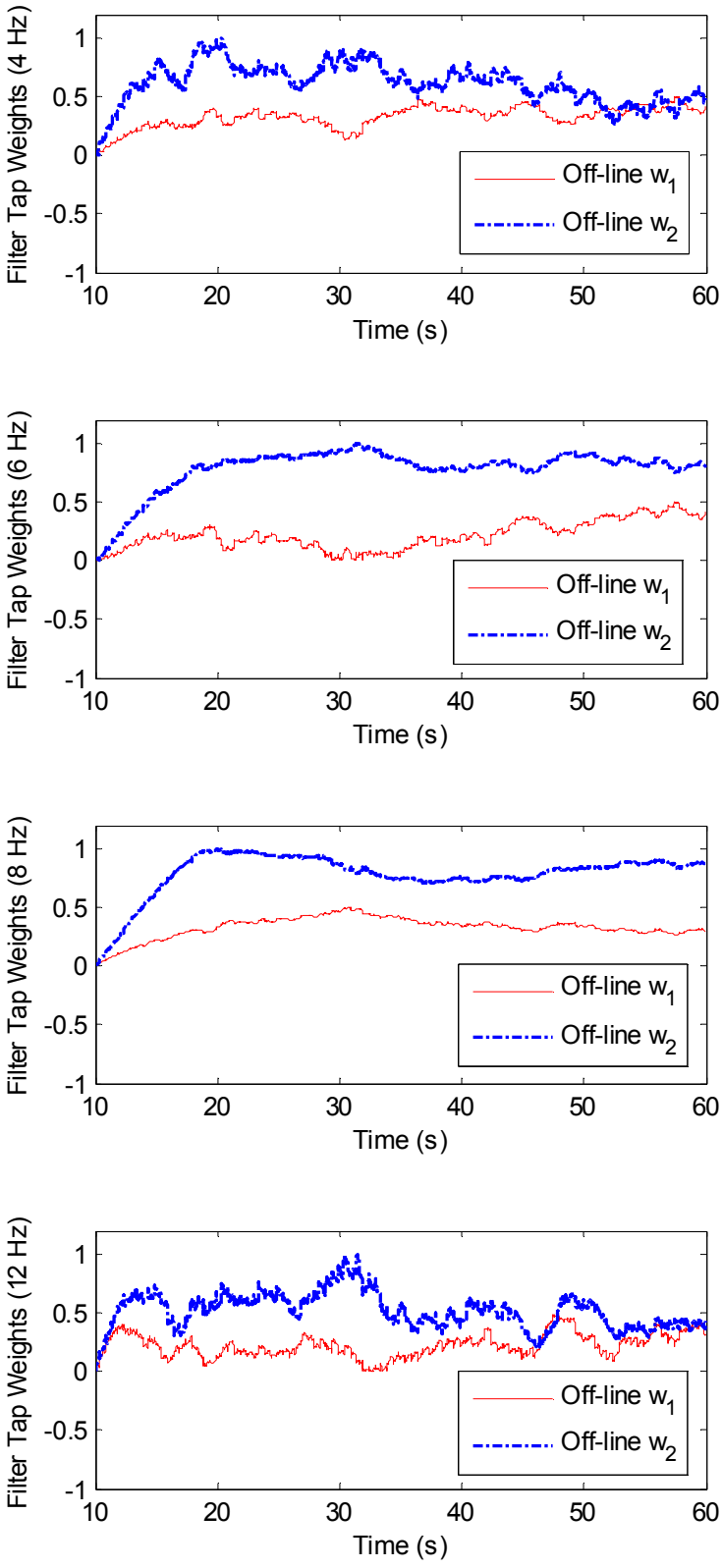

Figure 8.12: Tap weight trajectories of different sub-controllers for the off-line multiple harmonics cancellation test.

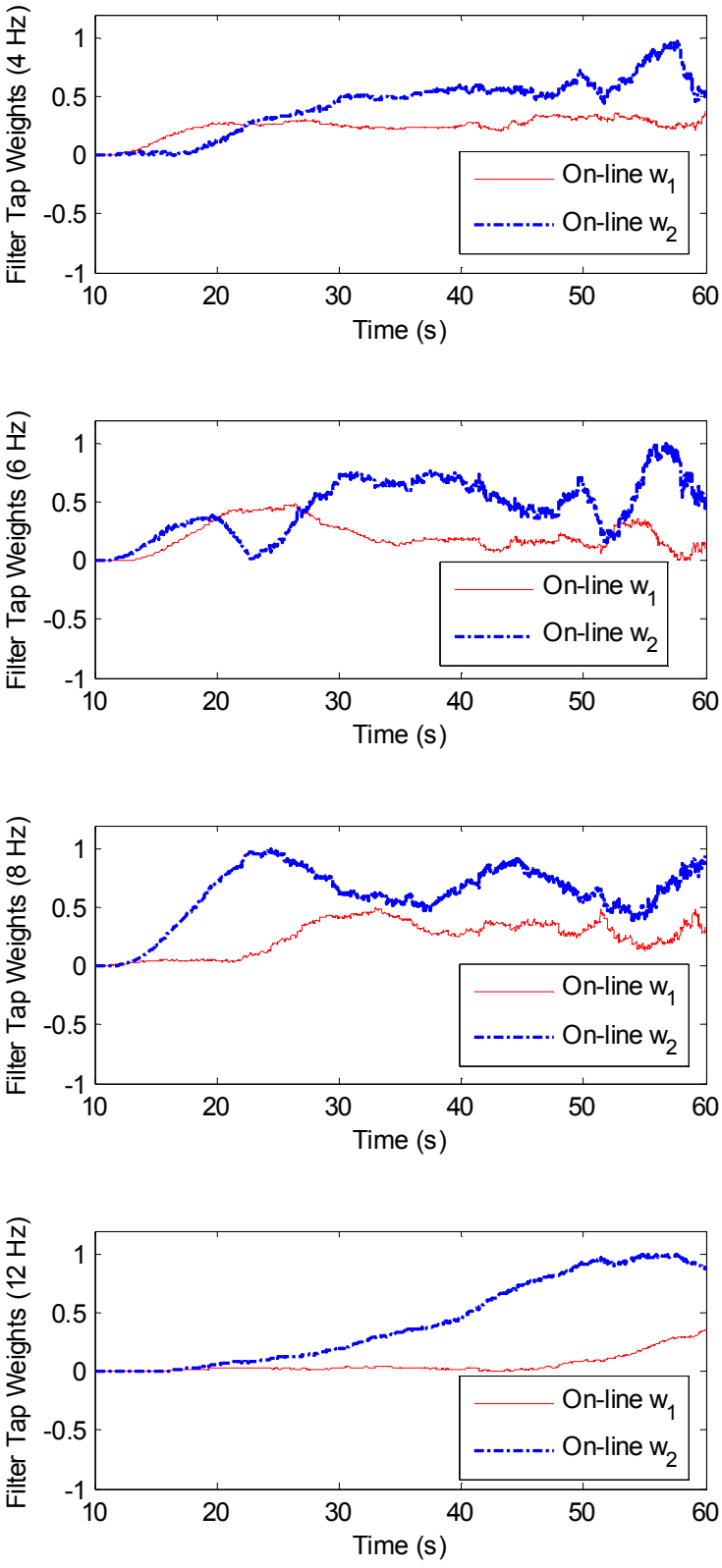

Figure 8.13: Tap weight trajectories of different sub-controllers for the on-line multiple harmonics cancellation test.

Figure 8.14 shows the harmonic cancellation results on the seat pan. It can be seen that the level of vibration cancellation achieved is over 20 dB for all the frequency components for the off-line case, while the reduction for the on-line case is around 20 dB at 4 Hz, 6 Hz and 8 Hz, and 5 dB at 12 Hz. Two dashed lines at -10 dB and -20 dB are placed in Figure 8.14, 8.15 and 8.16 to highlight the cancellation levels.

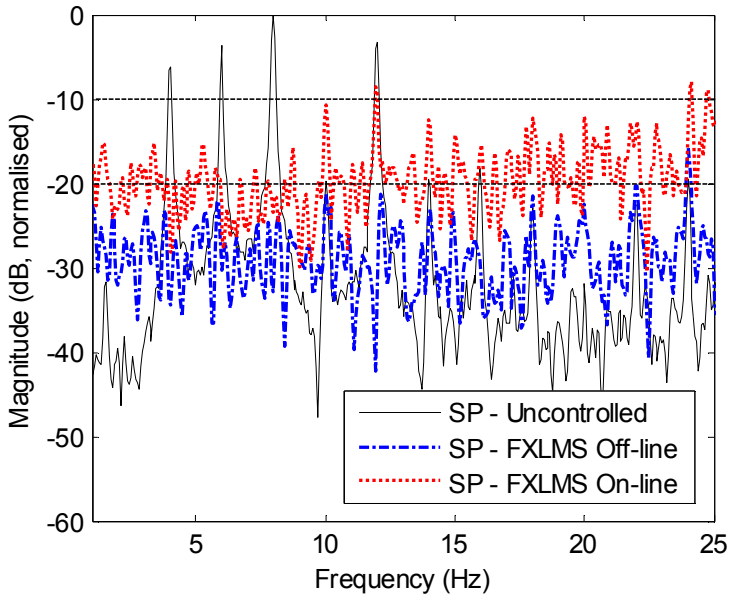

Figure 8.14: Harmonic cancellation results on the seat pan.

Figures 8.15 and 8.16 show the harmonic cancellation results on the dummy pelvis and shoulder, respectively. It can be seen that similar reduction levels are achieved for both the cases. The vibration level on the dummy pelvis and shoulder was reduced to below -10 dB at all the harmonic frequencies and the maximum cancellation occurs at 6 Hz. Again, some additional harmonics at 10 Hz, 14 Hz, 18 Hz and 24 Hz can be observed on the dummy pelvis and shoulder cancellation plots. These are a result of the dummy dynamics being excited by the active cancellation force.

The vibration reduction level achieved in this set of tests demonstrated the effectiveness of the active seat system for cancelling multiple harmonic vibrations.

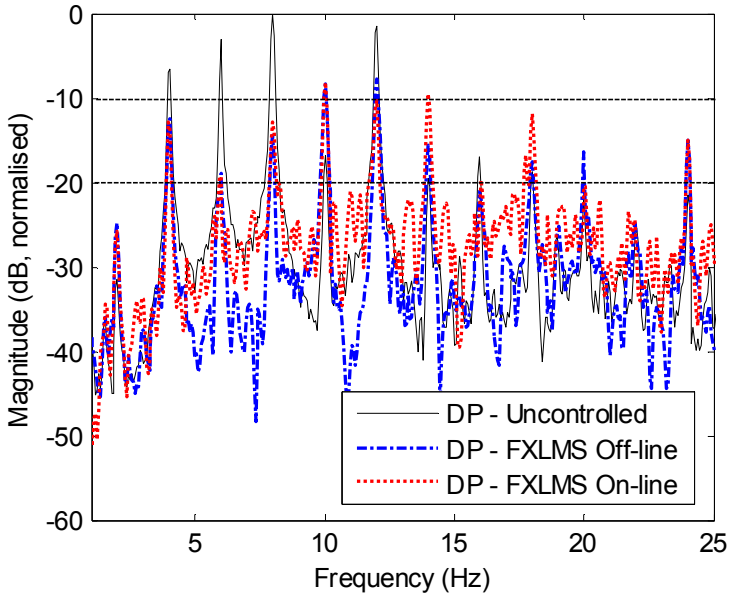

Figure 8.15: Harmonic cancellation results on the dummy pelvis.

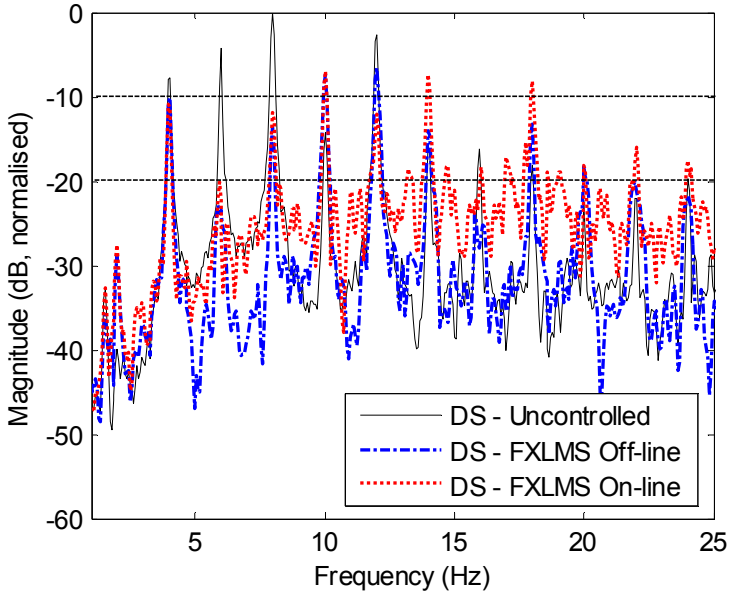

Figure 8.16: Harmonic cancellation results on the dummy shoulder.

8.4 Transient switching frequency cancellation

Transient switching frequency cancellation tests were carried out to evaluate the speed of response and robustness of the adaptive control system. The excitation vibration contains three frequencies, the fundamental frequency and the second and third harmonics, which are to be cancelled. Similar to the multiple harmonics excitation, the overall peak input acceleration for each period is approximately 0.1 g. All the sub-controllers were switched on with zero initial gains and they were all fully adapted before the frequencies were changed. In this set of tests, the active cancellation system with both the secondary path 1 and 2 were investigated. Given that the cancellation performance with off-line FBLMS secondary path identification has already been introduced for results comparison in the two previous tests, only the results with the on-line FBLMS secondary path identification are presented in the following sections.

8.2.1 Results for the secondary path 1

In this test, a filter length of 128 was used. The signal started at frequencies of 3 Hz, 6 Hz and 9 Hz, and changed to 4 Hz, 8 Hz and 12 Hz, then to 5 Hz, 10 Hz and 15 Hz over 120 seconds. Each transient period is 40 seconds, which is long enough to validate the response of the FXLMS controller with on-line secondary path identification. The on-line identification white noise variance was 0.4 and the convergence rate was 5×10^{-3}. Different convergence rates, as shown in Table 8.2, were used for different sub-controllers and they changed as the frequencies switched in order to achieve better cancellation performance. However, fixed convergence rates can be used for normal stable operation.

Table 8.2: Cancellation filter convergence rates in the switching frequency test.

Filter	Convergence rate	Filter	Convergence rate	Filter	Convergence rate
3 Hz	1.8×10^{-3}	4 Hz	1.4×10^{-3}	5 Hz	1×10^{-3}
6 Hz	8×10^{-4}	8 Hz	3.5×10^{-4}	10 Hz	1×10^{-4}
9 Hz	4×10^{-4}	12 Hz	1.2×10^{-4}	15 Hz	4×10^{-5}

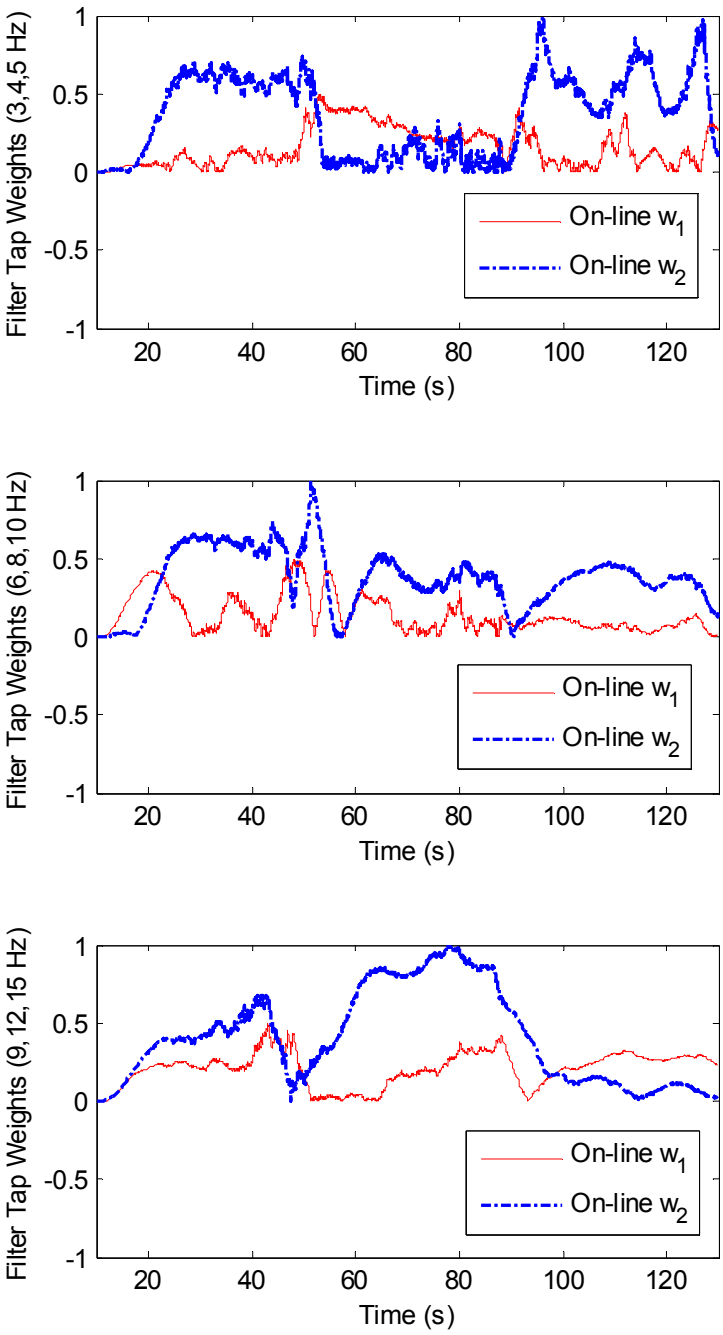

Figure 8.17: Tap weight trajectories of different sub-controllers for the switching frequency cancellation test.

Figure 8.17 shows the filter tap weight trajectories of different sub-controllers during frequency switching. It can be observed that all the weights have reasonable stable adaptions during the test period in spite of some notable oscillations.

Figure 8.18 presents a comparison between the original vibration and the active cancellation results with on-line secondary path identification on the seat pan during the transient switching frequency period. It can be seen that all the controllers are able to rapidly adapt to the changing conditions and provide significant levels of cancellation at the target frequencies. The initial adaption period is around 8 seconds, and stable cancellation for each frequency is seen after the controllers were fully adapted. Low level random noise which is introduced by the on-line FBLMS identification process is shown in the cancellation spectrogram as expected.

Figure 8.19 and 8.20 show spectrograms of the original vibration and the cancellation results on the dummy pelvis and shoulder during the frequency switching period, respectively. As it can be observed that the vibration level on the dummy pelvis and shoulder is substantially reduced by the active control system at all the target frequencies. Also, a robust and rapid adaption during the frequency transient is confirmed.

As previously stated, in the experimental tests using the secondary path 1 the control algorithm only utilized the acceleration signal on the seat pan as the feedback error signal. This means the estimated secondary path only contains the dynamics of the active seat system. As was indicated in the single frequency test, better cancellation performance on the dummy shoulder can be achieved by taking the dummy dynamics into account. In the next section, the cancellation results of the switching frequency test using the secondary path 2 (MAST to dummy shoulder) is presented for additional evaluation.

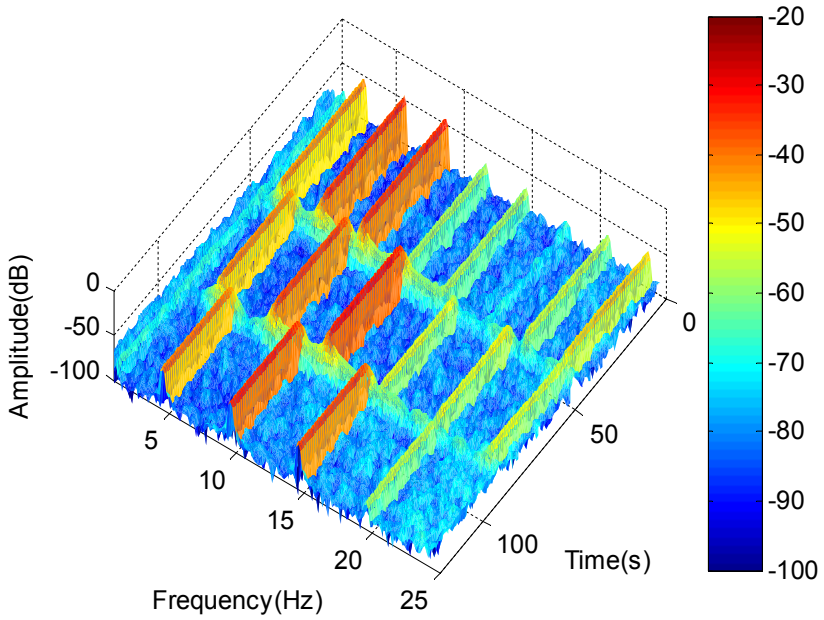

(a)

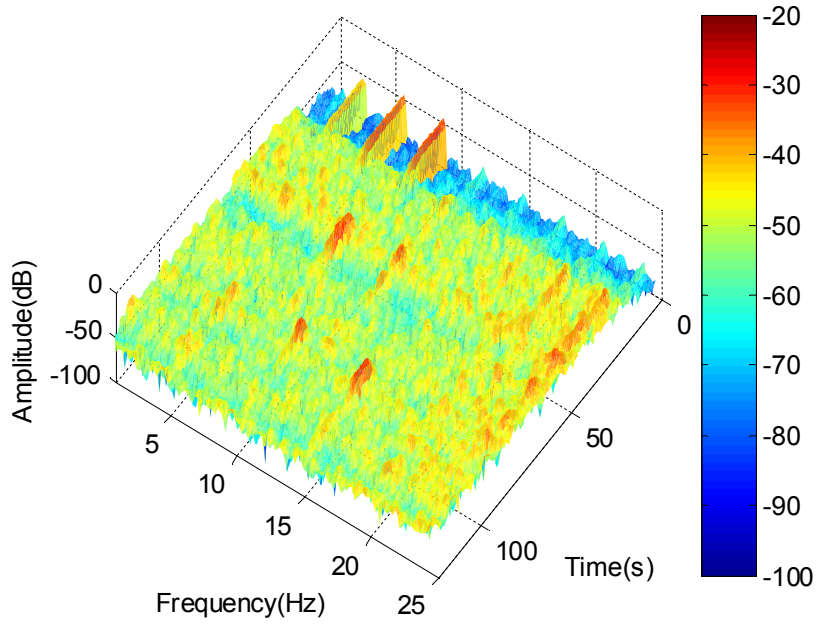

(b)

Figure 8.18: Spectrograms of the original vibration and active cancellation results on the seat pan during the transient switching frequency period. (a) Original vibration; (b) after cancellation.

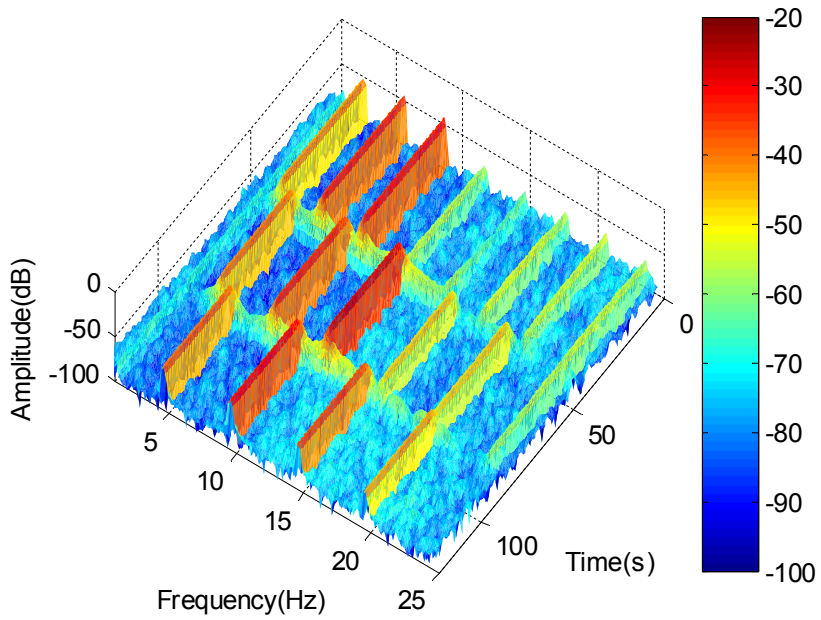

(a)

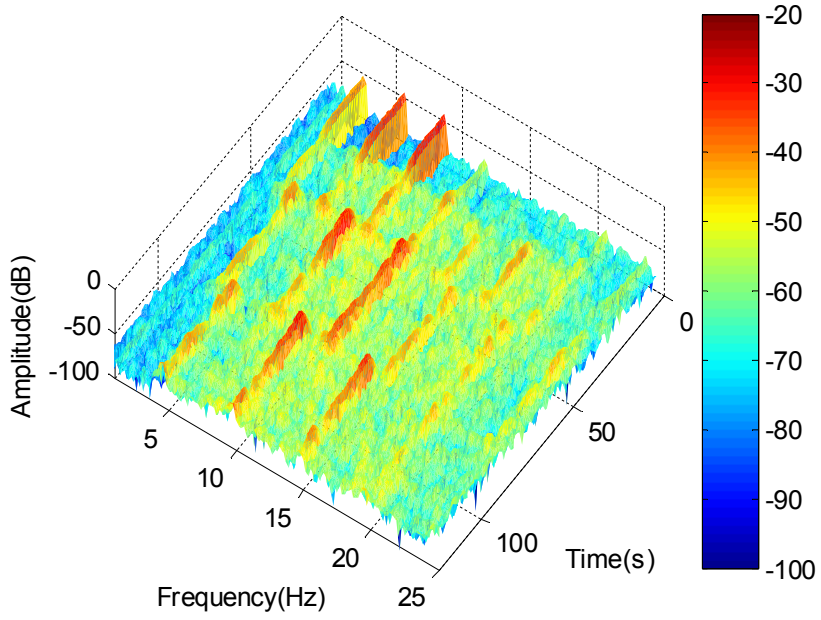

(b)

Figure 8.19: Spectrograms of the original vibration and active cancellation results on the dummy pelvis during the transient switching frequency period. (a) Original vibration; (b) after cancellation.

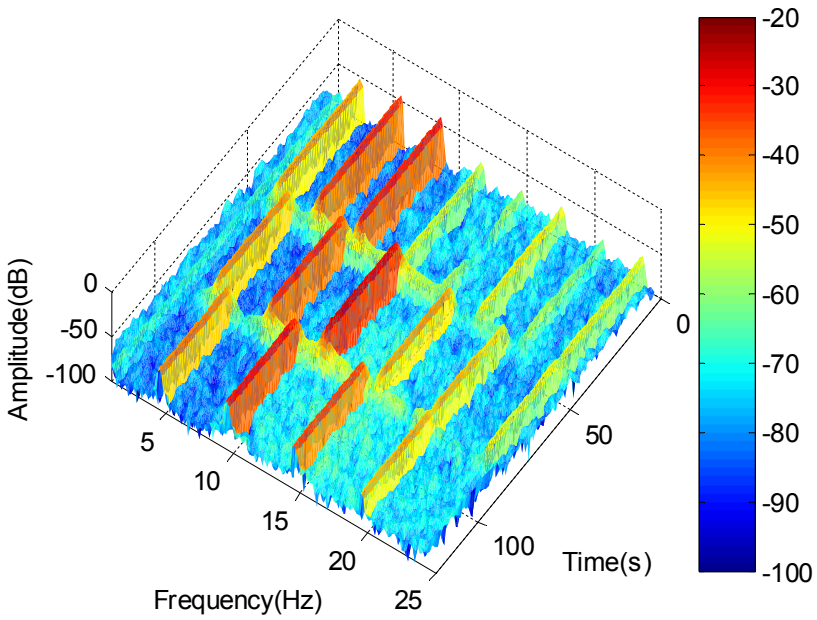

(a)

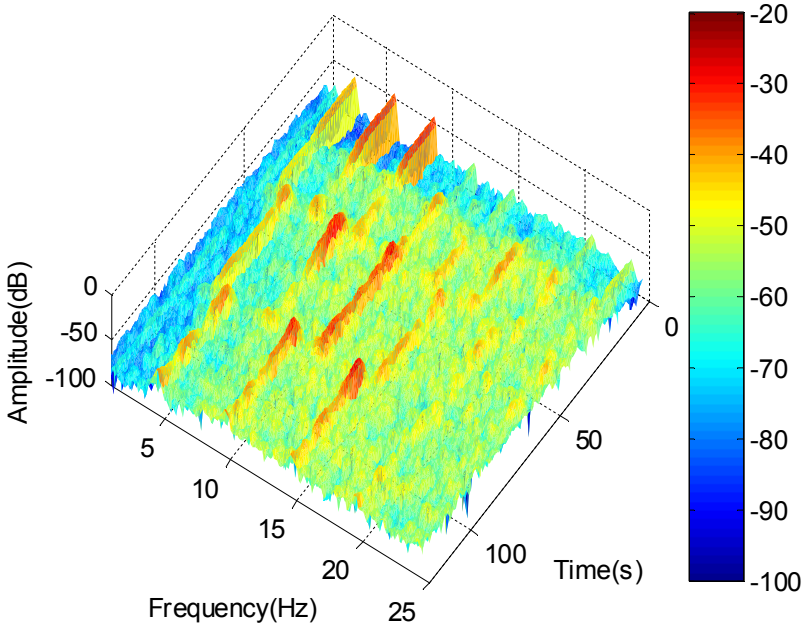

(b)

Figure 8.20: Spectrograms of the original vibration and active cancellation results on the dummy shoulder during the transient switching frequency period. (a) Original vibration; (b) after cancellation.

8.2.2 Results for the secondary path 2

In this test, a double filter length of 256 was used to ensure that the essential dynamic characteristics of the secondary path were captured. The signal started at frequencies of 4 Hz, 8 Hz and 12 Hz, and changed to 5 Hz, 10 Hz and 15 Hz, then to 6 Hz, 12 Hz and 18 Hz over 120 seconds with each transient period lasting 40 seconds.

Similar to the case using the secondary path 1, the on-line identification white noise variance was 0.4 and the convergence rate was 5×10^{-3}. Again, different convergence rates, as shown in Table 8.3, were used for different sub-controllers and frequencies in order to achieve better cancellation performance.

Table 8.3: Cancellation filter convergence rates in the switching frequency test.

Filter	Convergence rate	Filter	Convergence rate	Filter	Convergence rate
4 Hz	4×10^{-3}	5 Hz	1×10^{-3}	6 Hz	1×10^{-3}
8 Hz	3×10^{-4}	10 Hz	1×10^{-4}	12 Hz	2×10^{-4}
12 Hz	1×10^{-4}	15 Hz	1.5×10^{-5}	18 Hz	1×10^{-5}

Figure 8.21 shows the comparison between the original vibration and the active cancellation result on the seat pan during the transient switching frequency period. It is seen that a good level of vibration reduction was achieved after a short initial adaptive period. Rapid adaptation is found during the transient of the frequency switching. As shown previously, a low level random noise was inevitably introduced by the on-line identification process.

Figure 8.22 and 8.23 show spectrograms of the original vibration and the cancellation results on the dummy pelvis and shoulder during the frequency switching period, respectively. It can be observed that better vibration cancellations on the dummy pelvis and shoulder were achieved compared with the results using the secondary path 1 as shown in Figure 8.19 and 8.20. Again, the control system's robustness and rapid response are confirmed.

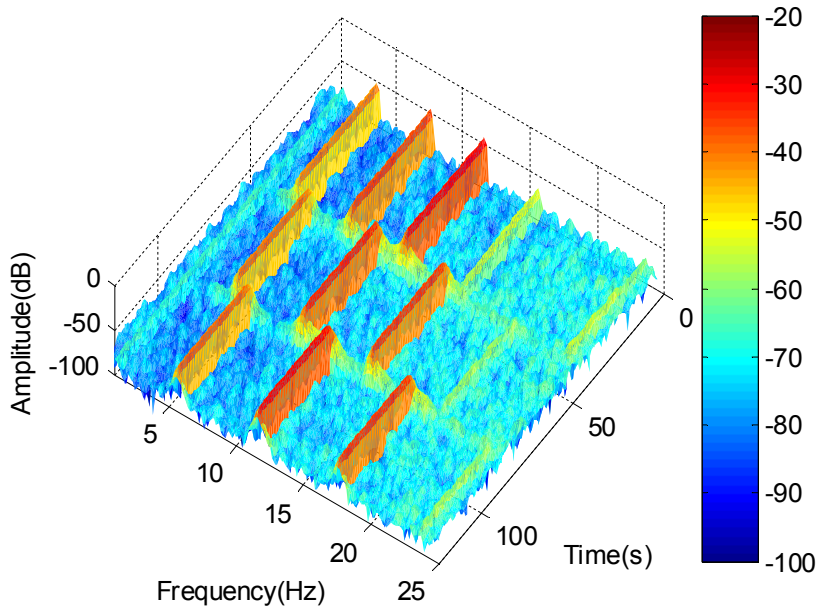

(a)

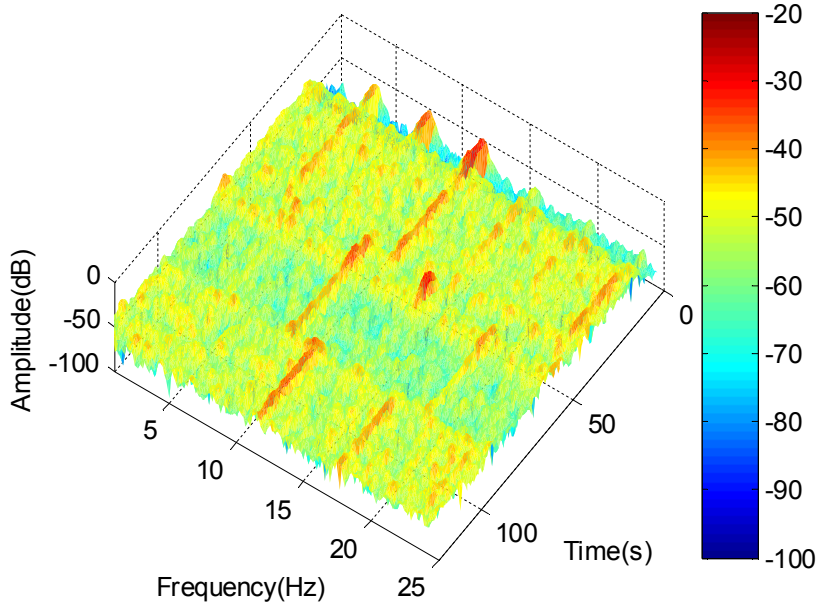

(b)

Figure 8.21: Spectrograms of the original vibration and active cancellation result on the seat pan during the transient switching frequency period. (a) Original vibration; (b) after cancellation.

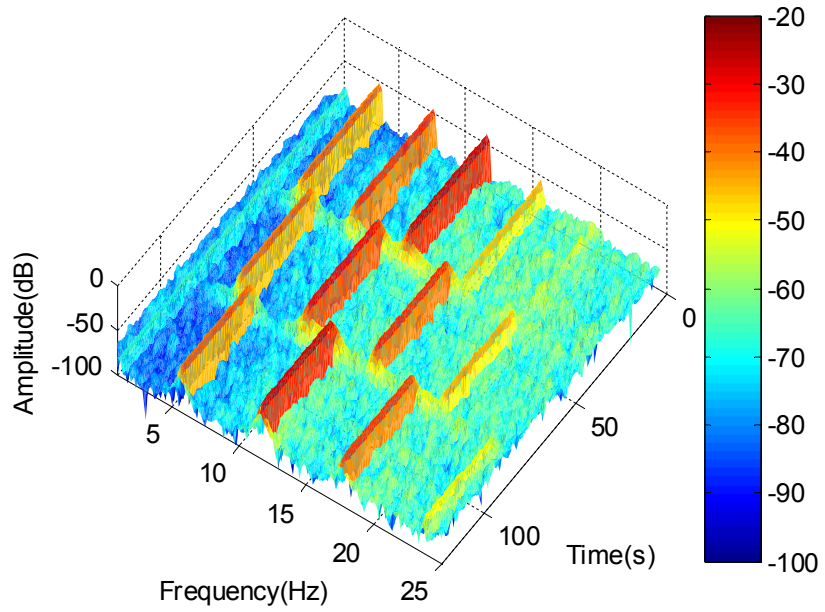

(a)

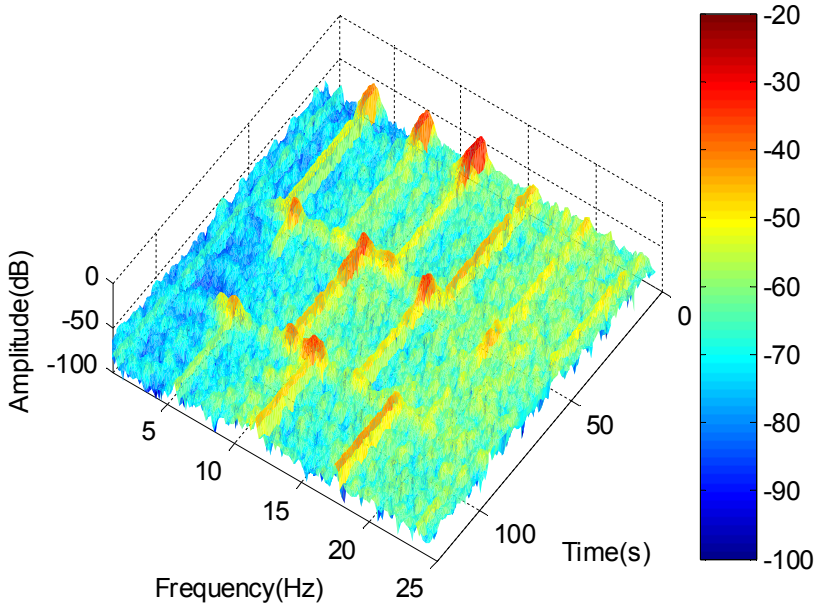

(b)

Figure 8.22: Spectrograms of the original vibration and active cancellation result on the dummy pelvis during the transient switching frequency period. (a) Original vibration; (b) after cancellation.

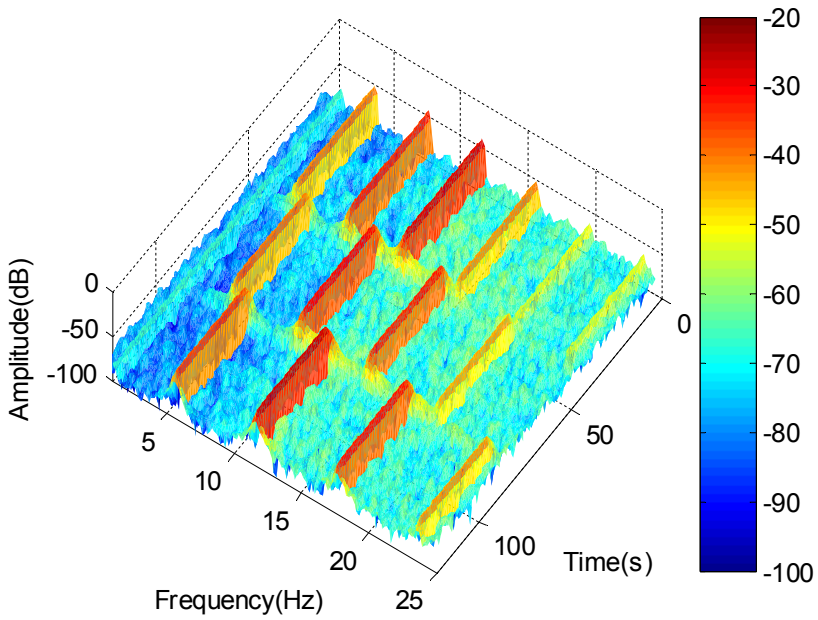

(a)

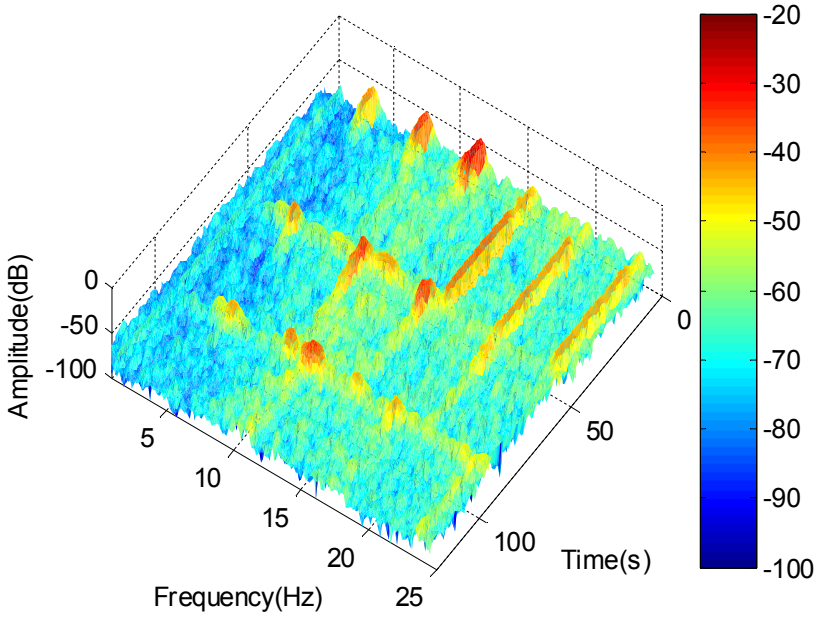

(b)

Figure 8.23: Spectrograms of the original vibration and active cancellation result on the dummy shoulder during the transient switching frequency period. (a) Original vibration; (b) after cancellation.

8.5 Performance when subject to low-frequency large amplitude disturbances

As mentioned in Chapter 6, in some practical applications such as helicopters, a single frequency (blade passing frequency) may be accompanied by unfiltered low-frequency large amplitude disturbances associated with the maneuvering. It is crucial that the control algorithm can effectively reject these disturbances during operation.

In this test, the performance of the active seat with the FXLMS adaptive control was examined by cancelling a 6 Hz single frequency vibration (0.1 g peak input acceleration approximately) combined with large amplitude disturbances at frequencies of 0.5 Hz and 1 Hz, respectively. The peak input acceleration for the 0.5 Hz disturbance was 0.04 g and for the 1 Hz disturbance was 0.09 g approximately. The duration of this test was 50 seconds and the controller was switched on at 10 seconds. Only the secondary path 1 with on-line identification was selected for this evaluation.

Figure 8.24 shows the spectrogram of the cancellation results on the seat pan for the 0.5 Hz disturbance. It can be observed that the target frequency at 6 Hz is successfully supressed with the presence of the low-frequency disturbance. The effectiveness of the controller for vibration reduction and disturbance rejection can be seen more clearly on the dummy pelvis and shoulder results shown in Figure 8.25 and 8.26, respectively.

The actuation force saturation problem found with a simple feedforward PI controller (Chapter 6) is not seen in this test. This was because the narrow-band FXLMS controller which works as a notch filter only responded to the vibration component on the target frequency and efficiently rejected the low-frequency large amplitude disturbance.

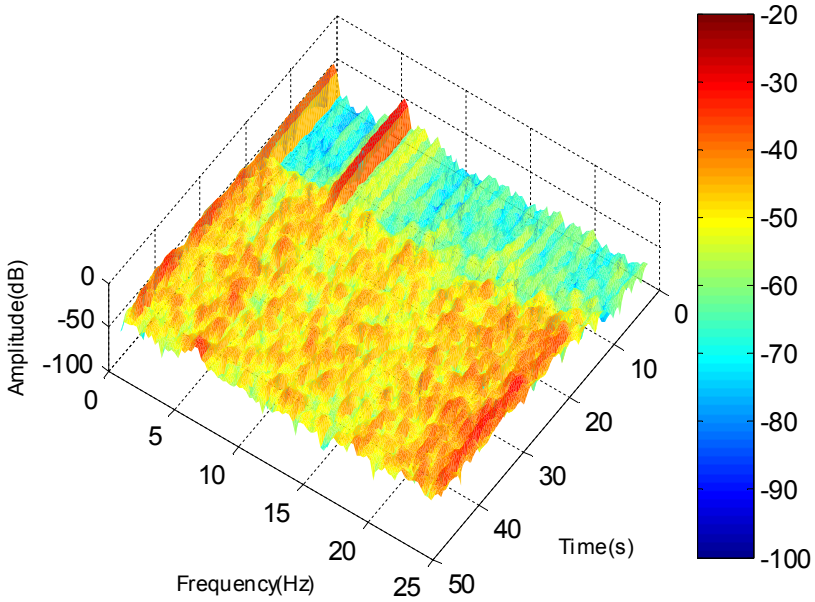

Figure 8.24: Spectrogram of the cancellation result on the seat pan for the 0.5 Hz disturbance.

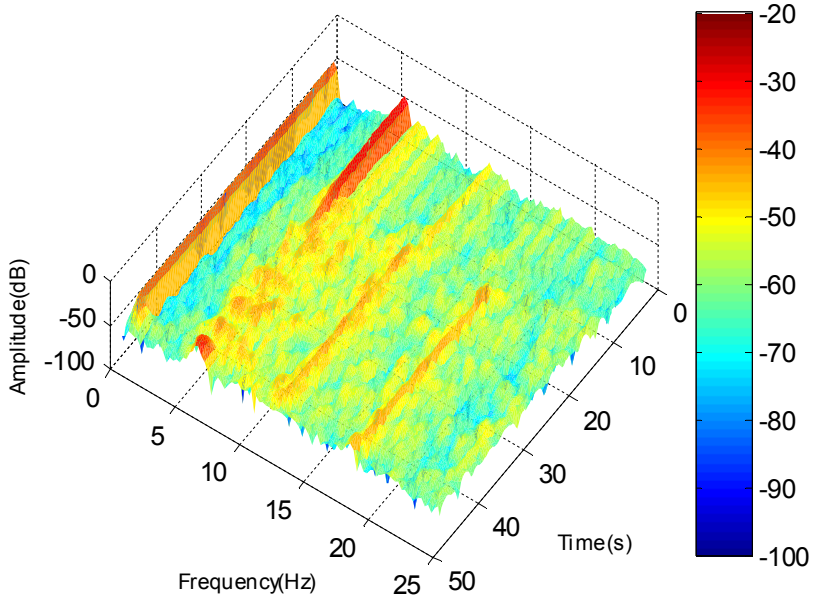

Figure 8.25: Spectrogram of the cancellation result on the dummy pelvis for the 0.5 Hz disturbance.

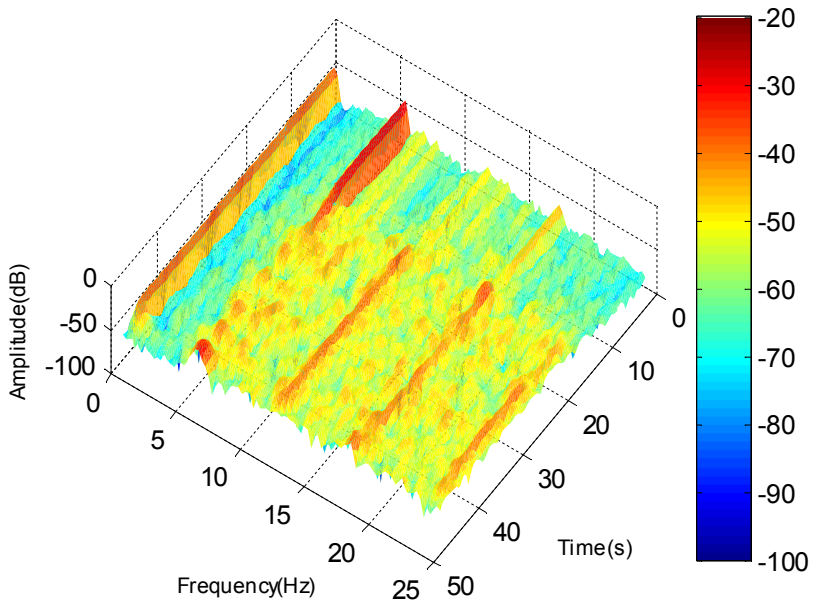

Figure 8.26: Spectrogram of the cancellation result on the dummy shoulder for the 0.5 Hz disturbance.

Figure 8.27 shows the spectrogram of the cancellation results on the seat pan for the 1 Hz disturbance. In a similar manner to the test results achieved using the 0.5 Hz disturbance, generally good vibration reduction is seen at the target frequency while the vibration at the 1 Hz disturbance remained. Again, a clearer demonstration of disturbance rejection and target frequency cancellation can be found in Figure 8.28 and 8.29.

From the above test results, it can be seen that the effects of the low-frequency large amplitude disturbance on the adaptive control system are insignificant. This indicates that stable vibration cancellation can be achieved using the active seat system in the presence of some unfiltered low-frequency disturbances.

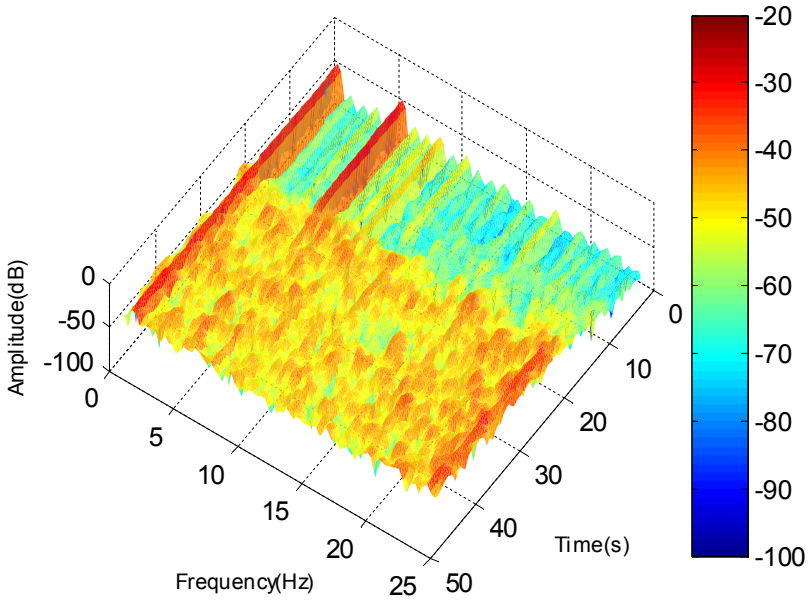

Figure 8.27: Spectrogram of the cancellation result on the seat pan for the 1 Hz disturbance.

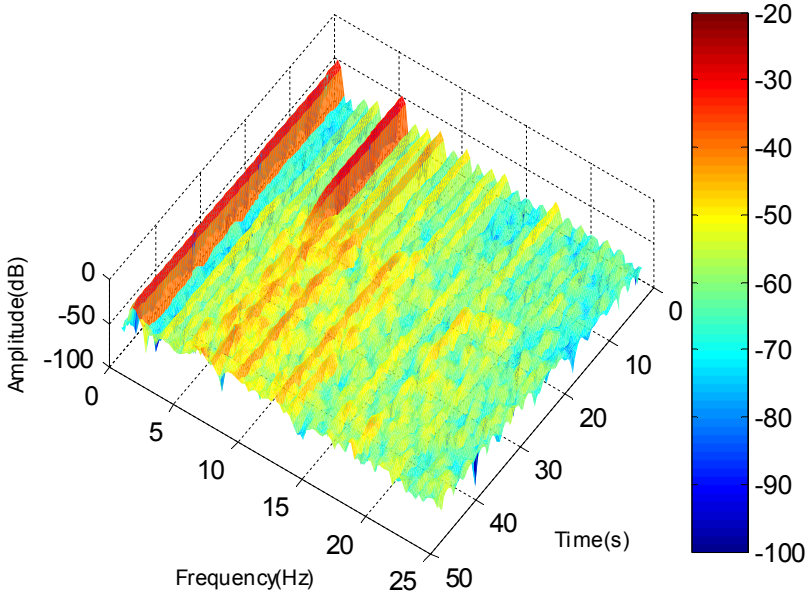

Figure 8.28: Spectrogram of the cancellation result on the dummy pelvis for the 1 Hz disturbance.

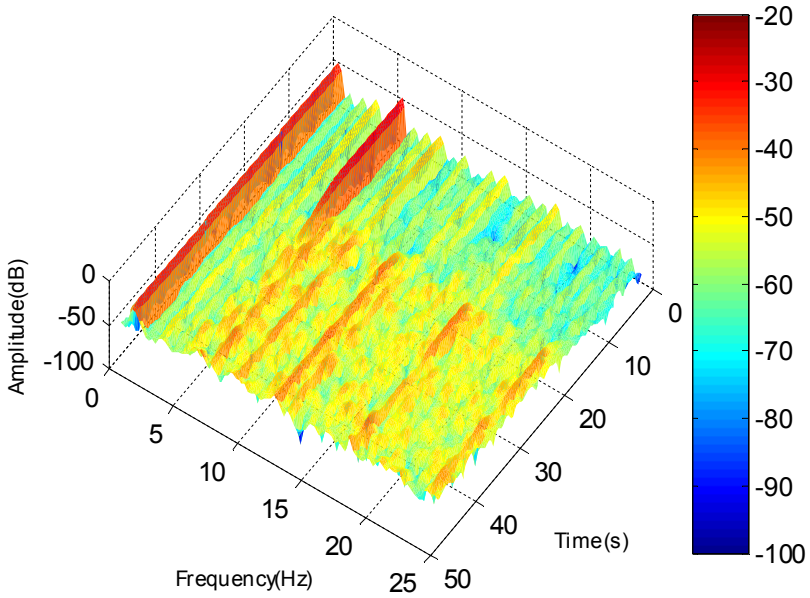

Figure 8.29: Spectrogram of the cancellation result on the dummy shoulder for the 1 Hz disturbance.

8.6 Discussions

From the comparison between the results achieved using off-line and on-line secondary path identification, it is clearly seen that the adaptive periods of the on-line cases were longer than those of the off-line cases. However, as stated previously, to assure the stability of the cancellation system, it is necessary to perform the on-line identification and cancellation process simultaneously if the secondary path dynamic is time-varying. In practical operations, for slow time-varying systems, the on-line identification process can be conducted occasionally rather than continuously in order to decrease the adaptive duration and reduce the computational burden.

The random noise which was inevitably introduced by the on-line secondary path identification process slightly degraded the vibration suppression effect on the seat pan. However, the random vibration transmitted to the dummy body was reduced to a low level as shown in the test results. In addition, in practical applications this noise can be further isolated passively by employing seat cushions. Since the experiment's sole focus was the active control system, a passive cushion was not used in these tests.

The comparison between the test results using the secondary path 1 and 2 revealed that larger vibration cancellation level on the dummy pelvis and shoulder can be achieved when the dummy dynamic is included in the estimated secondary path model. However, a longer filter length is required for the increased complexity of the second path to ensure the major dynamic characteristics are captured.

The transient switching frequency test results showed that the adaptive control system was able to rapidly adapt to the changing conditions and provide significant levels of vibration cancellation at the target frequencies. In this set of tests, different convergence rates were used for different sub-controllers and different frequencies in order to achieve a better cancellation performance. However, fixed convergence rates can be used for normal stable operations.

The results of the experimental tests including low-frequency large amplitude disturbances verified the effectiveness of the FXLMS adaptive controller for noise rejection. This feature makes the adaptive control system suitable for use in practical applications where the target frequency usually accompanied with some unfiltered low-frequency disturbances.

8.7 Conclusions

The combination of the FXLMS algorithm with the FBLMS system identification technique has been applied to the active seat. The vibration cancellation performance of the active seat system has been evaluated through extensive experimental tests using a variety of input vibration profiles. Substantial vibration reductions were achieved for the single frequency and multiple harmonic signals. A robust and rapid performance was shown by the transient switching frequency cancellation test. Additionally, the stability of the control system was further validated by cancelling vibration signals combined with low-frequency large amplitude disturbances. The experimental results presented in this chapter demonstrated the capability of the active seat using adaptive control for seated occupant's vibration reduction.

Chapter 9

Conclusions and Future Work

This chapter gives the conclusions and discussions of the work described throughout this thesis. The main achievements and contributions of the research work are summarised. Recommendations for future work are also included.

1.1 Conclusions

The work described in this thesis forms a successful simulation and experimental study of an active seat and control algorithm for occupants' whole-body vibration (WBV) reduction under low frequency excitations (1-25 Hz).

Prior to the design of an active seat system, a modelling study of seated human subjects (SHS) and an extensive experimental investigation into the vibration transmissibility of a test dummy and vehicle seat were carried out. The biodynamic responses of SHS exposed to uncoupled vertical and fore-and-aft WBV was modelled. The main limitation of existing SHS models is that they were derived to satisfy a single biodynamic response function. Such an approach may provide a reasonable fit with the function data being considered but uncertain matches with the others. The model presented in this study is based on all three types of biodynamic response functions: seat-to-head transmissibility (STHT), driving-point mechanical impedance (DPMI) and apparent mass (APM). The goodness-of-fit of the model developed in this work was evaluated graphically and statistically. A comparison with existing models was carried out and the results demonstrated that an improved fit with the aggregated experimental data was achieved. Through the model, the biodynamic behaviour of seated human subjects can be observed in a more comprehensive way. The model was also used to develop an experimental vibration test dummy which was used as a seated human body substitute in subsequent active seat

vibration cancellation tests in order to ensure an improved consistency in behaviour and avoid safety and ethical issues.

An active seat was developed based upon the observations and understanding of the SHS and seat system. The active seat was required to provide efficient vibration isolation in a low frequency excitation range of 1-25 Hz. The characteristics of the active seat dynamics were identified through experimental tests. Based on the measured system dynamics, the rig was identified as being suitable for the development of an active seat to attenuate the vibration experienced by vehicle occupants.

The vibration cancellation performance of the active seat using feedforward plus proportional-integral (PI) control was initially examined. Through these tests, the effectiveness of the actuator's control authority was verified and an understanding of the real-time implementation was gained. However, these tests also revealed the limitations of the feedforward plus PI control method when applied to this non-linear system. Firstly, the controller was not able to efficiently cancel multiple frequency components in the excitation signal. Secondly, the control performance was significantly influenced by the unfiltered low-frequency disturbance. Since the parameters of the feedforward controller were based on the identified system dynamics, *a priori* knowledge of the system was required to implement the controller. Because the active seat system is subject to non-linear and time-varying behaviour, *a priori* knowledge about the plant and disturbance is not available. Thus, a self-tuning fully adaptive algorithm is a prime requirement. The FXLMS algorithm with the FBLMS system identification technique was found suitable for this application and was selected for detailed investigation through experimental tests. Substantial vibration reductions were achieved for a variety of input vibration profiles. The robustness and stability of the control system was proven by cancelling vibration input signals which switched in frequency. Additionally, the results of the experimental tests under low-frequency large amplitude disturbances verified the effectiveness of the FXLMS adaptive controller for noise rejection. To conclude, the experimental results demonstrated an excellent capability of the active seat and control system for efficiently reducing the vibration level of seated occupants under low-frequency whole-body vibration.

1.2 Recommendations for future work

The research that has been undertaken for this thesis has indicated a number of topics which deserve further research.

- The random noise which was inevitably introduced by the on-line secondary path identification process degraded the vibration suppression effect to some extent. A seat cushion could be added to the active seat to passively isolate the low level random noise.

- The mechanical structure of the active seat could be improved and refined to reduce friction and backlash between the joints and linear guiders. The non-linearity of the active seat could be reduced and thus the system robustness could be improved.

- The active seat could be modified and combined with a crashworthy mechanism to meet shock protection requirements while providing enhanced vibration isolation for rotorcrafts occupants.

- The research work presented in this thesis only focused on the reduction of the dominate vibration in the vertical direction. The active seat system could be extended to consider the pitch vibration.

- The FXLMS algorithm was applied to the active seat for cancelling narrow-band vibrations. Further work could be aimed at extending the narrow-band adaptive algorithm to deal with broad-band vibration which may be introduced by road roughness on commercial vehicles, such as heavy duty trucks.

- Should the active seat system progress towards production then it must be fully tested under all real conditions. The adaptive algorithm described in this thesis must be implemented with on-board processors.

- No study was conducted here to establish the costs of the active system in terms of the resulting power consumption. It would be beneficial to investigate the power efficiency of the active system and establish an optimal cost functions for

minimisation rather than measured error signals. The cost functions would balance cancellation performance against power consumption.

References

[1] M.H. Pope, D.G. Wilder, and M.L. Magnusson. A review of studies on seated whole body vibration and low back pain. *Proceedings of the Institution of Mechanical Engineers, Part H: Journal of Engineering in Medicine*, 1999, 213-435.

[2] G.S. Paddan and M.J. Griffin. Evaluation of whole-body vibration in vehicle. *Journal of Sound and Vibration,* 2002, 253(1), 195–213.

[3] C. Hulshof and B. Veldhuijzen van Zanten. Whole-body vibration and low back pain- A review of epidemiologic studies. *International Archives of Occupational and Environmental Health*, 1987, 59, 205-220.

[4] A. Burdorf and G. Sorock. Positive and negative evidence on risk factors for back disorders. *Scandinavian Journal of Work, Environment and Health*, 1997, 23, 243-256.

[5] P.M. Bongers, H.C. Boshuizen, C. Hulshof, and A.C. Koemeester. Back disorders in crane operators exposed to whole-body vibration. *International Archives of Occupational and Environmental Health,* 1988, 60, 129-137.

[6] M. Bovenzi and A. Betta. Low-back disorders in agricultural tractor drivers exposed to whole-body vibration and postural stress. *Applied Ergonomics*, 1994, 25, 231-241.

[7] P.E. Boileau and S. Rakheja. Whole-body vertical biodynamic response characteristics of the seated vehicle driver measurement and model development. *International Journal of Industrial Ergonomics*, 1997, 22, 449-472.

[8] S. Rakheja, R.G. Dong, S. Patra, P.E. Boileau, P. Marcotte, and C. Warren. Biodynamics of the human body under whole-body vibration: Synthesis of the reported data. *International Journal of Industrial Ergonomics*, 2010, 40, 710-732.

[9] G.S. Paddan and M.J. Griffin. A review of the transmission of translational seat vibration to the head. *Journal of Sound and Vibration,* 1998, 215(4), 863-882.

[10] J.E. Smeathers and V. Wright. Response of the human body to impact dynamics and vibration. *Journal of engineering in medicine*, 1989, 203(H), 179-180.

[11] M.H. Pope, D.G. Wilder, and M.L Magnusson. A review of studies on seated whole body vibration and low back pain. *Proceedings of the Institution of Mechanical Engineers, Part H: Journal of Engineering in Medicine,* 1999, 213-435.

[12] M.H. Pope, H. Broman, and T. Hansson. The dynamic response of a subject seated on various cushions. *Ergonomics,* 1989, 32(10), 1155-1166.

[13] J. W. Coltman, C. Van Ingen, and N.B. Johnson, and R.E. Zimmerman. Aircraft Crash Survival Design Guide Vol. II – Aircraft Crash Design Impact Conditions and Human Tolerance. *Aviation Applied Technology Directorate, USAAVSCOM Technical Report,* 89-D-22B, 1989, 29-87.

[14] S.P. Desjardins. The Evolution of Energy Absorption Systems for Crashworthy Helicopter Seats. *Journal of the American Helicopter Society*, 2006, 51(2), 150-163.

[15] George E.P. Box and R.D. Norman. *Empirical Model-Building and Response Surfaces.* Wiley, 1987.

[16] S. Moss and Y. Huang. Development of an advanced finite element model database of the Hybrid III crash test dummy family. *SAE Paper* 971042, 1997.

[17] P.J. Arnoux, H.S. Kang, and K. Kayvantash. The Radioss Human model for Safety. *Arch. Physiol. Biochem.,* 2001, 109, 109–113.

[18] M. Iwamoto, Y. Kisanuki, I. Watanabe, K. Furusu, K. Miki, and J. Hasegawa. Development of a finite element model of the total human model for safety (THUMS) and application to injury reconstruction. *Proceedings of IRCOBI conference, Munich, Germany*, 2002, 31–42.

[19] M.M. Panjabi. Three-dimensional mathematical model of the human spine structure. *J. Biomechanics*, 1973, 6, 671-680.

[20] J.L. Hess and C.F. Lombard. Theoretical investigations of dynamic response of man to high vertical acceleration. *J. Aviat. Med.,* 1958, 29, 66-75.

[21] Y.K. Liu and J.D. Murray. A theoretical study of the effect of impulse on the human torso. *ASME Biomechanics Symposium*, 1966, 167-186.

[22] C.T. Terry and V.L. Roberts. A viscoelastic model of the human spine subjected to +g z accelerations. *J. Biomechanics*, 1968, 1, 161-168.

[23] F. Latham. A study in body ballistics: seat ejection. *Process of Royal Society, Biological Sciences*, 1957, 147(926), 121-139.

[24] R. Toth. Multiple degree-of-freedom nonlinear spinal model. *Presented 19th Annual Conference on Engineering in Medicine and Biology*, San Francisco, California, 1967.

[25] D. Orne and Y.K. Liu. A mathematical model of spinal impact. *J. Biomechanics,* 1971, 4, 49-71.

[26] M.M. Panjabi. Three-dimensional mathematical model of the human spine structure. *J. Biomechanics*, 1973, 6, 671-680.

[27] T. Yoshimura, K. Nakai, and G. Tamaoki. Multi-body dynamics modelling of seated human body under exposure to Whole-Body Vibration. *Industrial Health*, 2005, 43, 441-447.

[28] C.W. Suggs, C.F. Abrams, and L.F. Stikeleather. Application of a damped spring-mass human vibration simulator in vibration testing of vehicle seats. *Ergonomics*, 1969, 12, 79-90.

[29] R.R. Payne and E.G.U. Band. A four-degree-of-freedom lumped parameter model of the seated human body. *Aerospace Medical Research Laboratories Report AMRL-TR-70-35. Wright-Patterson Air Force Base*, OH, 1971.

[30] L. Wei and M.J. Griffin. The prediction of seat transmissibility from measures of seat impedance. *Journal of Sound and Vibration*, 1998, 212, 855-874.

[31] J. Rosen and M. Arcan. Modelling the human body-Seat system in a vibration environment. *Journal of Biomechanical Engineering*, 2003, 125, 223-231.

[32] D.C. Karnopp, M.J. Crosby, and R.A. Harwood. Vibration Control Using Semi-Active Force Generators. *ASME Journal of Engineering for Industry,* 1974, 619-626.

[33] X. Wu and M.J. Griffin. A semi-active control policy to reduce the occurrence and severity of end-stop impacts in a suspension seat with an electrorheological fluid damper. *Journal of Sound and Vibration,* 1997, 203, 781–793.

[34] S.B. Choi, M.H. Nam, and B.K. Lee. Vibration control of a MR seat damper for commercial vehicles. *Journal of Intelligent Material Systems and Structures,* 2000, 11, 936-944.

[35] S.J. McManus, K.A. St. Clair, P.E. Boileau, and J. Boutin. Evaluation of vibration and shock attenuation performance of a suspension seat with a semi-active magnetorheological fluid damper. *Journal of Sound and Vibration*, 2002, 253(1), 313–327.

[36] G.J. Hiemenz, W. Hu, and N.M. Wereley. Semi-active magnetorheological helicopter crew seat suspension for vibration isolation. *Journal of Aircraft,* 2008, 45, 945-953.

[37] Y. Chen, V. Wickramasinghe, and D.G. Zimcik. Development of adaptive helicopter seat for aircrew vibration reduction. *Journal of Intelligent Material Systems and Structures*, 2011, 22-489.

[38] M. Kawana and T. Shimogo. Active Suspension of Truck Seat. *Shock and Vibration* 1998, 5(1), 35-41.

[39] G.J. Stein. A driver's seat with active suspension of electro-pneumatic type, *Journal of Vibration and Acoustics*, 1997, 119(2), 230-235.

[40] I. Maciejewski, L. Meyer, and T. Krzyzynski. The vibration damping effectiveness of an active seat suspension system and its robustness to varying mass loading. *Journal of Sound and Vibration,* 2010, 329, 3898–3914.

[41] M. Appleyard and P.E. Wellstead. Active Suspensions: Some background, *IEE Proc. Control theory Appl.,* 1995, Vol. 142, 2, 123-128.

[42] Anonymous, *Bose Ride System* [online], 2015. Available from: http://www.boseride.com/seat-suspension-system [Accessed 16/02/2015].

[43] E.J. Krasnicki. The experimental performance of an "on-off" active damper. *Proceedings of the 51st Shock and Vibration Symposium, San Diego, USA*, 1980.

[44] S. Rakheja and S. Sankar. Vibration and shock isolation performance of a semi-active "on-off" damper. *Journal of Vibration, Acoustics, Stress, and Reliability in Design*, 1985, 107, 398-403.

[45] J. Alanoly and S. Sankar. A new concept in semi-active vibration isolation, American Society of Mechanical Engineers. *Journal of Mechanisms, Transmissions, and Automation in Design,* 1987, 109, 242–247.

[46] A. Alleyne and J.K. Hedrick. Nonlinear adaptive control of active suspensions. *IEEE Trans. Control Syst. Technol.*, 1995, 3, 9401.

[47] S.B. Choi, J.H. Choi, Y.S. Lee, and M.S. Han. Vibration control of an ER seat suspension for a commercial vehicle. *ASME Dynamic Systems and Control Division*, 2003, Vol. 125, 60-68.

[48] M. Novak and M. Valasek. A new concept of semi-active control of truck's suspension. *AVEC 96, Aachen, Germany,* 1996.

[49] Y. Liu, T.P. Waters, and M.J. Brennan. A comparison of semi-active damping control strategies for vibration isolators of harmonic disturbances. *Journal of Sound and Vibration*, 2005, 280, (1-2), 21-39.

[50] S.M. Savaresi, E. Silani, and S. Bittanti. Acceleration-Driven-Damper (ADD): An Optimal control algorithm for comfort-oriented semi-active suspensions. *Transactions of the ASME,* 2005, Vol.127, 218-229.

[51] B. Widrow, M.E. Hoff. Adaptive switching circuits. *Proceedings of WESCON Convention Record 4, Los Angeles, USA,* 1960, 96-140.

[52] E.H. Anderson and J.P. How. Adaptive feedforward control for actively isolated spacecraft platforms. *AIAA Structures, Structural Dynamics, and Materials Conference and Exhibit,* 1997, 7-10.

[53] J.E. Oh, S.H. Park, and J.S. Hong. Active vibration control of flexible cantilever beam using piezoactuator and Filtered-X LMS algorithm. *KSME International Journal,* 1998, 12, 665-671.

[54] J.J. Carnahan and C.M. Richards. A modification to filtered-X LMS control for airfoil vibration and flutter suppression. *Journal of Vibration and Control,* 2008, 14, 831-848.

[55] A.J. Hillis. Adaptive control of active engine mounts. *Phd thesis, University of Bristol*, 2005.

[56] K.J. Astrom and B. Wittenmark. On self-tuning regulators. *Automatica,* 1973, 9, 185-199.

[57] K.J. Astrom, U. Borisson, L. Ljung, and B. Wittenmark. Theory and applications of self-tuning regulators. *Automatica*, 1977, 13(5), 457-476.

[58] J.T. Pearson and R.M. Goodall. Adaptive schemes for the active control of helicopter structural response. *IEEE Transactions on Control Systems Technology,* 1994, Vol.2, 2, 61-72.

[59] M. Sunwoo, K.C. Cheok, and N.J. Huang. Model reference adaptive control for vehicle active suspension systems. *IEEE Transactions on Industrial Electronics,* 1991, Vol. 38, 217-222.

[60] F.B. Nejad and A.K. Mohammadi. Active vibration control of vehicles with elastic body using model reference adaptive control. *Journal of vibration and control*, 1998, Vol. 4, 463-479.

[61] J. Fei. Adaptive sliding mode vibration control schemes for flexible structure system. *Proceedings of the46th IEEE Conference on Decision and Control, LA, USA,* 2007, 1332-1337.

[62] L. Zuo, J.E. Slotine, and S.A. Nayfeh. Experimental study of a novel adaptive controller for active vibration isolation. *Proceedings of the 2004 AmericanControl Conference*, 2004, Vol. 1-6, 3862-3868.

[63] C.S. Chang and T.S. Liu. LQG controller for active vibration absorber in optical disk drive. *IEEE Transactions on Magnetics,* 2007, Vol. 43, 2, 799-801.

[64] W.T. Baumann. An adaptive feedback approach to structural vibration suppression. *Journal of Sound and Vibration*, 1997, 205(1), 121-133.

[65] H. Li, S.J. Hu, C. Jakubiak. H_2 active vibration control for offshore platform subjected to wave loading. *Journal of Sound and Vibration,* 2003, Vol. 263, 4, 709-724.

[66] A.K. Rao, K. Natesan, M.S. Bhat, and R. Ganguli. Experimental demonstration of $H\infty$ control based active vibration suppression in composite fin-tip of aircraft using optimally placed piezoelectric patch actuators. *Journal of Intelligent Material Systems and Structures,* 2007, Vol.19, 6, 651-669.

[67] C.-C. Liang, C.-F. Chiang. A study on biodynamic models of seated human subjects exposed to vertical vibration. *International Journal of Industrial Ergonomics*, 2006, 36, 869-890.

[68] B. Hinz, G. Menzel, R. Blüthner and H. Seidel. Seat-to-head transfer function of seated men-determination with single and three axis excitations at different magnitudes. *Industrial Health*, 2010*,* 48, 565-583.

[69] T.E. Fairley and M.J. Griffin. A test method for the prediction of seat transmissibility. *Society of Automotive Engineers International Congress and Exhibition Paper*, 860047, 1986.

[70] B. Hinz and H. Seidel. The nonlinearity of the human body's dynamic response during sinusoidal whole body vibration. *Industrial Health*, 1987*,* 25, 169-181.

[71] P. Holmlund and R. Lundström. Mechanical impedance of the human body in the horizontal direction. *Journal of Sound and Vibration*, 1998, 215(4), 801-812.

[72] N.J. Mansfield and M.J. Griffin. Effects of posture and vibration magnitude on apparent mass and pelvis rotation during exposure to whole-body vertical vibration. *Journal of Sound and Vibration*, 2002, 253, 93-107.

[73] M.G. Toward and M.J. Griffin. Apparent mass of the human body in the vertical direction: effect of a footrest and a steering wheel. *Journal of Sound and Vibration*, 2010, 329, 1586-1596.

[74] T.E. Fairley and M.J. Griffin. The apparent mass of the seated human body: vertical vibration. *Journal of Biomechanical Engineering*, 1987, 109, 148-153.

[75] Y. Qiu and M.J. Griffin. Biodynamic responses of the seated human body to single-axis and dual-axis vibration. *Industrial Health*, 2009, 48, 615-627.

[76] Y. Wan and J.M. Schimmels. A simple model that captures the essential dynamics of a seated human exposed to whole body vibration. *Advances in Bioengineering, ASME, BED*, 1995, 31, 333-334.

[77] G.J. Stein, P. Múčka, R. Chmúrny, B. Hinzb, and R. Blüthner. Measurement and modelling of x-direction apparent mass of the seated human body–cushioned seat system. *Journal of Biomechanics*, 2007, 40, 1493-1503.

[78] Y. Qiu and M.J. Griffin. Modelling the fore-and-aft apparent mass of the human body and the transmissibility of seat backrests. *Vehicle System Dynamics: International Journal of Vehicle Mechanics and Mobility*, 2011, 49(5), 703-722.

[79] S.M. Kuo and D.R. Morgan. *Active noise control systems: algorithms and DSP implementations*. John Wiley & Sons, New York, 1996.

[80] B. Widrow and S.D. Stearns. *Adaptive signal processing*. Prentice-Hall Inc., 1985.

[81] S.J. Elliott, I.M. Stothers, and P.A. Nelson. A multiple error LMS algorithm and its application to the active control of sound and vibration. *IEEE transactions on acoustics, speech, and signal processing, Vol. ASSP-35, 10*, 1987, 1423-1434.

[82] J. Tapia and S. M. Kuo. New adaptive on-line modelling technique for active noise control systems. *Proc. IEEE Int. Conf. systems Engineering*, 1990, 280-283.

[83] L.J. Eriksson. Active acoustic attenuation system with overall modelling. U.S. Patent 4987598, Jan. 22, 1991.

[84] C. Bao, P. Sas, and H. Van Brussel. Comparison of two on-line identification algorithms for active noise control. *Proc. Recent Advances in Active Control of Sound Vibration*, 1993, 38-51.

[85] S.J. Eilliott. *Signal processing for active control.* New York: Academic Press, 2001.

[86] M. Zhang, H. Lan, and W. Ser. On comparison of online secondary path modelling methods with auxiliary noise. *IEEE Transactions on Speech and Audio Processing, Vol. 13, No. 4,* July 2005, 618-628.

[87] L.J. Eriksson and M.C. Allie. Use of random noise for on-line transducer modelling in an adaptive active attenuation system. *Journal of Acoustical Society of America, Vol. 85,* 1989, 797–802.

[88] C. Bao, P. Sas, and H. Van Brussel. Adaptive active control of noise in 3-D reverberant enclosures. *Journal of Sound Vibration, Vol. 161,* 1993, 501–514.

[89] S.M. Kuo and D. Vijayan. A secondary path estimate techniques for active noise control systems. *IEEE Trans. Speech Audio Processing, Vol. 5, 4*, Jul. 1997, 374–377.

[90] M. Zhang, H. Lan, and W. Ser. Cross-updated active noise control system with on-line secondary path modelling. *IEEE Trans. Speech Audio Process., Vol. 9, 5*, Jul. 2001, 598–602.

[91] S. Haykin. *Adaptive Filter Theory*. New Jersey: Prentice-Hall, 3 edition, 1996.

[92] F.B. Behrouz. *Adaptive filters: theory and applications.* John Wiley & Sons, New York, 2013.